Springer ThesesRecognizing Outstanding Ph.D. Research

Cheng-Hua Liu

Electrical and Optoelectronic Properties of the Nanodevices Composed of Two-Dimensional Materials

Graphene and Molybdenum (IV)
Disulfide



Springer Theses

Recognizing Outstanding Ph.D. Research

Aims and Scope

The series "Springer Theses" brings together a selection of the very best Ph.D. theses from around the world and across the physical sciences. Nominated and endorsed by two recognized specialists, each published volume has been selected for its scientific excellence and the high impact of its contents for the pertinent field of research. For greater accessibility to non-specialists, the published versions include an extended introduction, as well as a foreword by the student's supervisor explaining the special relevance of the work for the field. As a whole, the series will provide a valuable resource both for newcomers to the research fields described, and for other scientists seeking detailed background information on special questions. Finally, it provides an accredited documentation of the valuable contributions made by today's younger generation of scientists.

Theses are accepted into the series by invited nomination only and must fulfill all of the following criteria

- They must be written in good English.
- The topic should fall within the confines of Chemistry, Physics, Earth Sciences, Engineering and related interdisciplinary fields such as Materials, Nanoscience, Chemical Engineering, Complex Systems and Biophysics.
- The work reported in the thesis must represent a significant scientific advance.
- If the thesis includes previously published material, permission to reproduce this must be gained from the respective copyright holder.
- They must have been examined and passed during the 12 months prior to nomination.
- Each thesis should include a foreword by the supervisor outlining the significance of its content.
- The theses should have a clearly defined structure including an introduction accessible to scientists not expert in that particular field.

More information about this series at http://www.springer.com/series/8790

Cheng-Hua Liu

Electrical and Optoelectronic Properties of the Nanodevices Composed of Two-Dimensional Materials

Graphene and Molybdenum (IV) Disulfide

Doctoral Thesis accepted by the National Taiwan University, Taipei, Taiwan



Author Dr. Cheng-Hua Liu National Taiwan University Taipei, Taiwan Supervisor
Dr. Wei-Hua Wang
Institute of Atomic and Molecular Sciences,
Academia Sinica
Taipei, Taiwan

ISSN 2190-5053 ISSN 2190-5061 (electronic) Springer Theses ISBN 978-981-13-1354-7 ISBN 978-981-13-1355-4 (eBook) https://doi.org/10.1007/978-981-13-1355-4

Library of Congress Control Number: 2018946677

© Springer Nature Singapore Pte Ltd. 2018

This work is subject to copyright. All rights are reserved by the Publisher, whether the whole or part of the material is concerned, specifically the rights of translation, reprinting, reuse of illustrations, recitation, broadcasting, reproduction on microfilms or in any other physical way, and transmission or information storage and retrieval, electronic adaptation, computer software, or by similar or dissimilar methodology now known or hereafter developed.

The use of general descriptive names, registered names, trademarks, service marks, etc. in this publication does not imply, even in the absence of a specific statement, that such names are exempt from the relevant protective laws and regulations and therefore free for general use.

The publisher, the authors and the editors are safe to assume that the advice and information in this book are believed to be true and accurate at the date of publication. Neither the publisher nor the authors or the editors give a warranty, express or implied, with respect to the material contained herein or for any errors or omissions that may have been made. The publisher remains neutral with regard to jurisdictional claims in published maps and institutional affiliations.

Printed on acid-free paper

This Springer imprint is published by the registered company Springer Nature Singapore Pte Ltd. The registered company address is: 152 Beach Road, #21-01/04 Gateway East, Singapore 189721, Singapore

Supervisor's Foreword

This Ph.D. thesis refers to the research of transport and optoelectronic properties of the nanoscale devices composed by two-dimensional materials, graphene and molybdenum disulfide (MoS₂). The devices are fabricated by novel lithography-free processes to achieve the high-quality graphene junction, the MoS₂ transistors, and the suspended MoS₂ transistors. Therefore, the remarkable quantum physics are distinctively demonstrated in the temperature range of 2 K < T < 300 K and the magnetic fields up to 9T. The research works were conducted in Institute of Atomic and Molecular Sciences, Academia Sinica, Taiwan and co-supervised by Prof. Chi-Te Liang of Department of Physics, National Taiwan University.

The description of the projects is given as follows:

- The high-quality graphene p-n and p-n-p junction devices are achieved by controlling the metal diffusion locally. The metal deposited on graphene surface can introduce substantial carrier scattering, limiting the mobility of intrinsic graphene. On the other hand, the weakly functionalization with small carrier scattering can achieve the p-type doping on graphene, enabling us to fabricate the graphene p-n-p junctions. Specifically, the p-type doping regions are contributed by with metal diffusion while he n-type doping is intrinsic. By engineering the lateral diffusion of metallic contacts, the graphene p-n and p-n-p junction device can be realized in one-step with resist-free fabrication. The high-quality of graphene p-n and p-n-p junctions is further substantiated by a pronounced fractional number of quantum Hall (QH) plateau.
- Distinctive magnetotransport properties of high-quality graphene p-n and p-n-p junction device described above have been further investigated. For both devices, the temperature dependence of resistance follows a power law and the analysis of the exponent indicates the dominant role of electron-hole puddles in the transport behavior. We have also utilized asymmetric method to achieve lateral diffusion in one of the two-terminal electrodes, resulting in graphene p-n junction, as evidence of pronounced QH effect. In addition, the interesting QH effect with a fractional-valued plateau as well as the Shubnikov-de Haas oscillations are demonstrated in our high-quality graphene p-n-p junction

- device. We observed a well-defined QH plateau-plateau transition of zeroth Landau level, yielding a scaling exponent of $\kappa = 0.21 \pm 0.01$. Furthermore, the graphene p-n-p junctions exhibit weak localization behavior, and the coherence length was found to be correlated to carrier scattering in the graphene devices.
- We demonstrate a giant persistent photoconductivity (PPC) effect in monolayer MoS₂ in which the photocurrent robustly persists after illumination has ceased. The PPC effect in monolayer MoS₂ FET fabricated on organic-molecule-functionalized substrates sustains up to room temperature and can be highly suppressed by applying a source—drain or back gate voltage to the transistors. The persistency and controllability of the PPC effect enable us to achieve a bistable conductance at room temperature by utilizing optical and electrical pulses, paving the way to the applications in memory devices. The observed giant PPC effect in MoS₂ can be attributed to a large electron-capture barrier of trap states, which is estimated to be as high as 390 meV.

The results demonstrated in this thesis provide insight in monolayer MoS₂ and graphene junction devices, which is significant for developing the applicable two-dimensional materials based devices in the future.

Taipei, Taiwan May 2018 Dr. Wei-Hua Wang

Abstract

The main objective of this thesis is to investigate the electrical and optoelectrical properties of two-dimensional (2D) materials. To probe the fundamental quantum physics, it is crucial to find the appropriate 2D materials and fabricate the high-quality devices which are properly designed. Graphene, one of the important 2D materials, has been demonstrated to have unique characteristics for application, such as high carrier mobility, high optical transparency, and high mechanical flexibility. In the first part of thesis, we study the magnetotransport of the graphene junction (p-n-p or p-n junction) devices which is made by the novel one-step resist-free fabrication method. The graphene p-n-p junctions were fabricated by controlling the diffusion length while depositing metal contacts. In most cases, materials deposited on graphene surface introduce substantial carrier scattering, which suppresses the intrinsic high mobility of pristine graphene, while in our cases, the metallic diffusion during the deposition process only introduces the weakly disturbed regions that leads to high performance of magnetotransport in graphene p-n-p junctions. These graphene p-n-p junction devices exhibit high performance of quantum Hall plateau at $2/3 e^2/h$ which is due to the mixing of chiral edge states in the p-n interface. At low field, coherence length analyzed by weak localization reveals a similar behavior as conductance as a function of back gate voltage. In addition, we can also demonstrate the p-n junction device in which high quality of mixing state is contributing to $1 e^2/h$ plateau in the quantum Hall regime. The two types of junction devices fabricated by resist-free method also apply a well condition for magnetotransport research.

In the second part, we further investigate the distinctive magnetotransport properties of a graphene p-n-p junction, which exhibits pronounced quantum Hall effect, a well-defined transition point of the zeroth Landau level (LL), and scaling behavior. The scaling exponent obtained from the evolution of the zeroth LL width as a function of temperature exhibits a relatively low value of $\kappa=0.21\pm0.01$. Moreover, we calculate the energy level for the LLs as a function of the LL index

viii Abstract

based on the distribution of plateau-plateau transition points, further validating the assignment of the LL index of the QH plateau-plateau transition. I also make one chapter to exhibit the quantum conductance in graphene nanoribbon which is fabricated by mechanical exfoliated method.

In the last part of thesis, we demonstrate persistent photoconductivity (PPC) in the monolayer MoS_2 devices. Here, we present a systematic study of the PPC effect and conclude that the effect can be attributed to random localized potential fluctuations in the devices. Notably, the potential fluctuations originate from extrinsic sources based on the substrate effect. Moreover, we point out a correlation between the PPC effect in MoS_2 and the percolation transport behavior of MoS_2 . We demonstrate a unique and efficient means of controlling the PPC effect in monolayer MoS_2 , which may offer novel functionalities for MoS_2 -based optoelectronic applications in the future.

Acknowledgements

Glory to God in the highest heaven, and on earth peace to those on whom his favor rests.

Luke 2:14

It is my honor to have two great supervisors, Chi-Te Liang from NTU and Wei-Hua Wang from IAMS during my time as a Ph.D. student. They provided me not only the experimental skill but also the presentation ability. Professor Liang asked me to point out what the new physics is in my experiment, and Prof. Wang asked me to do all processes from making devise in the beginning to final data analysis. I must thank them for teaching me so much.

This thesis is also dedicated to my wife, Chu-Chu Wen. She was always with me to overcome all challenges. My family is my best support during my research time. Finally, many thanks to my parterres, Shao-Yu Chen, Fu-Yu Shih, Yueh-Chun Wu, Po-Hsun Ho, Ren-Jye Shiue, Kuang Yao Chen, Po-Hsiang Wang, Tak-Pong Woo, Chiashain Chuang, Yi-Ting Wang, Shun-Tsung Lo, Shu-Wei Wang, Fan-Hung Liu, Tsung-Wei Huang, and Yu-Chuan Lin for sharing many experimental experiences with me during this few years.

Contents

1	Intr	oductio	n	1	
	Refe	erences		2	
2	The	oretical	Background	3	
	2.1	Physic	al Properties of Graphene	3	
		2.1.1	Electrical Structure and Zero Band Gap	3	
		2.1.2	Pseudospin	5	
		2.1.3	Klein Tunneling	6	
		2.1.4	Quantum Hall Effect		
		2.1.5	Shubnikov-de Haas Oscillation and Massless		
			Effective Mass	11	
		2.1.6	Quantum Hall Plateau-Plateau Transition		
		2.1.7	Weak Localization	13	
	2.2	Molyb	odenum Disulfide (MoS ₂)	16	
		2.2.1	Photoconductivity Effect	16	
		2.2.2			
	Refe	erences			
3	Exp	erimen	tal Methods	23	
	3.1		-Free Fabrication		
	3.2		al Property Measurement System		
	3.3	-	d Measurement Systems		
	3.4	-	c Force Microscopy		
	3.5				
			d	28	
		3.5.1	OTS-Functionalized Substrates		
		3.5.2	Two-Terminal Conductance Measurements		
	Refe	erences		30	

xii Contents

4	Distinctive Magnetotransport of Graphene p-n-p Junctions via Resist-Free Fabrication and Controlled Diffusion										
	of N		Contact								
	4.1		uction								
	4.2		ation								
	4.3		imental Results								
	4.4		nstration of p-n Junction Devices								
	4.5	Concl	usion	39							
	Refe	erences		40							
5	Obs	ervatio	n of Quantum Hall Plateau-Plateau Transition								
	and Scaling Behavior of the Zeroth Landau Level										
	in G	rapher	ne p-n-p Junction	41							
	5.1	Introd	uction	41							
	5.2	Fabric	ation	42							
	5.3		imental Results								
		5.3.1	The Doping Effect from Titanium Diffusion	42							
		5.3.2	The Doping Effect Simulated by Theoretical								
			Dipining Model	44							
		5.3.3	Characteristics of Graphene p-n-p Junction Devices								
		5.3.4	Quantum Hall Effect in p-n-p Junction								
		5.3.5	Scaling Behavior								
		5.3.6	The MR and the Distribution of the Energy								
			Levels of the LLs	50							
	5.4	Concl	usion								
	Refe										
,	TC4-		Addition of Description A. Distriction of the description of the descr								
6			Origin of Persistent Photoconductivity in Monolayer	55							
	6.1	_	uction								
	6.2		ation								
	6.3										
	6.4										
	0.4	6.4.1	imental Results and Discussion								
			The PPC Effect in a Monolayer MoS ₂ Transistor								
		6.4.2	Temperature Dependence of PPC Relaxation								
		6.4.3	The Subtract Effect of PPC								
		6.4.4	Discussion of PPC Mechanism	63							
		6.4.5	The Relationship Between the PPC Effect	<i>(</i>							
		(16	and Transport Behavior								
		6.4.6	Fitting of the PPC Relaxation Curves								
		n 4 /	CTALE VOLIAGE DEDENOENCE OF THE PPC	nh							

7	Conclusion	. 73
	References	. 69
	6.5 Conclusion	. 69
	6.4.9 Carrier Mobility Dependence of the PPC	. 68
	6.4.8 Transport Characteristics of the MoS ₂ FET	. 67

Chapter 1 Introduction



1

The Moore's law, which predicts the component density and performance of integrated circuits doubles approximately every two years, has been extended since Gordon E. Moore mentioned this trend in 1965 [1]. The size unit of each element has been made smaller from micrometer to nanometer in the past 50 years, leading to the development of semiconductor industry. However, the yield of devices becomes low when the size unit is recently down to 10 nm. This challenge is not only to develop a new fabrication method but also to improve the quality of the short channel devices. Moreover, finding new materials in which the functionality is good enough to replace Si is crucial.

Graphene, the material that leads to the Nobel prize in 2010, [2] has been marked in the extension of Moore's law in the future since its mobility can be ten times higher than that in a commercial Si-wafer [3]. Molybdenum disulfide (MoS₂) is another material to study in the extension of Moore's law. As high as 10⁸ of a on-off ratio with the subthreshold swing about 70 mV/decade is revealed in the monolayer MoS₂ devices [4–6]. If the substrate with thinner SiO₂ is adapted, the limitation of the subthreshold swing of the 60 mV/decade at room temperature in the complementary metal-oxide-semiconductor (CMOS) devices can be overcome [7]. In addition, using such a monolayer semiconductor with a large band gap as a channel is useful to decrease large intrinsic capacitances and unavoidable current tradeoffs, to minimize the short channel effects at scaling limits [8, 9].

At the beginning of this thesis, we introduce the theoretical background in Chap. 2, which is including some of the basic electrical transport properties of graphene and MoS_2 , the magneto properties of the graphene junction devices, and the optoelectronic properties of MoS_2 . Chapter 3 describes the fabrication methods and experimental set-up. In Chap. 4, we demonstrate the fabrication of graphene junction devices by a one-step and resist-free fabrication method. A full mixing of filling factor in the p-n and p-n-p interface are observed in the magneto transport measurements. The carrier transport in the junction also can be investigated by the temperature dependence at B=0 T. Chapter 5 reveals delocalized mechanism at the zeroth Landau level. The plateau-plateau transition point, which is corresponding to each

2 1 Introduction

Landau level position, can be observed between the quantum Hall plateaus in the graphene junction device.

In Chap. 6, we investigate the persistent photoconductivity (PPC) effect and its mechanism in MoS_2 . Comparing the PPC in suspended MoS_2 with that in substrate-supported MoS_2 devices led us to conclude that PPC originates primarily from extrinsic sources. Moreover, we could correlate the PPC phenomena with percolation transport, whereby carriers transfer among nearest low-potential puddles. In the last chapter, we will summarize the experimental results in this thesis.

References

- 1. G.E. Moore, Tech. Dig. IEDM 21, 11 (1975)
- 2. A.K. Geim, Rev. Mod. Phys. 83, 851 (2011)
- 3. A.K. Geim, K.S. Novoselov, Nat. Mater. 6, 183 (2007)
- 4. A.K. Geim, I.V. Grigorieva, Nature 499, 419 (2013)
- Q.H. Wang, K. Kalantar-Zadeh, A. Kis, J.N. Coleman, M.S. Strano, Nat. Nanotechnol. 7, 699 (2012)
- 6. K. Alam, R.K. Lake, I.E.E.E. Tran, Electron Devices. 59, 3250 (2012)
- 7. J. Jo, C. Shin, Curr. Appl. Phys. 15, 352 (2015)
- 8. M.L. Luisier, M. Antoniadis, D. A. Bokor, J. IEDM Tech. Dig. IEDM. 251–254 (2011)
- 9. Y. Taur. IBM J. Res. Dev. 46, 213 (2002)

Chapter 2 Theoretical Background



2.1 Physical Properties of Graphene

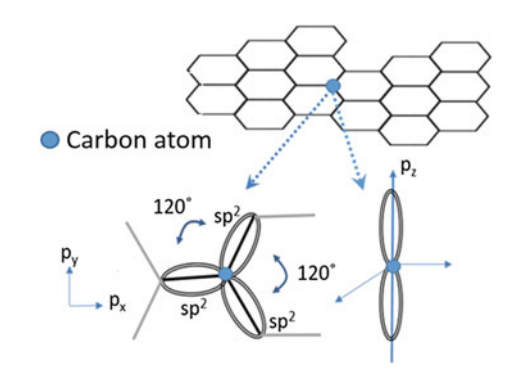
Using a mechanical exfoliation method [1], monolayer graphene, consisting of a two-dimensional layer of carbon atoms on an $\mathrm{SiO}_2/\mathrm{Si}$ substrate of appropriate thickness, can be observed under an optical microscope [2], revealing relativistic quantum mechanics in two-dimensional systems. Therefore, numerous unique characteristics and physical theories can be investigated through experiments on graphene, which can illuminate the potential of this material for future applications. In this chapter, I briefly introduce the novel physical properties of graphene, which are also discussed in later experimental chapters.

Section 2.1.1 describes the linear energy dispersion in the intrinsic band structure of graphene that can be characterized by a Dirac cone. Section 2.1.2 describes pseudospin chirality in the graphene lattice. Section 2.1.3 introduces the Klein tunneling effect in which the carriers can propagate through a potential barrier even if the energy of the carriers is lower than the height of the potential barrier. Sections 2.1.4, 2.1.5, 2.1.6, and 2.1.7 describe magnetotransport theories, corresponding to the quantum Hall effect, Shubnikov–de Haas oscillations, phase transition between the quantum Hall plateau, and weak localization behavior, respectively.

2.1.1 Electrical Structure and Zero Band Gap

Graphene consists of a single layer of carbon atoms. The crystal structure formed by the in-plane σ -bonds between two carbon atoms exhibits a sp²-hybridization system. Each carbon atom contacting with neighbor carbon retains unhybridized π -bonds in the direction of the p_z -orbital, as shown in Fig. 2.1 [3, 4]. The half-filled π -bond makes the dominant contribution to conductance in the transport. The distance between a carbon atom and the nearest three carbon atoms is $a_0 = 1.42 \text{ Å}$

Fig. 2.1 Schematic of the graphene lattice structure with its sp²-hybridized carbon atoms. The in-plane sp² orbitals form σ bonds, and the unhybridized p_z orbitals form π bonds



with separation angle of 120° between the σ -bonds, producing a honeycomb lattice structure.

The lattice vectors in the real space are $\vec{a} = a\hat{x} + b\hat{y}$ and $\vec{b} = a\hat{x} - b\hat{y}$; they are shown in Fig. 2.2a, where $(a,b) = \left(3a_0/2,\sqrt{3}a_0/2\right)$. The corresponding reciprocal lattice in the first Brillouin zone conversion is shown in Fig. 2.2b. The lattice is presented by $\vec{K} = M\vec{A_1} + N\vec{A_2}$, where (M,N) is composed of integers; $\vec{A_1} = \pi/a\hat{x} + \pi/b\hat{y}$ and $\vec{A_2} = \pi/a\hat{x} - \pi/b\hat{y}$ are the basis vectors of the reciprocal space based on the transforming equation:

$$a_i.A_j = 2\pi \delta_{ij}. \tag{2.1}$$

The two sublattice corners, \overrightarrow{K} and \overrightarrow{K}' , exhibit different valleys in the energy contours of the first Birlioun zone condition.

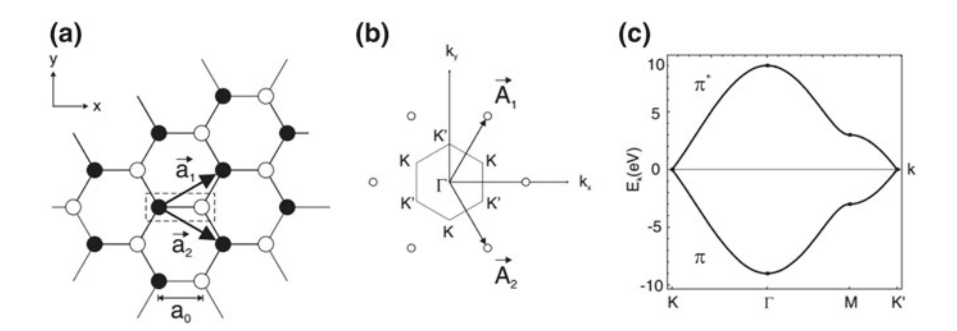


Fig. 2.2 Honeycomb lattice in real and reciprocal space. **a** A unit cell in Honeycomb lattice in real space. A unit cell is constructed on a basis of two carbon atoms, black and white particles marked by the dashed line, in real space. **b** Reciprocal lattice in the first Brillouin zone. The lattice is constructed from two vectors in the reciprocal space. **c** The graphene π -band dispersion in three-dimensional representation as calculated with the original tight-binding approach. (Figures extracted from Ref. [3])

The electronic band structure can be constructed using the first tight-binding analysis [5] due to a covalent solid system, which considers p_z -orbital interaction with the nearest and next-nearest neighbor atoms. The dispersion relation $E_k(k)$ calculated from the Bloch wave function [5] is shown by:

$$E_k = \pm t \sqrt{1 + 4\cos(k_y b)\cos(k_x a) + 4\cos^2(k_y b)},$$
 (2.2)

where the plus sign and minus sign are the upper conduction (π^*) and the lower valance (π) bands, respectively; and the parameter t is the nearest-neighbor hopping energy. Notably, the condition $E_k = 0$ occurs at six corners of the boundary in the first Birlioun zone. When the Fermi level E_F is located in this natural point, the π and π^* -band meet each other at the K and K' points, representing a zero-gap semiconductor or a zero-overlap semimetal. The band structure can be approximated as cones located at the different corners of the Brillouin zone. The cones curve, and the energy dispersion relation is linear; these phenomena indicate a zero effective mass at the natural point. For such relativistic particles, the energy dispersion,

$$E_k = \sqrt{m_0^2 + \hbar^2 k^2},\tag{2.3}$$

can be simplified to $E_k = \hbar k = \hbar v_F |\vec{q}|$ where v_F is the Fermi velocity, \hbar is the Plank constant divided by 2π , \vec{q} is the wave vector in momentum space.

Because half-filled π -bands characterize a linear dispersion around the natural Dirac point, the carrier density can easily be tuned by applying back gate voltage [6]. Figure 2.3 shows the resistivity as a function of the back gate voltage. The Fermi level, E_F , shifted in the valence (conduction) band in the regime of negative (positive) back gate voltage, indicates that the transport carrier is contributed by electrons (holes), causing the resistivity to decrease away from the natural point. Notably, the finite maximum resistance is located at the natural point instead of at infinity because electron holes puddle near the intersection point of the conduction and valence bands [6, 7].

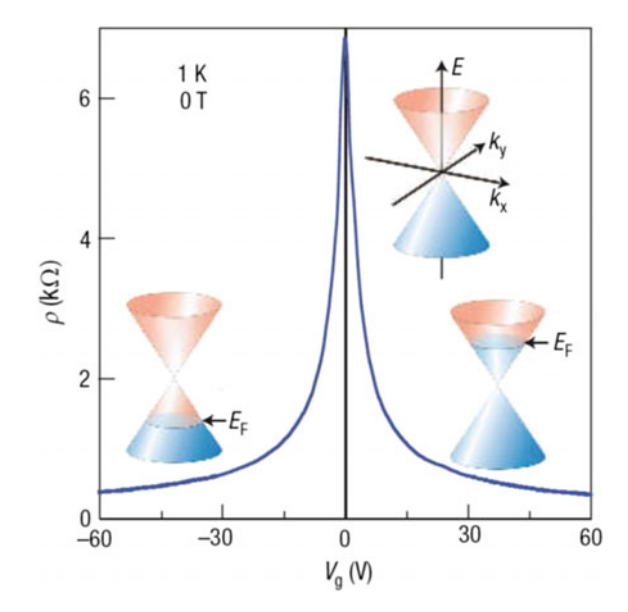
2.1.2 Pseudospin

The band structure calculated with a tight-binding method near the two valleys, K and K', causes the carriers to behave as massless Dirac fermions [5, 8, 9]. The energy-eigenstate equation approximates the orbital wave function near K and K' points by a two-dimensional Dirac Hamiltonian for massless fermions,

$$H = \hbar \nu_F \sigma k, \tag{2.4}$$

where k is a wave vector related to the K and K' points; $\overrightarrow{\sigma}$ is the Pauli matrix [10, 11]. The eigenstate is written as:

Fig. 2.3 Ambipolar electric field effect showing in monolayer graphene. The inset shows the location of Fermi levels in the conical energy spectrum E(k). (Figures extracted from Ref. [6])



$$|k| \ge \frac{1}{\sqrt{2}} e^{ik \cdot r} \begin{pmatrix} -ibe^{-i\theta/2} \\ e^{i\theta/2} \end{pmatrix},$$
 (2.5)

where $\theta(k)$ is the $\tan^{-1} k_y/k_x$ in momentum space; b = 1 or -1 depending on the states above or below the energy at the K and K' points [11]. The eigenstate can be written as a two-component vector that contributes the amplitudes of an electronic wave function on the superposition of the K and K' points. As the result, the electron generated by this vector can be viewed as a pseudospin that replaces the real spin. Therefore, the wavefunction is generated on the superposition of both sublattices by a pseudospin operator which replaces the role of the real spin [12].

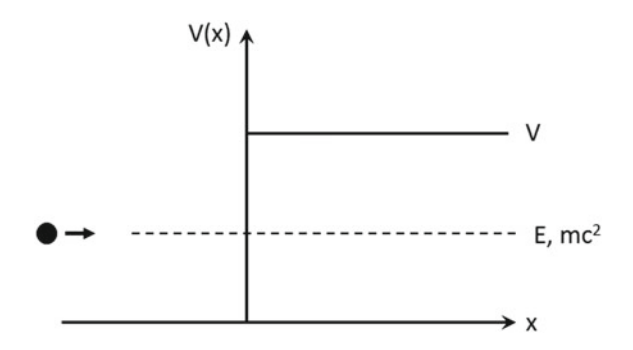
2.1.3 Klein Tunneling

Massless graphene can be used to probe the Klein paradox in the context of relativistic problems [10, 11]. In the normal case, quantum tunneling can be briefly described by a one-dimensional Dirac equation written as:

$$\left(\sigma_x \frac{\partial}{\partial_x} - (E - V(x))\sigma_z + m\right)\Psi = 0, \tag{2.6}$$

where V(x) = V for x > 0 and V(x) = 0 for x < 0, as shown in Fig. 2.4. The reflection and transmission coefficients are:

Fig. 2.4 One-dimensional potential problem. The carrier propagates to the potential well of V(x) = V for x > 0 and V(x) = 0 for x < 0



$$R = \left(\frac{1-\kappa}{1+\kappa}\right)^2 \tag{2.7}$$

and

$$=\frac{4\kappa}{(1+\kappa)^2},\tag{2.8}$$

where $\kappa = \frac{p}{k} \frac{E+m}{E+m-V}$. As in the case of E < V, the reflection and transmission coefficients are R > 1 and T < 0, referring to a counterintuitive relativistic process. Such a counterintuitive paradox is also independent to potential barriers even as $V \to \infty$. To resolve this paradox, the group velocity,

$$v_g \equiv \frac{dE}{dp} = \frac{p}{E - V},\tag{2.9}$$

shows that the momentum should be negative in the case of E < V. It can be divided by the energy-momentum relation and written as:

$$p = -\sqrt{(V - E)^2 - m^2}. (2.10)$$

Therefore, the coefficient parameter is:

$$\kappa = \sqrt{\frac{(V - E + m)(E + m)}{(V - E - m)(E - m)}},$$
(2.11)

where the R and T are satisfied with values between 0 and 1. But this does not resolve the problem that the transmission coefficient is still nonzero in the case of $V \to \infty$, indicating that quantum tunneling happens in the relativistic transport. To observe the tunneling effect, the potential step should be over the Compton length:

$$\lambda = \hbar/mc,\tag{2.12}$$

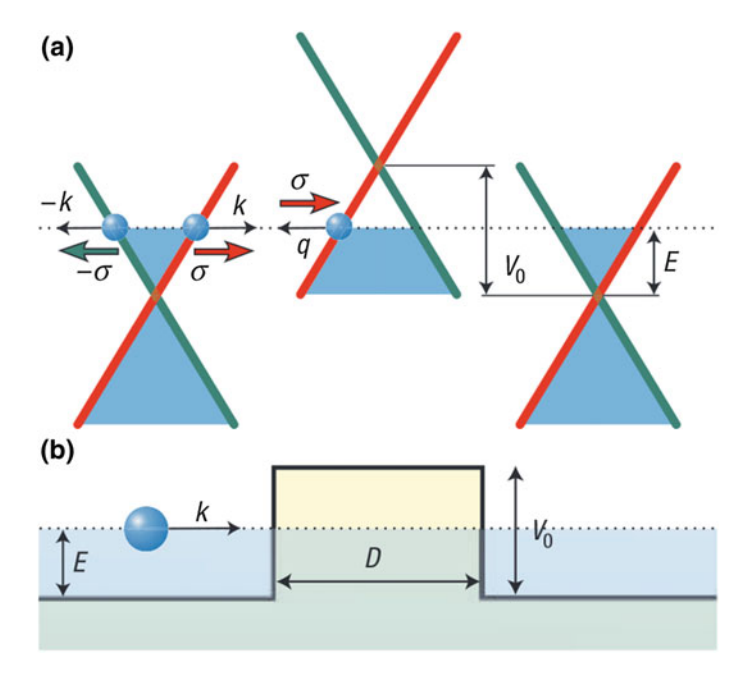


Fig. 2.5 Tunneling behavior in the graphene junction. a Schematic of the graphene junction. In the middle Dirac cone, the Dirac point is mismatched with cones on both sides because of the doping effect. b The schematic diagram shows the potential barriers of height V_0 and width D, which correspond to the junction in (a). The Fermi energy E is lower than V_0 , which shows the conduction (valence) band outside (inside) the barrier. (Figure extracted from Ref. [14])

which requires enormous electric fields of 10¹⁶ MV/cm [13].

Graphene allows one to observe relativistic quantum tunneling in the context of the Klein paradox [14]. Figure 2.5a shows a graphene junction induced by a doping effect, which can be analogous to the case of one-dimensional potential well shown in Fig. 2.5b. The red line shows the same pseudospin σ direction for an electron with energy E and a hole with -E. The absence of backscattering is due to the carrier momentum perfectly changing its sign as the carrier changes from electron to hole. According to the Klein paradox theory, this electron and hole go through the potential well as particle and antiparticle, which makes it highly probable that the carriers pass through the barrier.

2.1.4 Quantum Hall Effect

The quantum Hall effect is a fundamental physical phenomenon in which electrons are confined in a two-dimensional system, which shows the quantization of cyclotron orbits in a magnetic field directed perpendicular to the plane [15]. The charged

particles only occupy certain discrete energy levels, called the Landau levels (LL). Each filled LL contributes one e^2/h of quantized conductance value to the Hall conductance (per spin, per valley). For the quantum Hamiltonian including a B field, the general form is given as:

$$H = \frac{1}{2m^*} \left(\vec{p} + \frac{e}{c} \vec{A} \right)^2 - e\phi.$$
 (2.13)

Applying a perpendicular magnetic field in the x-y plane, the equation can be written as:

$$H = \frac{1}{2m^*} \Big[p_x^2 + (p_y - eBx)^2 \Big]. \tag{2.14}$$

If we assume free electron motion in the y-direction, the eigenfunction can be written as:

$$\psi(x, y) = \varphi(x)e^{-ik_y y}. \tag{2.15}$$

Based on the Hamitonian and eigenfunction, the Schrödinger equation can be obtained as:

$$\frac{1}{2m^*} \left[p_x^2 + \left(\hbar k_y - eBx \right)^2 \right] \psi \equiv \frac{1}{2m^*} \left[p_x^2 + \frac{1}{2} m^* \omega_c^2 (x - x_0)^2 \right], \tag{2.16}$$

where $\omega_c = \frac{eB}{m^*}$ and $\omega_c = x_0$ are the cyclotron frequency and the center of oscillation, respectively. The eigenenergy is given by

$$E_N = \hbar\omega \left(N + \frac{1}{2}\right),\tag{2.17}$$

where ω is the cyclotron frequency, N is an integer representing LL index, and m^* is effective mass. In the ideal system, the energy separation is $\hbar\omega$ between the LLs, as shown in Fig. 2.6a. However, in a real system, the LLs will be broadened by the appearance of disorder, as shown in Fig. 2.6b. Only the states around the middle of the LLs are extended and contribute to conductance.

In comparison with a classical semiconductor, LL formation in graphene has been studied using 2+1-dimensional quantum electrodynamics, and the LL energy is written as [16]:

$$E_n = \pm \sqrt{2e\hbar v_F^2 |N|B},\tag{2.19}$$

where \hbar is the Planck constant divided by 2π , N represent the electron-like (n > 0) or hole-like (n < 0) LLs. Based on Eq. 2.19, the E_n is proportional to \sqrt{N} , exhibiting unequally spaced LLs. This equation shows the zeroth LL exists at $E_n = 0$, which is also different from the two-dimensional material shown in Fig. 2.7. Figure 2.8 shows

Fig. 2.6 Landua level showing in the density of states as a function of energy. a The LL in an ideal system. b The LL broadening in a real device

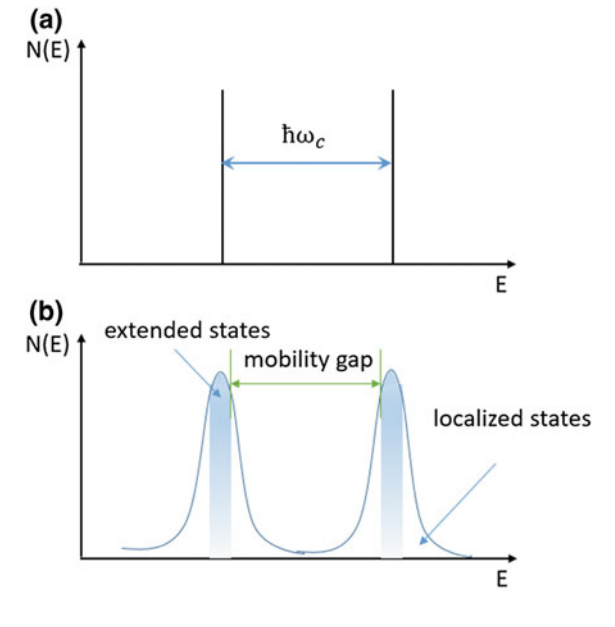
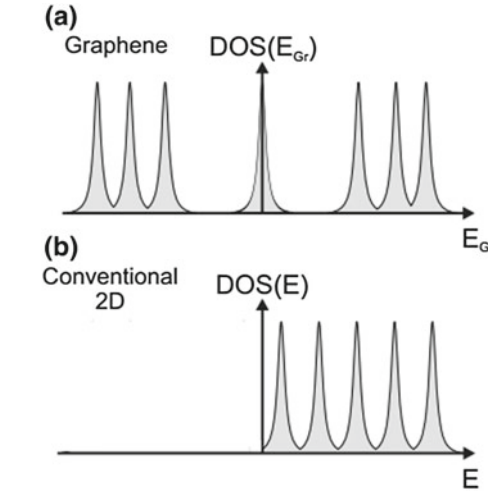


Fig. 2.7 Unique property of the zeroth LL in graphene. a The unique zeroth LL and the nonequal energy separation between LLs shown in graphene. b equal energy separation in a conventional two-dimensional material. (Figures extracted from Ref. [3])



the quantum Hall effect in the graphene device. The longitudinal magnetoresistance shows the conductance goes to zero, corresponding to the Hall resistance plateau position. The Hall conductance shows:

$$G = 4(n+1/2) e^2/h,$$
 (2.20)

where the fact of 4 is induced by spin-valley degeneracy [17].

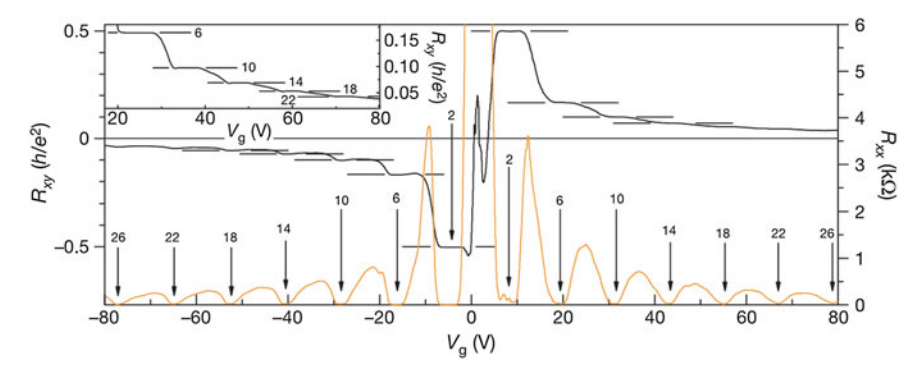


Fig. 2.8 Quantum Hall effect in graphene. Hall resistance (black) and magneto resistance (orange) as functions of back gate voltage at 9 T. Inset: high level of the filling factor measured at 30 mK. (Figures extracted from Ref. [9])

Moreover, the graphene junction has been experimentally realized by the dual gates controlling different carrier densities in two adjacent regions. Because of the ambipolar characteristics of graphene, the junction type can be tuned to a p-p, p-n, or n-n condition. The electron-hole symmetry also causes symmetrical appearances of the quantum Hall effect on both sides of the Dirac point in this material, resulting the number of $n = |\nu|$ edge modes in each of the quantized states. In the bipolar regime, the densities are $\nu > 0$ and $\nu < 0$ on either side of the boundary with opposite chirality. When the magnetic filed is applied, the mixing edge state exists in the p-n and p-n-p interface induce conductance has the fraction of e^2/h . The junctions also present interesting phenomena reflecting the massless Dirac carriers during the transport. The new plateau can be explained using the theory of quantum-chaotic transport [18–21]. The carriers propagated along the interface are from both the n and p reservoirs; they move into the edge modes. Until the carriers are fulfilled in the edge states, the carriers on both sides return to the reservoirs with backscattering [22, 23].

2.1.5 Shubnikov-de Haas Oscillation and Massless Effective Mass

In a real device, the LLs are broad; they do not exhibit sharp peaks like the one shown in Fig. 2.6a. The extended states located at the center of LLs contribute conductance values within k_BT of the Fermi energy. On the LL tail, the carriers remain localized in those states, revealing no contribution to conductance. Therefore, the alternate extended and localized states in each LL are swept through the Fermi energy, revealing oscillations in the longitudinal resistance, shown in Fig. 2.9a, which are called Shubnikov–de Haas (SdH) oscillations. The left inset shows that in a fixed

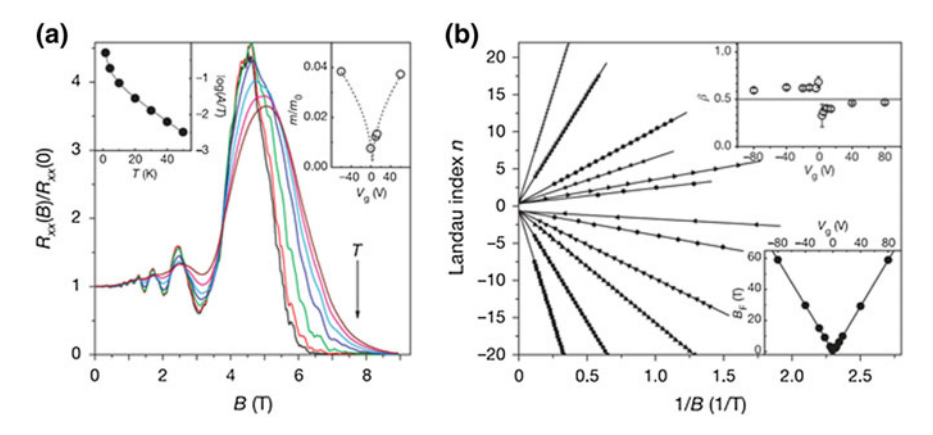


Fig. 2.9 Shubnikov–de Haas oscillation and LL fan diagram. a SdH oscillation measured in 0 T < B < 9 T. b LL index versus $1/B_n$ at different gate voltages. (Figures extracted from Ref. [9])

magnetic field, the amplitude of oscillation is decreased by increasing temperature. In addition, effective mass can also be extracted by SdH oscillation as shown in the right inset. It is notable that mass vanishes at the Dirac point and can be fitted by the effective relativistic mass:

$$m_c = \frac{E_F}{v_F^2} = \sqrt{\pi \, \hbar^2 n_s / v_F^2}.$$
 (2.21)

Based on semiclassical magneto oscillation, the longitudinal resistance can be also written as:

$$\Delta R_{xx} = R(B, T) \cos \left[2\pi \left(\frac{B_F}{B} + \frac{1}{2} + \beta \right) \right], \tag{2.22}$$

where R(B,T), B_F , β are SdH oscillation amplitudes, frequency of oscillation is 1/B, and Berry's phase represents the quantum phase of pseudo spinor in the range of $0 < \beta < 1$. Normally, Berry's phase is 0 or 1 for trivial cases with equivalent magneto resistance. The fact that $\beta = 1/2$ implies that Dirac particles exist [24], which can be observed in the experiment through values of $1/B_n$ at the value of Nth minimum of R_{xx} against their LL index n, as shown in Fig. 2.9b. The linear relationship is extrapolated to the y-axis at 1/2 (-1/2) for the electron (hole) at all back gate voltages. The upper inset shows the β is achieved at various back gate voltages, and the lower inset shows that the slope of linear fitting indicates B_F . A half-integral quantum Hall effect (Eq. 2.20) is also predicted the existence of a non-zero Berry's phase.

2.1.6 Quantum Hall Plateau-Plateau Transition

In the quantum Hall regime the Hall resistance exhibits a plateau corresponding to zero longitudinal resistance when E_F is located between the LLs and increases the value of ${\rm e}^2/h$ when E_F is across one of the nondegenerate LLs, as shown in Fig. 2.10a; this is associated with the broadened LL shown in Fig. 2.10b. Therefore, the temperature or magnetic dependence of scaling behavior in the quantum Hall regime can be used to detect LL conditions. It is more useful to investigate graphene which have the zeroth LL and fourfold degenerate LLs contributed by spin-valley degeneracy. Figure 2.11 shows the temperature independence of Hall plateau-plateau transition points in graphene devices. A scaling exponent κ can then be derived and the maximum slope of ${\rm d}\sigma_{xy}/{\rm d}\nu$ diverges as $T^{-\kappa}$ in the transition region. The exponent is of 0.40 ± 0.02 , in accordance with the universal scaling theory [25–27].

2.1.7 Weak Localization

Weak localization (WL) is a physical effect by which the carriers propagated with two time-reversed paths, but in opposite directions that return to the original position (point A shown in Fig. 2.12), causing resistivity to increase [29]. The localization caused by weak disorder happens in the metallic and diffusive regimes, and requires $k_F l \gg 1$ where k_F is the Fermi wave vector and l is the elastic scattering length [17].

Electron motion in the disordered system is characterized by numerous collisions. If a collision is elastic, the electrons scattered by impurities or other electrons retain consistent momentum and energy after experiencing scattering, which reveals phase coherence in the electron wave function, $\tau_{\phi} \gg \tau_{e}$. Therefore, quantum interference occurs, and the total probability of finding the electrons at A can be written as [30]:

$$P_{[A,B]} = \sum_{i,j} A_i A_j^* = \sum_i |A_i|^2 + \sum_{\substack{i,j\\i\neq i}} A_i A_j^*,$$
 (2.23)

where A_i and A_j are probability amplitudes. The first term is the sum of the individual probability density contributed by the classical result, while the second term is the sum of the interference probability density, known as quantum correlation. Because no phase difference exists between both time-reversal symmetry paths, the equation can be given as [30]:

$$P_{[A,A]} = \sum_{i,j} A_i A_j^* = \sum_i |A_i|^2 + \sum_i A_i A_i^* = 2 \sum_i |A_i|^2.$$
 (2.24)

The probability density is twice as large as the classical result, showing that constructive interference occurring at the original point A will enhance resistivity.

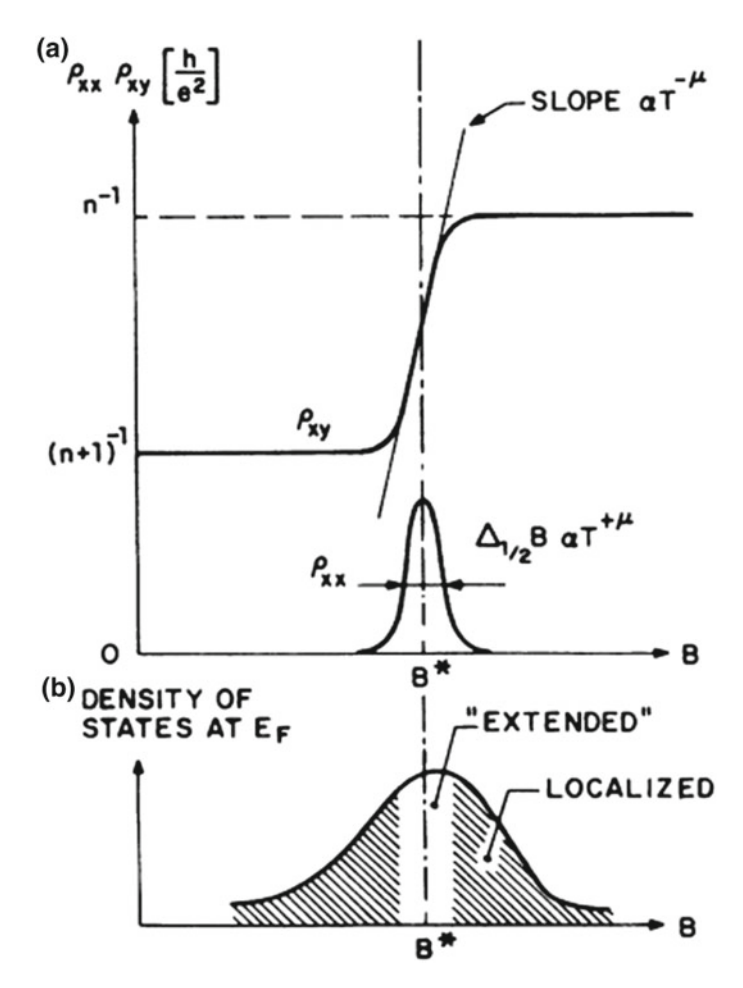


Fig. 2.10 Detail of LL condition corresponding to the resistance in the longitudinal and orthogonal directions. **a** Plateau in the Hall resistance with distance of h/e^2 from the neighbor and corresponding to zero longitudinal resistance. **b** Localized state at LL tails and extended state in the middle. (Figures extracted from Ref. [26])

If inelastic collisions exist during the transport, the phase coherence will be completely broken, which can be induced by increasing temperature to causes electron scattering with phonons or by increasing perpendicular magnetic field to break time-reversal symmetry [31]. However, the result of the breaking of phase coherence of the time-reversed loop will suppress the weak localization effect. Applying the magnetic field is a method commonly used to investigate the weak localization effect. In a diffusive transport regime, $\frac{k_B T \tau}{\hbar} > 1$, the magneto conductivity can be corrected by a weak localization term in the conventional two-dimensional electron gas system, given by [32]:

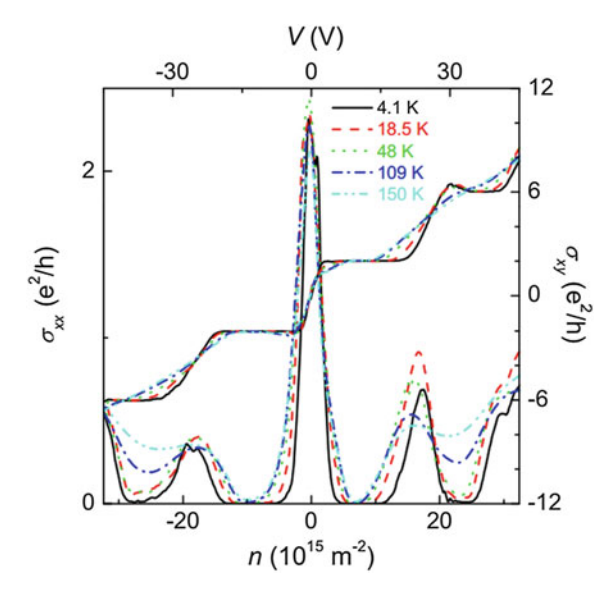


Fig. 2.11 Plateau-plateau transition points in graphene device. Temperature independent transition points are observed between the quantum Hall plateau. (Figures extracted from Ref. [28])

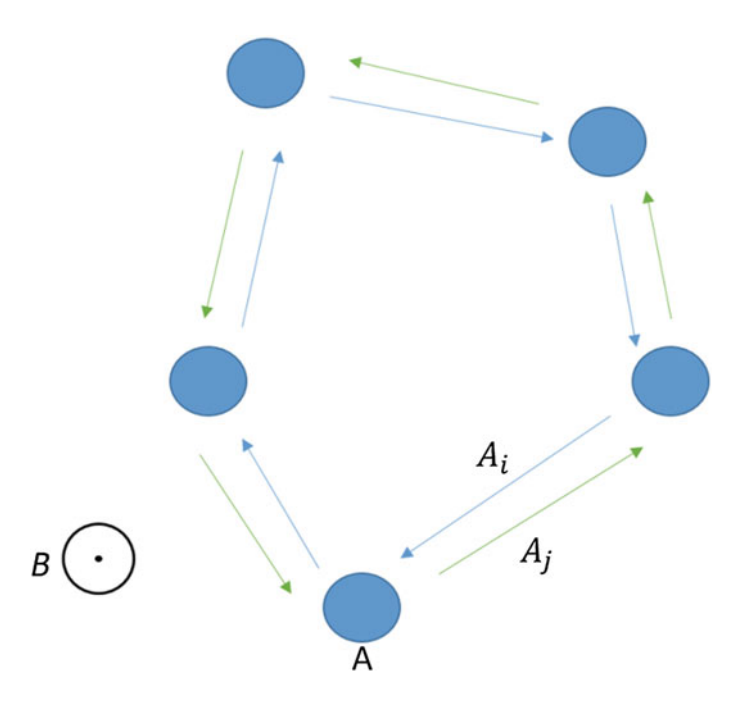


Fig. 2.12 Two identical time-reversed paths in opposite directions. The carrier retains exactly the same phase and the same amplitude as the wave function during the process of elastic collision

$$\Delta \sigma_{xx}^{wl} = G_0 \left\{ \psi \left(\frac{1}{2} + \frac{B_{\varphi}}{B} \right) - \psi \left(\frac{1}{2} + \frac{B_{tr}}{B} \right) + \ln \left(\frac{B_{tr}}{B_{\varphi}} \right) \right\}, \tag{2.25}$$

where ψ is the digamma function, $G_0 = \frac{e^2}{\pi h}$, $B_{tr} = \frac{\hbar}{2el^2}$, $B_{\varphi} = \frac{\hbar}{4el_{\varphi}^2}$, l_{φ} is the defacing length, and l is the mean free path. Compared to graphene in the diffusive transport regime, the correction of WL was derived by McCann et al. [33]:

$$\Delta \sigma_{xx}^{wl} = G_0 \left\{ F\left(\frac{B}{B_{\varphi}}\right) - F\left(\frac{B}{B_{\varphi} + 2B_{iv}}\right) - 2F\left(\frac{B}{B_{\varphi} + B_{iv} + B_z}\right) \right\}, \quad (2.26)$$

with $F(z) = \ln z + \psi(\frac{1}{2} + \frac{1}{z})$, $G_0 = \frac{e^2}{\pi h}$, $B_{\varphi,i,*} = \frac{\hbar}{4De\tau_{\varphi,i,*}}$, where τ_{φ} , τ_i , and τ_* are decoherence time, intervalley scattering time, and intravalley scattering time, respectively.

2.2 Molybdenum Disulfide (MoS₂)

By a method similar to the exfoliation of graphene from graphite, bulk molybdenum disulfide with a weak van der Waal interaction between its layers can be easily exfoliated to a monolayer form with a 6.5 Å thickness, as shown in Fig. 2.13. Single-layer MoS_2 also has a hexagonal structure, which is composed with two planes of molybdenum atoms and one plane of sulfur atoms, as shown in Fig. 2.14. Its transport properties include an on/off current ratio as high as 10^8 because of the 1.8 eV direct bandgap [34].

2.2.1 Photoconductivity Effect

Photoconductivity is an optical and electrical phenomenon that manifests itself as a positive correction to conductivity caused by the absorption of electromagnetic radiation. When light has an energy value larger than the energy gap of illuminated material, the number of free electrons and holes increases in the conduction and valence bands, as shown in Fig. 2.15a, increasing its electrical conductivity. If light is terminated, the conductivity will return to its original value because of the recombination of electrons and holes, as shown in Fig. 2.15b. This behavior is usually observed in semiconductors because their energy gaps correspond to the emission energy levels of visible light.

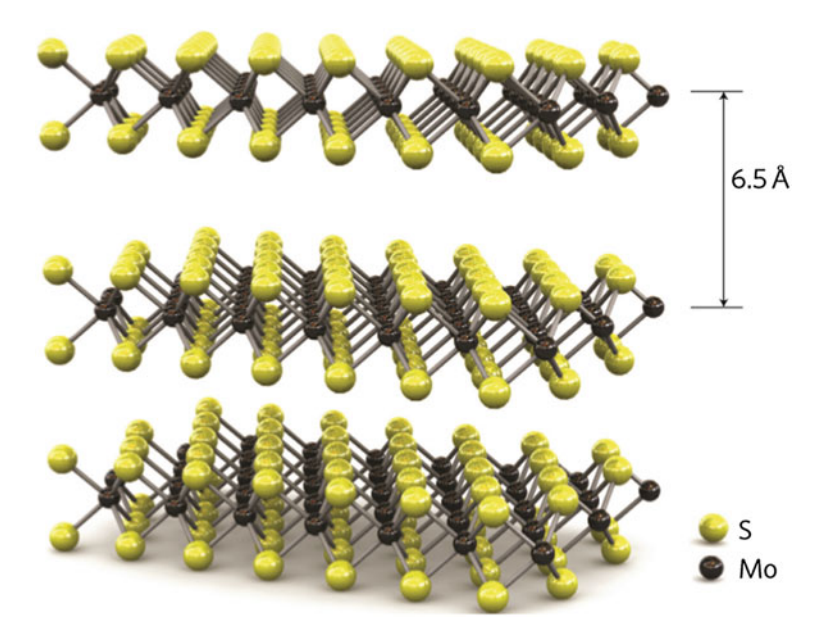


Fig. 2.13 Schematic of Bulk MoS_2 . It is stacked in a hexagonal S-Mo-S structure; each layer is 6.5 Å thick. (Figures extracted from Ref. [34])

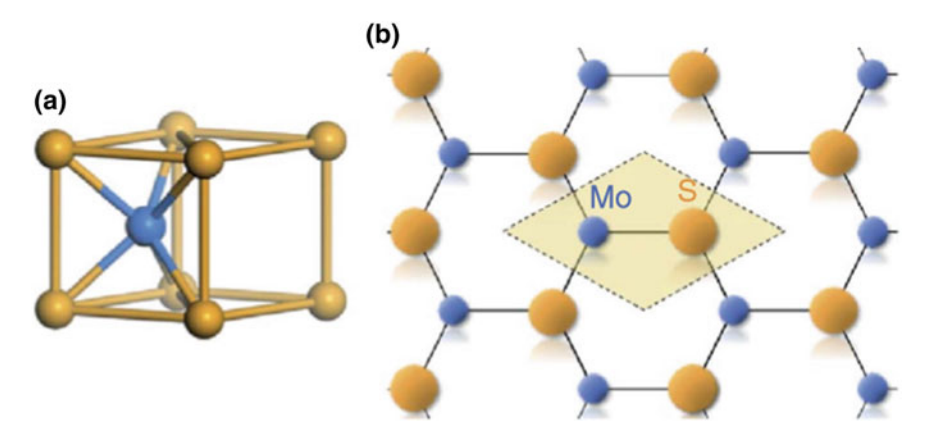


Fig. 2.14 a Trigonal prismatic structure in MoS₂. b Mo-S unit cell in the Honeycomb periodic lattice structure. (Figures extracted from Ref. [35])

2.2.2 Persistent Photoconductivity

Unlike the photoconductivity effect, photo-induced current tends to persist for a long period of time after the light has been terminated. The persistent photoconductivity (PPC) increases carrier density and transport mobility in the channel. Its mecha-

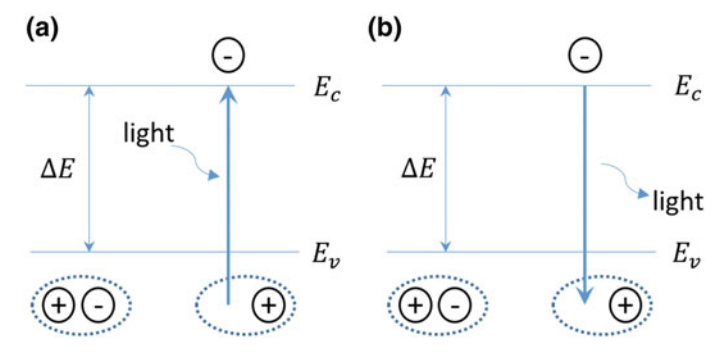


Fig. 2.15 a Electron generation process. Electron has enough energy to jump from conduction band to valence band after illumination. b Electron-hole recombination after illumination was terminated

nism is related to the possibility of instabilities such as charge trapping and often is investigated by decay kinetics as a function of temperature dependence. The large lattice relaxation (LLR), microscopic barrier (MB), and random local potential fluctuations (RLPF) models are possible models to explain the PPC mechanism after illumination.

In the LLR model, electrons are photoexcited from deep-level traps, and an energy barrier prevents the recapture of the electrons [36, 37], resulting in the PPC effect. As shown in Fig. 2.16, the electrons are excited from the trapped state (D curve) to

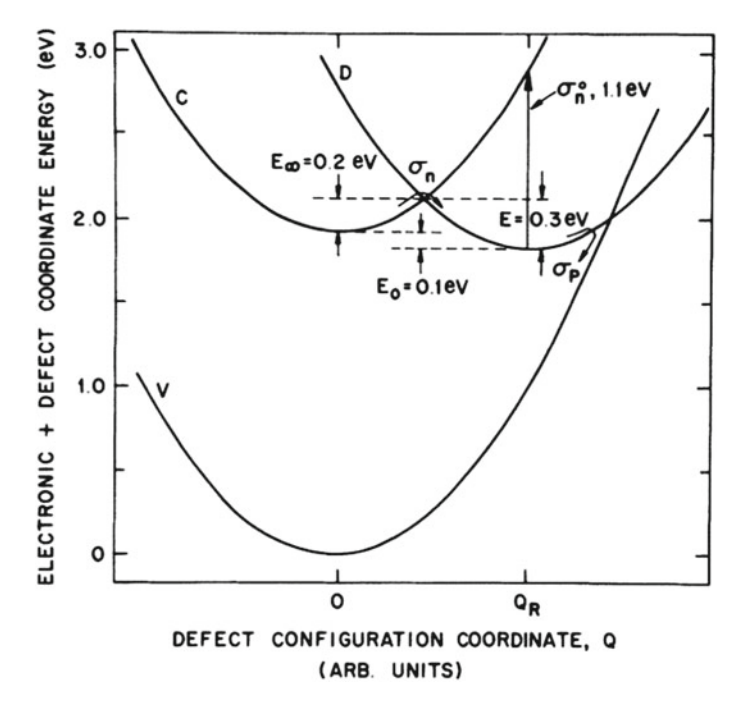
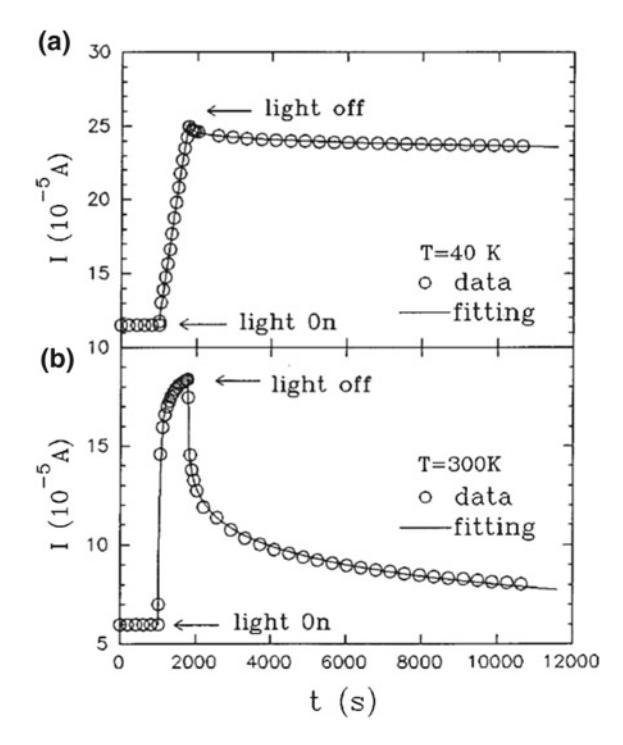


Fig. 2.16 Mechanism of LLR model in the study of PPC effect [37]

Fig. 2.17 PPC effect at a 300 K and b 40 K. Based on the LLR model, the photocurrent at a low temperature is more persistent than the photocurrent at room temperature, showing in a two-dimensional electron gas system [39]

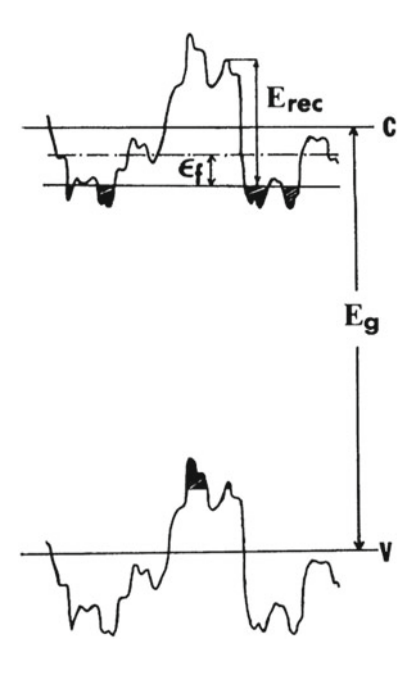


a conduction band (C curve) by light emission. After illumination, the PPC is more pronounced at low temperatures because the probability of recapture is related to thermally activated processes, as shown in Fig. 2.17. Another feature of the PPC that results from LLR is that a photocurrent can be activated by excitation from deep-level traps to conduction bands [38] with energies below that of the bandgap, which also contradicts the observed dependence of the PPC on the excitation energy.

The MB is another mechanism for PPC in which photoexcited electron-hole pairs are spatially separated by a macroscopic potential barrier, followed by charge accumulation or trapping by barriers or spacers [40, 41]. Recent studies on various structures, including MoS₂/graphene [42], quantum-dot/graphene [43] and chlorophyll/graphene [44] heterostructures, demonstrated noticeable PPC phenomena because of this MB model. However, there were no such artificially created structures in our MoS₂ devices that could yield a macroscopic potential barrier. The PPC effect in the MB model also follows a single-exponential decay [40], unlike the stretched exponential decay that was observed in our samples.

Finally, in the RLPF model [45–47], local potential fluctuations arise either because of intrinsic disorders in the materials or extrinsic charged impurities. Therefore, low-energy electrons and holes become localized in potential minima and are spatially separated, as shown in Fig. 2.18, resulting in a long recombination lifetime. The thermal excitation of carriers to higher energy states above the mobility edge produces a photocurrent after the irradiation has been terminated, resulting in the

Fig. 2.18 RLPF model shows that the carriers are excited by light emission and filled in the trap state [47]



PPC effect. At low temperatures, the carriers are well-confined inside charge traps and negligible PPC is observed. This RLPF model has been widely used to explain PPC in II–VI compound semiconductors [45, 46, 48].

References

- K.S. Novoselov, A.K. Geim, S.V. Morozov, D. Jiang, Y. Zhang, S.V. Dubonos, I.V. Grigorieva, A.A. Firsov, Science 306, 666 (2004)
- R.R. Nair, P. Blake, A.N. Grigorenko, K.S. Novoselov, T.J. Booth, T. Stauber, N.M.R. Peres, A.K. Geim, Science 320, 1308 (2008)
- 3. T.J.B.M. Janssen, A. Tzalenchuk, S. Lara-Avila, S. Kubatkin, V.I. Fal'ko, Rep. Prog. Phys. 76, 104501 (2013)
- 4. M. Mecklenburg, B.C. Regan, Phys. Rev. Lett. **106**, 116803 (2011)
- 5. P.R. Wallace, Phys. Rev. 71, 622 (1947)
- 6. A.K. Geim, K.S. Novoselov, Nat. Mater. 6, 183 (2007)
- Y.W. Tan, Y. Zhang, K. Bolotin, Y. Zhao, S. Adam, E.H. Hwang, S. Das Sarma, H.L. Stormer, P. Kim, Phys. Rev. Lett. 99, 246803 (2007)
- 8. K.S. Novoselov, A.K. Geim, S.V. Morozov, D. Jiang, M.I. Katsnelson, I.V. Grigorieva, S.V. Dubonos, A.A. Firsov, Nature **438**, 197 (2005)
- 9. Y. Zhang, Y.-W. Tan, H.L. Stormer, P. Kim, Nature 438, 201 (2005)
- 10. T. Ando, T. Nakanishi, R. Saito, J. Phys. Soc. Jpn. 67, 2857 (1998)
- P.L. McEuen, M. Bockrath, D.H. Cobden, Y.-G. Yoon, S.G. Louie, Phys. Rev. Lett. 83, 5098 (1999)
- 12. N.M.R. Peres, Rev. Mod. Phys. 82, 2673 (2010)
- 13. W. Greiner, B. Mueller, J. Rafelski. (Springer, Berlin, 1985)

References 21

- 14. M.I. Katsnelson, K.S. Novoselov, A.K. Geim, Nat. Phys. 2, 620 (2006)
- 15. E.M.L.L.D. Landau, Theor. Phys., vol. 3 (Butterworth-Heinemann, Oxford)
- 16. Y. Zheng, T. Ando, Phys. Rev. B 65, 245420 (2002)
- 17. F.D.M. Haldane, Phys. Rev. Lett. **61**, 2015 (1988)
- 18. C.W.J. Beenakker, Rev. Mod. Phys. 69, 731 (1997)
- 19. H.U. Baranger, P.A. Mello, Phys. Rev. Lett. 73, 142 (1994)
- 20. O. Agam, I. Aleiner, A. Larkin, Phys. Rev. Lett. 85, 3153 (2000)
- S. Oberholzer, E.V. Sukhorukov, C. Strunk, C. Schönenberger, T. Heinzel, M. Holland, Phys. Rev. Lett. 86, 2114 (2001)
- 22. D.A. Abanin, L.S. Levitov, Science 317, 641 (2007)
- 23. J.R. Williams, L. DiCarlo, C.M. Marcus, Science 317, 638 (2007)
- 24. G.P. Mikitik, Y.V. Sharlai, Phys. Rev. Lett. 82, 2147 (1999)
- 25. H.P. Wei, D.C. Tsui, M.A. Paalanen, A.M.M. Pruisken, Phys. Rev. Lett. 61, 1294 (1988)
- 26. A.M.M. Pruisken, Phys. Rev. Lett. 61, 1297 (1988)
- 27. B. Huckestein, Rev. Mod. Phys. 67, 357 (1995)
- A.J.M. Giesbers, U. Zeitler, L.A. Ponomarenko, R. Yang, K.S. Novoselov, A.K. Geim, J.C. Maan, Phys. Rev. B 80, 241411 (2009)
- 29. B.L. Altshuler, D. Khmel'nitzkii, A.I. Larkin, P.A. Lee, Phys. Rev. B 22, 5142 (1980)
- 30. P.M. Mensz, R.G. Wheeler, Phys. Rev. B **35**, 2844 (1987)
- 31. C.W.J. Beenakker, H. van Houten, in *Solid State Physics*, ed. by E. Henry, T. David (Academic Press, 1991), p. 1
- 32. S. Hikami, A.I. Larkin, Y. Nagaoka, Prog. Theor. Phys. **63**, 707 (1980)
- E. McCann, K. Kechedzhi, V.I. Fal'ko, H. Suzuura, T. Ando, B.L. Altshuler, Phys. Rev. Lett. 97, 146805 (2006)
- B. Radisavljevic, A. Radenovic, J. Brivio, V. Giacometti, A. Kis, Nat. Nanotechnol. 6, 147 (2011)
- 35. T. Cao, G. Wang, W. Han, H. Ye, C. Zhu, J. Shi, Q. Niu, P. Tan, E. Wang, B. Liu, J. Feng, Nat. Commun. 3, 887 (2012)
- 36. R.J. Nelson, Appl. Phys. Lett. 31, 351 (1977)
- 37. D.V. Lang, R.A. Logan, Phys. Rev. Lett. 39, 635 (1977)
- 38. Y.C. Lee, J.L. Shen, K.W. Chen, W.Z. Lee, S.Y. Hu, K.K. Tiong, Y.S. Huang, J. Appl. Phys. **99** (2006)
- 39. J.Z. Li, J.Y. Lin, H.X. Jiang, M. Asif Khan, Q. Chen, J. Appl. Phys. 82, 1227 (1997)
- 40. H.J. Queisser, D.E. Theodorou, Phys. Rev. B 33, 4027 (1986)
- 41. T.N. Theis, S.L. Wright, Appl. Phys. Lett. 48, 1374 (1986)
- 42. K. Roy, M. Padmanabhan, S. Goswami, T.P. Sai, G. Ramalingam, S. Raghavan, A. Ghosh, Nat. Nanotechnol. 8, 826 (2013)
- G. Konstantatos, M. Badioli, L. Gaudreau, J. Osmond, M. Bernechea, F.P.G. de Arquer, F. Gatti, F.H.L. Koppens, Nat. Nanotechnol. 7, 363 (2012)
- 44. S.-Y. Chen, Y.-Y. Lu, F.-Y. Shih, P.-H. Ho, Y.-F. Chen, C.-W. Chen, Y.-T. Chen, W.-H. Wang, Carbon 63, 23 (2013)
- 45. H.X. Jiang, J.Y. Lin, Phys. Rev. B 40, 10025 (1989)
- 46. H.X. Jiang, J.Y. Lin, Phys. Rev. Lett. 64, 2547 (1990)
- 47. H.X. Jiang, G. Brown, J.Y. Lin, J. Appl. Phys. 69, 6701 (1991)
- 48. A.S. Dissanayake, S.X. Huang, H.X. Jiang, J.Y. Lin, Phys. Rev. B 44, 13343 (1991)

Chapter 3 Experimental Methods



This chapter describes the fabrication of the graphene- and MoS₂-based devices and the experimental set-up. It is composed of four parts. Section 3.1 describes the fabrication method of making devices without resist. In Sect. 3.2, we introduce the physical property measurement system which was used to perform transport measurement in high magnetic fields and at cryogenic temperatures. Next, Sect. 3.3 shows the measurement system which consists of a cryogenic system with the spectrometer for optical measurement at low temperatures and high vacuum. Finally, Sects. 3.4 and 3.5 briefly describe our atomic force microscopy measurement system and the substrate treatment with OTS molecule for improving the device quality, respectively.

3.1 Resist-Free Fabrication

We developed a resist-free fabrication method, which is designed for making high-quality devices, to investigate the transport and magneto transport behaviors of 2D materials. Compared to conventional lithography-based fabrication, resist-free fabrication has several advantages, including the reduction of electron scattering from resist residues; implementing fewer steps to reduce the environmental influences; using a shadow mask to leave the sample surface contact-free; and realizing electrode geometry with simpler procedures. Recently, residue-free fabrication has been demonstrated in fabricating high-quality graphene devices, [1–7] for example, those with stencil masks for multi-terminal measurements [5] and focused electron beam for local doping [8].

The procedures are described as follows. First, a 2.5-mm-diameter hole is drilled on a stainless steel sheet with a thickness of 0.1 mm. The diameter is designed to be smaller than 3.5 mm in order to fit the commercial TEM grids, as shown in Fig. 3.1a. We first drop some PMMA over the hole. As shown in Fig. 3.1b, most of the PMMA is absorbed by filter paper under the steel, except for those remaining at the hole edge. TEM grid can be attached on the steel by residue resist. After backing at 90 °C

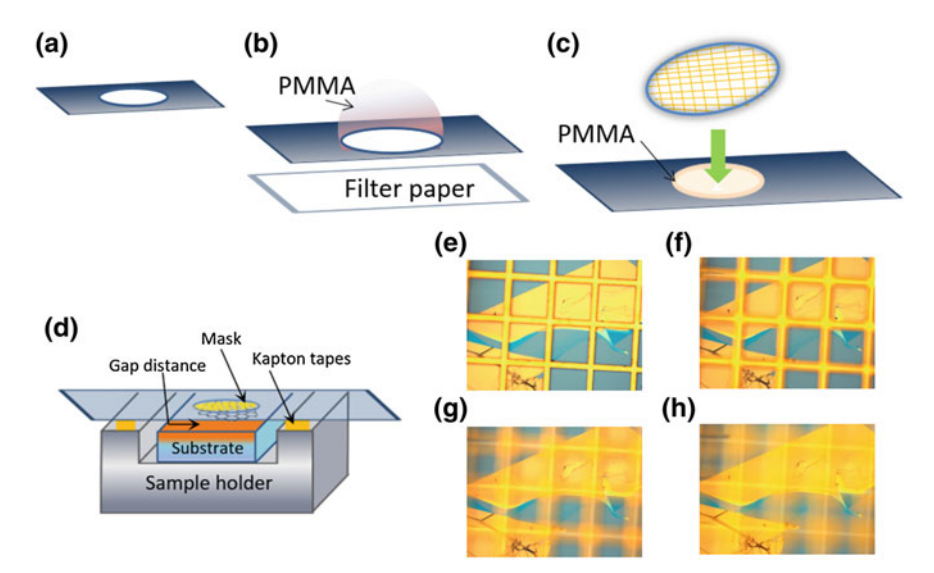


Fig. 3.1 a-c The fabrication processes of the shadow mask. d Schematic showing the gap distance between the mask and graphene is increased by inserted Kapton tapes. e-h are OM images in which the different focal distances between the mask and graphene are 18, 60, 80, and 130 μ m, respectively

for 30 s, the shadow mask is finished and is shown in Fig. 3.1c, on which no further patterning is needed. We then align graphene with respect to the shadow mask by using a homemade xyz 3-axis manipulator under an optical microscope. To achieve controllable diffusive electrode patterns after metallization, controlling the distance between shadow mask and graphene sample is crucial. The gap can be adjusted by adding layers of gaskets (Kapton tapes, 15–20 μm per layer with 5 μm flatness variation of TEM grids) below the shadow mask, as shown in Fig. 3.1d. The distance of gap is further confirmed by measuring the focal distance of graphene and TEM grids with $100\times$ objective under a microscope. Figure 3.1e–h show OM images with different focal distances. The separation of 18 μm was found while focusing separately on the graphene, and the grid in Fig. 3.1e. As the separation increased to 60, 80, and 130 μm , shown in Figure (f)–(h), the image of grid is getting out of focus. After aligning the TEM grid to graphene with a designated distance, Ti/Au (5 nm/55 nm) was deposited as electrodes using an electron-beam evaporator at a base pressure of 1.0×10^{-7} Torr.

3.2 Physical Property Measurement System

Physical property measurement system (PPMS) (Quantum Design) allows researchers to investigate many physical quantities of a device in an open architecture

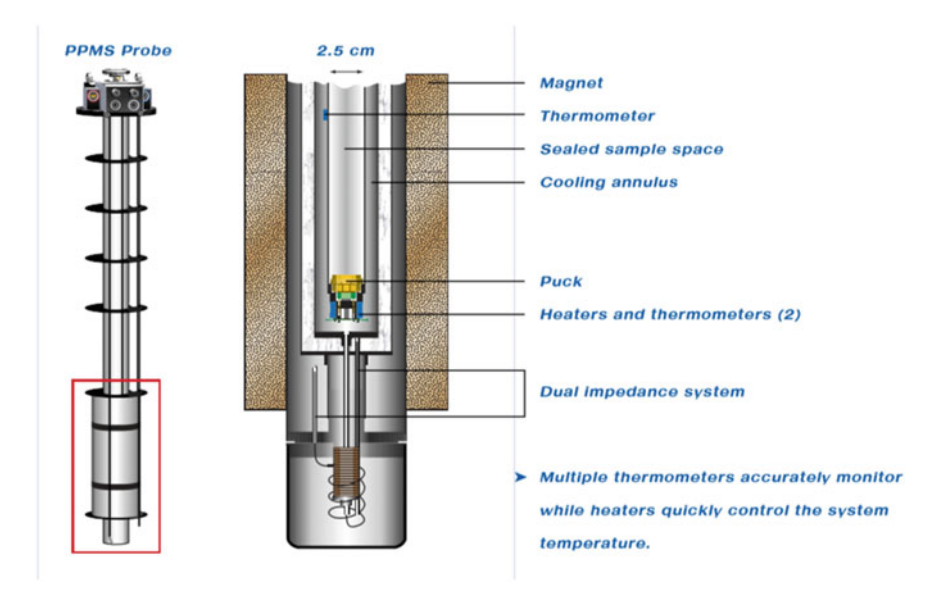


Fig. 3.2 Schematic described the structure of the physical property measurement system

and variable temperature-field conditions. The applied magnetic field can be varied from -9 to 9 T. The temperature range is between 1. 9 and 400 K. Figure 3.2 shows the sample mount space, magnet, cooling annulus and heaters in the PPMS probe. To control the temperature, helium is drawn at the annular region by a vacuum pump and then the heaters warm up the gas, increasing system flexibility by making the sample chamber in a tunable environment.

3.3 Optical Measurement Systems

The optical measurement system which consists of an optical microscope, a spectrometer (Horiba iHR550), and the cryostat (Janis Research Company, ST-500) system is shown in Fig. 3.3. The cryostat condition is in the pressure of 2.0×10^{-7} Torr and can be cooling down to 4.2 K by liquid He or 80 K by liquid N₂ through the cooling gas channel. In the photoresponse measurements, solid-state CW laser (Nd: YAG, 532 nm) is employed as the light source corresponding to the energy gap of MoS₂. The incident light with 1 mW power is guided into the microscope and focused by an objective $(10\times, NA~0.3)$ with a spot size of $\simeq 1~\mu m$. The power density on the sample is estimated at $5.6 \times 10^4~W/cm^2$.

Raman spectroscopy is widely used to study the vibrational, rotational, and other low-frequency modes of particle properties in a lattice system [9]. By inelastic scattering of emission photons in solid or in molecules, the phononic properties of the

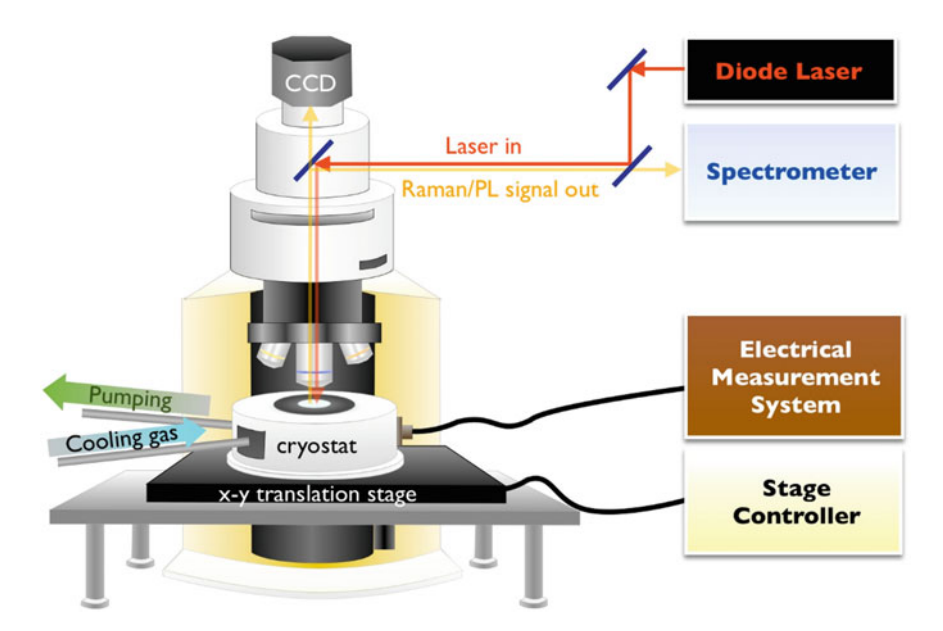


Fig. 3.3 Schematic described the optical measurement system which consists of cryostat, OM, and Raman spectroscopy

crystal or the vibrational properties of molecule can be investigated. If the scattering is elastic, the final state is the same with the initial one, which is called as Rayleighscattering [10]. In contrast, in the case of inelastic scattering, if the final vibrational state is higher (lower) than the initial state in energy, the photon will lost (gain) a portion of energy to obey the law of energy conservation. As depicted in Fig. 3.4, the process is called as Stokes (anti-Stokes) Raman scattering. In addition, the energy shift of Raman modes is strongly related to the electronic system as well as crystal symmetry. Therefore, Raman scattering have been shown as an accurate and noninvasive method to distinguish the number of layers of 2D material. For instance, the monolayer MoS₂ sheet is characterized by optical contrast and the Raman spectroscopy. Figure 3.5a shows an optical microscope image of the MoS₂ flakes on the OTS substrates. To confirm the thickness of MoS₂ sheets, we perform Raman spectroscopy and observe two characteristic peaks at 387 and 405 cm⁻¹ which corresponding to the E2g and A1g resonance modes, respectively [11]. As shown in Fig. 3.5b, the difference of two peaks is about 18 cm⁻¹, which is consistent with previous report on monolayer MoS_2 [12].

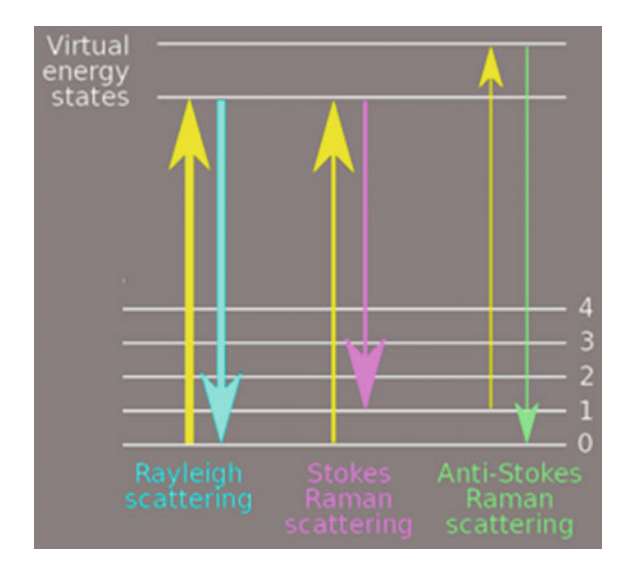


Fig. 3.4 Diagram described the different energy transitions between energy levels for the explanation of the different types of scattering

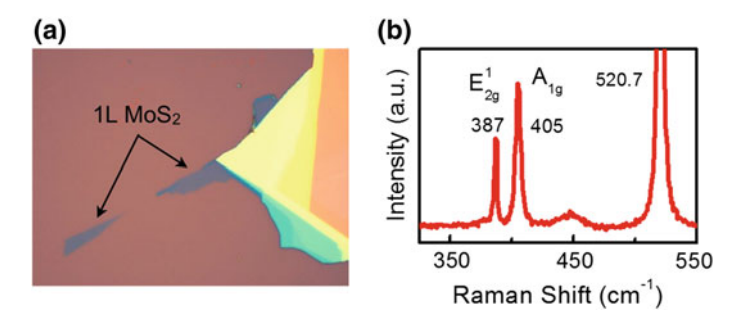
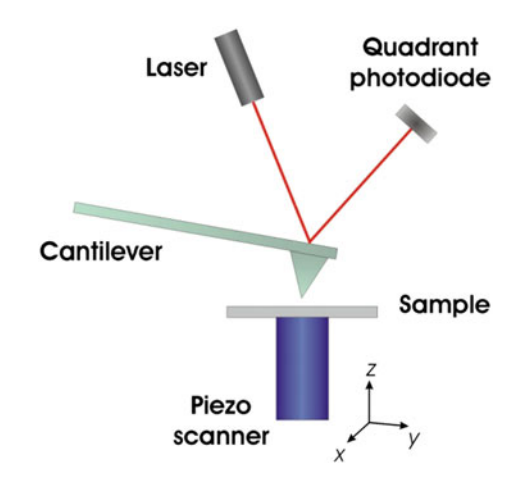


Fig. 3.5 a The OM image of MoS_2 flakes on an OTS substrate. b Raman spectrum of monolayer MoS_2 . The characteristic peaks are measured at 387 and 405 cm⁻¹, which correspond to the E_{2g} and A_{1g} resonance modes, respectively

3.4 Atomic Force Microscopy

The atomic force microscopy (AFM) can precisely measure the thickness of the material down to one atomic layer. Its working mechanism is shown in Fig. 3.6. The information between the tip and sample surface is monitored by the optical reflection at the cantilever and subsequently detected by a photo-detector. The contact mode and tapping mode are used to operate in the experiments, which are distinguished by the shape of the potential between tip and sample. In the contact mode, the measurement is related to the variation of the repulsive forces due to Pauli repulsion. The forces between the tip and the surface is recorded and kept in the feedback

Fig. 3.6 Diagram described working mechanism of AFM. Diagram taken from Ref. [13]



loop. In comparison, the tapping mode exploits the attractive minimum potential between the tip and sample, leading to a periodic tapping motion. During scanning, the interaction between tip and sample provokes a change in the amplitude, resonance frequency, and phase of the cantilever, which are used for feedback control.

3.5 OTS-Functionalized Substrates and Electrical Measurement Method

3.5.1 OTS-Functionalized Substrates

The OTS-functionalized SiO₂/Si substrates can effectively reduce charged impurity scattering due to adsorbed molecules and the phonon effect, which is coupled to the substrates. Consequently, graphene on OTS-functionalized SiO₂/Si substrates exhibits high mobility [3]. The surface topography images revealed by AFM show that the surface roughness are estimated to be approximately 0.3 – 0.4 nm for SiO₂/Si substrates and 0.15 – 0.2 nm for OTS-modified substrates in Fig. 3.7a and b, respectively. It shows an ultra-smooth substrate modified by OTS thin film. In addition, the Fig. 3.7e shows the histogram of surface roughness, which also reveals that the FWHM is 0.3 nm for the ultra-smooth OTS-modified substrate, which is lower than 0.5 nm for the SiO₂/Si substrate. Moreover, we preform the contact angle measurements on SiO₂/Si and OTS-modified substrates, respectively shown in Fig. 3.7c and d. The contact angle of the OTS-modified substrate is 109°, exhibiting ahydrophobic property of OTS modified substrates. By this property, it not only effectively decreasess the number of dangling bonds and extrinsic surface-adsorbed molecules, but also reduces doping or charged impurity scattering on the device.

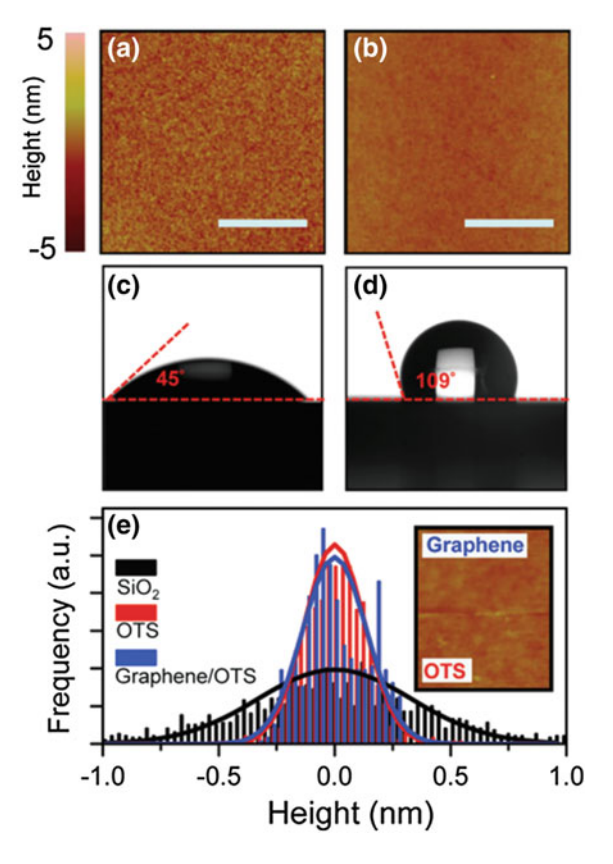


Fig. 3.7 The comparison of surface characterizations of SiO_2/Si and OTS-modified substrates by AFM and contact angle measurements. The difference in surface topography is shown by the AFM images of **a** typical SiO_2/Si and **b** typical OTS-modified substrates. The scale bar is 1 μ m. The measured contact angles of **c** typical SiO_2 and **d** typical OTS-modified substrates are 45 and 109° , respectively. The contact angle measurement reveals the highly hydrophobic surface property of the OTS-modified substrate. **e** Histogram of the height distribution for the SiO_2/Si substrate (black), the OTS-modified substrate (red), and graphene on the OTS-modified substrate (blue). The histogram is calculated from the AFM images, and the solid lines are fitted by a Gaussian distribution. The FWHM of the height distribution are 0.5 and 0.3 nm for the SiO_2/Si and OTS modified substrates, respectively. It is noted that the FWHM of graphene on the OTS-modified substrate is very close to that of the OTS-modified substrate [3]

3.5.2 Two-Terminal Conductance Measurements

Figure 3.8 shows the schematic of two-terminal measurement system. We measure the transport properties of device by standard lock-in techniques. We apply an ac source-drain bias and measure the current by a current pre-amplifier (Stanford Research Systems, SR570) and then measured by a lock-in amplifier (Stanford

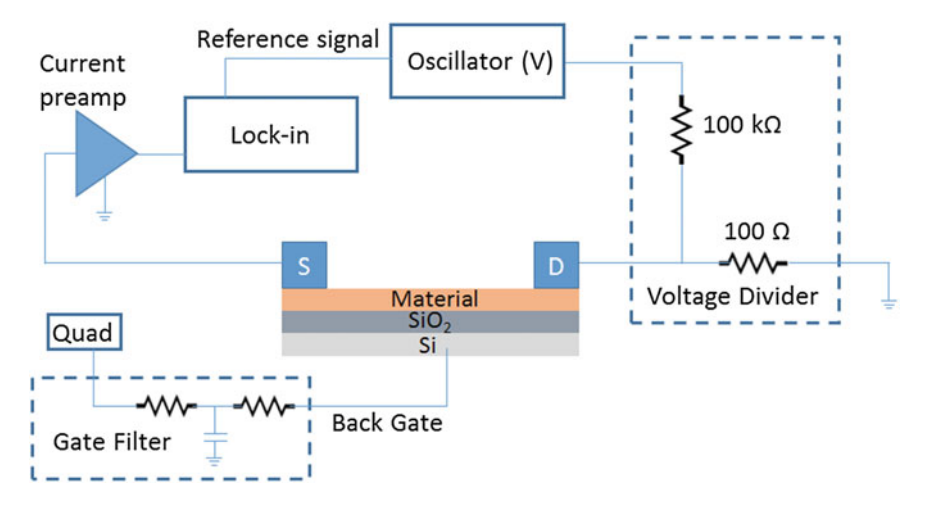


Fig. 3.8 Diagram described the two-terminal conductance measurement

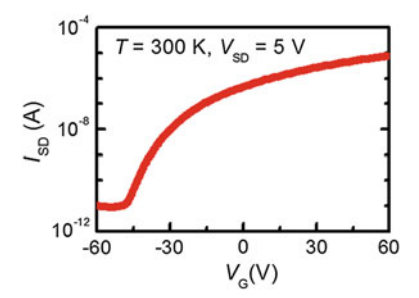


Fig. 3.9 $I_{SD-}V_G$ curve of a monolayer MoS $_2$ device. The on/off ratio is about 10^6 at room temperature

Research Systems, SR830). Back gate voltage is applied by a DC sourcemeter (Keithley 2400).

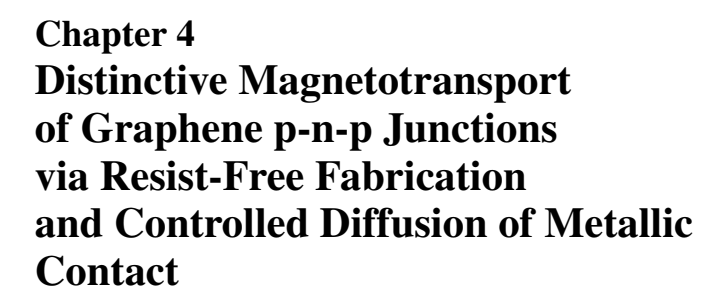
To measure the low off-current in MoS_2 , we employ the DC measurement. DC source and back gate voltage are applied by DC sourcemeter Keithley 237 and 2400, respectively. The transfer characteristic of the monolayer MoS_2 device is shown in Fig. 3.9, which exhibits a typical n-type semiconductor behavior with off current $\sim 10^{-11}$ A. The on/off ratio is observed about 10^6 ($V_G = \pm 60$ V) at room temperature.

References

- 1. A.M.M. Pruisken, Phys. Rev. Lett. 61, 1297 (1988)
- W. Bao, G. Liu, Z. Zhao, H. Zhang, D. Yan, A. Deshpande, B. LeRoy, C. Lau, Nano Res. 3, 98 (2010)

References 31

- 3. S.-Y. Chen, P.-H. Ho, R.-J. Shiue, C.-W. Chen, W.-H. Wang, Nano Lett. 12, 964 (2012)
- F.-Y. Shih, S.-Y. Chen, C.-H. Liu, P.-H. Ho, T.-S. Wu, C.-W. Chen, Y.-F. Chen, W.-H. Wang, AIP Adv. 4, 067129 (2014)
- O. Vazquez-Mena, L. Gross, S. Xie, L.G. Villanueva, J. Brugger, Microelectron Eng. 132, 236 (2015)
- M. Jang, T.Q. Trung, J.-H. Jung, B.-Y. Kim, N.-E. Lee, Phys. Chem. Chem. Phys. 16, 4098 (2014)
- 7. K. Yoon, G. Hwang, J. Chung, H.G. Kim, O. Kwon, K.D. Kihm, J.S. Lee, Carbon 76, 77 (2014)
- 8. S. Kim, M. Russell, M. Henry, S.S. Kim, R.R. Naik, A.A. Voevodin, S.S. Jang, V.V. Tsukruk, A.G. Fedorov, Nanoscale 7, 14946 (2015)
- 9. D.J. Gardiner, P.R. Graves, *Practical Raman Spectroscopy*. Springer-Verlag (1989)
- 10. A.T. Young, Appl. Opt. 20, 533 (1981)
- 11. P.A. Bertrand, Phys. Rev. B **44**, 5745 (1991)
- 12. H. Li, Q. Zhang, C.C.R. Yap, B.K. Tay, T.H.T. Edwin, A. Olivier, D. Baillargeat, Adv. Funct. Mater. 22, 1385 (2012)
- 13. M. Baclayon, G.J.L. Wuite, W.H. Roos, Soft Matt. 6, 5273 (2010)





4.1 Introduction

Graphene junction devices have revealed unique electrical transport properties [1], including quantum interference [2, 3], Klein tunneling [4, 5], and the fractional-valued quantum Hall effect [6], which are absent in homogeneous graphene. The versatility of the graphene junction devices can therefore offer novel functionality of the graphene-based material. To fabricate these graphene junction devices, various methods, including dual-gated technique [6–8], chemical doping of the graphene surface [9–12], and electronic modification of the substrates [13], have been reported.

To explore the novel functionality of the graphene junction devices, the ability to fabricate high-quality devices is essential. To achieve this, most studies have used dual-gated structures [6–8] to create differential doping in different regions of graphene. Interface engineering has also been demonstrated by utilizing non-covalent functionalization [9] in creation of graphene junction devices. Generally, multi-step fabrication involving e-beam lithography or surface functionalization is required in the fabrication of the graphene devices. However, a simple fabrication which requires no lithographic process to achieve high-quality graphene junction devices is highly desirable. Here we demonstrate fabrication of graphene p-n-p junction and p-n junction by a resist-free fabrication process. This method involves one-step deposition to fabricate contacts by well-controlled diffusion of metals. Moreover, we adapt a resist-free approach to reduce undesirable residue which can cause substantial carrier scattering. Notably, the fabricated graphene junction devices exhibit noticeable magnetotransport properties, including pronounced quantum Hall effect and weak localization well-described by the theory.

4.2 Fabrication

The fabrication processes are depicted in schematics of Fig. 4.1a, b. We first fabricate the shadow mask which was described in Chap. 3. We then align graphene flakes with respect to the shadow mask by utilizing a homemade x-y-z manipulator under an optical microscope (OM), as shown in Fig. 4.1b. A key step is to control the distance between the graphene sample and the mask, which is enabled by inserting proper thickness of a gasket (Kapton tapes, ~15–20 μ m/layer) under the shadow mask. Figure 4.1c, d show the OM images of a graphene sample with a gap distance of 18 and 130 μ m, respectively. Although the grid is out of focus for large gap distance, it is still manageable to align with the graphene flake, as shown in Fig. 4.1d. After the alignment, Ti/Au (5 nm/55 nm) was deposited as electrodes at a base pressure of 1.0×10^{-7} Torr.

4.3 Experimental Results

Figure 4.1e shows an OM image of a fabricated graphene sample, which exhibits a large diffusion region (gradient colored region) resulted from intentionally increased gap distance. These diffusion regions are easily oxidized and cause p-type doping effect in graphene underneath, leading to a graphene p-n-p structure [14]. Figure 4.1f shows a schematic of the graphene p-n-p junction with a pronounced diffusion of the metallic contact. A line profile of topography obtained from the AFM mapping (Fig. 4.1g) yields a diffused extent of $4\,\mu m$ as a result of $130\,\mu m$ gap. We fabricate 25 test samples with the gap distance ranging from 80 to 180 μm , and plotte the diffusion length obtained from the AFM characterization as a function of gap distance in Fig. 4.1h. The relatively linear correlation indicates the viability to vary the diffusion by adjusting the gap distance.

We first present the magnetotransport properties of the fabricated graphene p-n-p junctions prepared by the aforementioned resist-free technique. Figure 4.2a shows the magnetic field dependence of conductance (G-B) of the sample A at $V_G=0$ V and 10 V, corresponding to the unipolar and bipolar regime, respectively. At high magnetic fields, the magnetoconductance (MC) evolves into pronounced quantum Hall (QH) plateaus, which suggests the high mobility of the graphene p-n-p junction sample. The observed filling factors are consistent with those in graphene p-n-p junction: the $2\ e^2/h$ plateau for B>3 T at $V_G=0$ V is consistent with

$$G = min(|v_1|, |v_2|) \times e^2/h$$
 (4.1)

in the unipolar regime [15]. In the bipolar regime ($V_G = 10 \text{ V}$), the QH plateaus can be expressed as

$$G = v_{\rm pnp} e^2 / h, \tag{4.2}$$

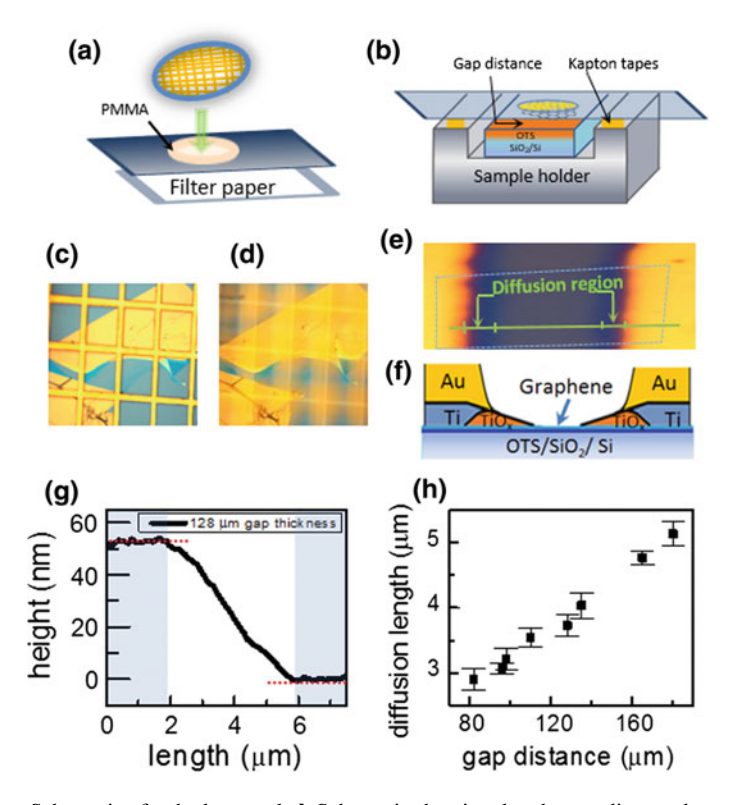


Fig. 4.1 a Schematic of a shadow mask. b Schematic showing that the gap distance between mask and graphene is controlled by inserting Kapton tapes. c, d OM images in which the gap distances are 18 and 130 $\,\mu$ m, respectively. e The OM image of a p-n-p junction device. The blue area shows the diffusion area after deposition. The location of graphene is presented by the dash line. f Schematic of the device structure. g An example for the demonstration of the metallic diffusion length. The diffusion length is identified between the metal and graphene platform edge in AFM data. h The linear correlation in the curve of diffusion length as a function of gap distance

with $v_{pnp} = |v_1||v_2|/(|v_1| + 2|v_2|)$ ($v_1v_2 < 0$, v_1 , $v_2 = \pm 2$, ± 6 , ...) [6]. The filling factor $v_1 = 2/3$ for $v_2 = 2/3$ for $v_3 = 1/2$ state of the intrinsic graphene region and $v_2 = -2$ state of the doped region [14].

At low magnetic fields, sample A exhibits positive MC (Fig. 4.2b), which can be attributed to the weak localization (WL) in graphene. The WL is manifested by the suppression of the conductivity, which is owing to the coherent backscattering of carrier wave scattered by weak disordered potential. The WL is suppressed due to the chiral nature of carriers in graphene system [16–18]. The inset in Fig. 4.2c shows the $\sigma-B$ curves of sample A in the unipolar ($V_G=0$ V) and bipolar regimes ($V_G=10, 20$ V). The $\sigma-B$ curves were analyzed by the WL theory developed for graphene [17, 19], in which the quantum correction to the semi-classical (Drude) conductivity, $\delta\sigma(B)$, is given by

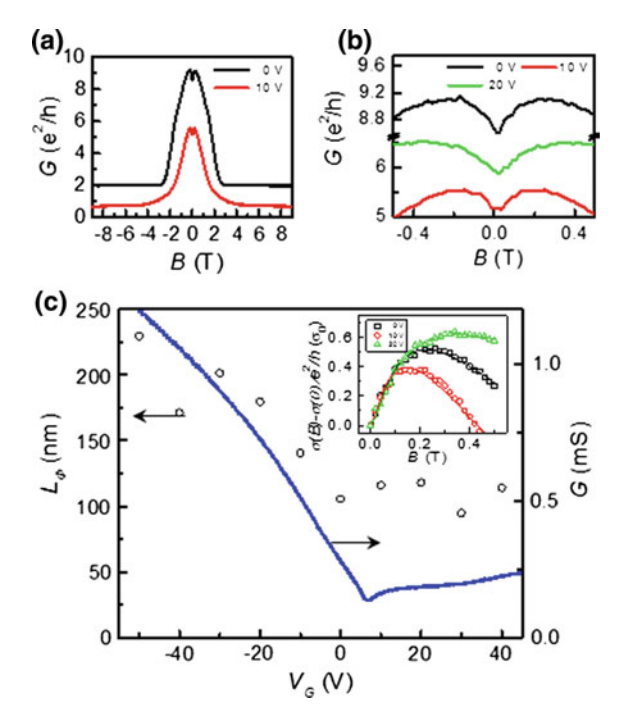


Fig. 4.2 a The magnetoconductance of the p-n-p device in the range of 9 T>B>-9 T. **b** The weak localization effect for back gate voltages of 0, 10, and 20 V. **c** The G and coherent length as a function of back gate voltage. Inset shows that the data can be well fitted by Eq. 4.4

$$\Delta\sigma(B) = \frac{e^2}{\pi h} \left[F\left(\frac{\tau_B^{-1}}{\tau_{\Phi}^{-1}}\right) - F\left(\frac{\tau_B^{-1}}{\tau_{\Phi}^{-1} + 2\tau_i^{-1}}\right) - 2F\left(\frac{\tau_B^{-1}}{\tau_{\Phi}^{-1} + \tau_i^{-1} + \tau_i^{-1}}\right) \right], \quad (4.4)$$

$$F(z) = \ln z + \psi \left(\frac{1}{2} + \frac{1}{z}\right),$$
 (4.5)

$$\tau_B^{-1} = 4eDB/\hbar,\tag{4.6}$$

$$\tau_{\Phi,i,*} = L_{\Phi,i,*}^2/D,$$
(4.7)

where $\psi(z)$, τ_{Φ} , τ_{i} , and τ_{*} are corresponding to the digamma function, phase coherence time, intervalley scattering time, and intravalley scattering time, respectively. The MC data for $V_{G}=0$, 10, 20 V are well described by the theory, as shown in the inset of Fig. 4.2c, validating WL as the mechanism for the observed positive MC. Moreover, the MC data are well fitted for $-50\mathrm{V} < V_{G} < 40\mathrm{V}$, yielding a V_{G} -dependent L_{ϕ} in the range of 95–230 nm, as shown in Fig. 4.2c. Notably, we observe that the trend resembles to $G-V_{G}$ curve, in which L_{ϕ} and G are gate-independent in the bipolar regime and correlated in the unipolar regime. To understand this correlation, we point out that L_{ϕ} can be expressed as

$$L_{\Phi} = \sqrt{D\tau_{\Phi}} = \sqrt{\nu_F^2 \tau_0 \tau_{\Phi}},\tag{4.8}$$

where D, v_F , and τ_0 , are diffusion coefficient, Fermi velocity, and momentum relaxation time, respectively [17]. τ_0 is strongly dependent on carrier density, which is attributed to less momentum scattering away from the electron-hole puddle near Dirac point [20–22]. Because L_ϕ is proportional to the square root of τ_0 , it is reasonable that L_ϕ and G are correlated, despite that WL originated from an interference effect which is quantum mechanical in nature.

We further compare the T dependence of resistance (R) between unipolar and bipolar regimes to elucidate the transport characteristics discussed in Fig. 4.2c. Figure 4.3a, b show the T dependence of R in the unipolar and bipolar regimes, respectively. At T < 100 K, the graphene p-n-p junction exhibits insulating behavior (dR/dT > 0) in both unipolar and bipolar regimes. The performance of carrier transport in the channel is closely related to the temperature, uncovering the dominant mechanism in the system. The T dependence of R can be well described by a power law $R \propto T^{\gamma}$ and V_G -dependence exponent γ is plotted in Fig. 4.3c. It is noted that γ is relatively independent on the variations of V_G in the bipolar regime $(\gamma \sim -0.12)$, which is similar in the $L_{\phi} - V_{G}$ and $G - V_{G}$ curves shown in Fig. 4.2c. Considering the presence of charged impurity, an insulating behavior of graphene at low T has been reported and is attributed to the activated transport in the presence of electron-hole puddles [23]. We therefore infer that the carrier transport in the bipolar regime is dominated by the electron-hole puddles, which may originate from the doped graphene region where charged impurity in the oxide layer cause large potential fluctuation [24]. As V_G is tuned away from the CNP, the value of γ reduces and the graphene device becomes less insulating as a result of suppression of the carrier localization due to the electron-hole puddles.

At T > 100 K, sample A exhibits an opposite T dependence between the unipolar and bipolar regimes. In the unipolar regime, the graphene p-n-p junction exhibits a metal-insulator transition as in homogeneous graphene and can be attributed to the phonon effect and thermal weakening of screening at higher T [23]. Interestingly, the insulating behavior in the bipolar regime persists up to room temperature, suggesting the dominance of activated insulating behavior over the phonon effect. The observed insulating behavior in the bipolar regime may be attributed to the proximity of Fermi level to the CNP and the scattering at the p-n interface, which both lead to the localization of the carriers.

We further analyze the T dependence of MC to reveal the carrier transport mechanism in the graphene p-n-p junction samples. Figure 4.3d shows the $\sigma-B$ curves of sample A at $V_G=0$ V with T ranging from 2 to 80 K. The positive MC signal is suppressed as T increases, which is attributed to the reduction of phase coherence length [18]. The T dependent $\sigma-B$ curves can be well described by the WL theory, yielding a T dependence of L_ϕ , as shown in Fig. 4.3e. It is found that L_ϕ decreases from 100 to 32 nm as T increases in the range of 2 < T < 80 K. At T > 15 K, L_ϕ exhibits a T dependence of $\sim T^{-0.5}$, which can be ascribed to the electron-electron scattering with expressed as

$$\tau_{\Phi}^{-1} = \beta k_B T \ln g / \hbar g, \tag{4.9}$$

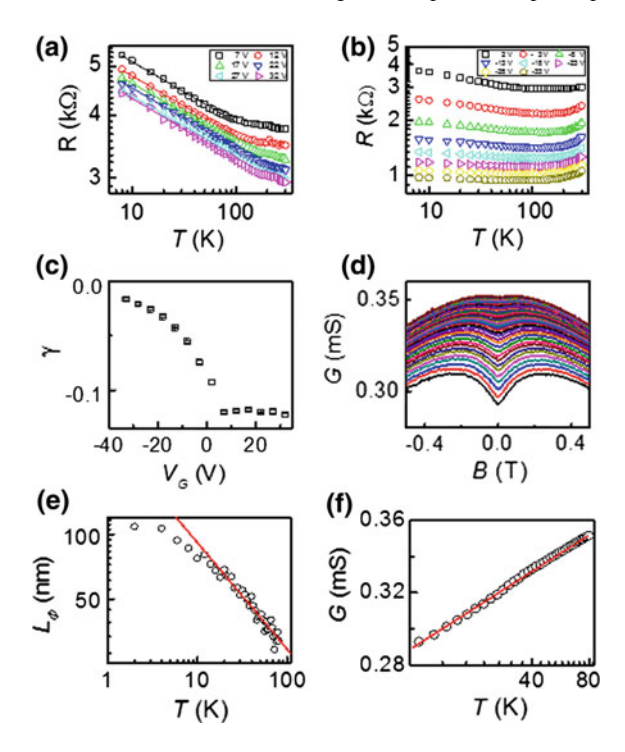


Fig. 4.3 a Resistance as a function of temperature dependence in the bipolar regime. b The metalinsulator transition in the unipolar regime. c The detail of the temperature exponent in whole back gate voltage regime, revealing the similar exponent under 100 K in bipolar regime. d The WL for back gate voltage of 0 V. e L_{ϕ} as a function of temperature dependence. L_{ϕ} exhibits a T dependence of $\sim T^{-0.5}$. f A logarithmic T dependence of conductance at zero magnetic field and at zero back gate voltage

where $g = \sigma h/e^2$ [25, 26]. In Fig. 4.3f, it is shown that the conductivity at B = 0 T exhibits a logarithmic T dependence, which is consistent with the weak localization effect [25, 26]. Here we note that the dephasing mechanism of the phase coherent length in the studied graphene p-n-p junction samples is consistent with that of homogeneous graphene samples, suggesting the irrelevance of the p-n interface in this MC measurement.

4.4 Demonstration of p-n Junction Devices

This resist-free method can be applied to fabricate a graphene p-n junction device by combining a diffused and a conventional contact in an asymmetric technique. The resulted sample is characterized by the OM image (inset of Fig. 4.4a), shown an asymmetric profile of the contacts. The contact of the left side exhibits a large diffusion length of 3 μ m while that of the right side shows a negligible diffusion

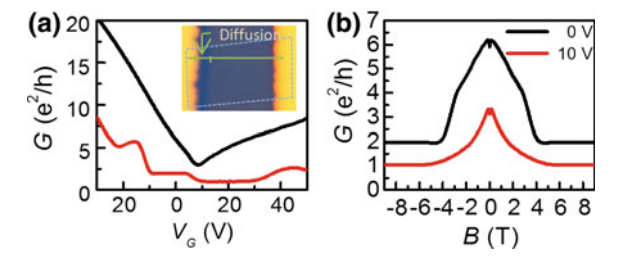


Fig. 4.4 a $G - V_G$ curves at B = 0 (black) T and 9 (red) T. Inset: OM of the p-n junction device. It is employed metal diffusion fabrication on the left side to affect doping effect in the channel. **b** The magnetoconductance of the p-n junction device

length of 0.2 µm. We then present the magnetotransport properties of the fabricated graphene device (sample B) to reveal the effect of asymmetric contact. Figure 4.4a shows the $G - V_G$ curves of sample B at B = 0 T and B = 9 T. The $G - V_G$ curve at B = 0 T shows a dip similar to sample A (Fig. 4.2c), suggesting the presence of a doped graphene region resulted from the diffused contact area [14]. At B = 9 T, we observe pronounced QH plateau with v = 1 in the bipolar region, indicating a full mixing of the edge states of $v_1 = 2$ of the intrinsic graphene region and that of $v_2 = -2$ of the doped region at the interface of the graphene p-n junction [15]. In the unipolar region, sample B exhibits QH plateau with v = 2, showing typical half-integer QH effect in the hole conduction regime. These filling factors are consistent with those of graphene p-n junction samples [7, 27, 28]. Moreover, we compare the G - B curves of sample B at $V_G = 0$ V (unipolar regime) with that at $V_G = 10 \text{ V}$ (bipolar regime). In the unipolar regime, QH plateau of $\nu = 2$ is observed for B > 4 T. In the bipolar regime, sample B exhibits a filling factor v = 1 for B > 15.5 T, which is consistent with the QH plateau observed in a graphene p-n junction. Therefore, the measured magnetotransport behavior indicates the realization of highquality graphene p-n junction device by employing the asymmetric fabrication of the two electrodes and the controlled diffusion of metallic contact.

4.5 Conclusion

We report distinctive magnetotransport properties of graphene p-n-p junctions with a resist-free, one-step method. We have realized controlled lateral diffusion of metallic contact, which enables simultaneous fabrication of electrical contact and interfacial oxidation for doping. By using this simple method, the fabricated graphene p-n-p junction samples exhibit pronounced quantum Hall (QH) effect with a fractional-valued plateau. We observed weak localization in the graphene p-n-p junction sample and the coherence length is found to be correlated to the two-terminal conductance. The temperature dependence of resistance follows a power law and the analysis of the exponent indicates the dominant role of electron-hole puddles in the transport

behavior. We have also utilized asymmetric method to achieve lateral diffusion in one of the two-terminal electrodes, resulting in graphene p-n junction, as evidence of pronounced QH effect.

References

- 1. A.F. Young, P. Kim, Ann. Rev. Conden. Ma. P. 2, 101 (2011)
- 2. A.F. Young, P. Kim, Nat. Phys. 5, 222 (2009)
- 3. M. Satoru, M. Sei, O. Masahiro, I. Kazuyuki, W. Kenji, T. Takashi, M. Tomoki, Jpn. J. Appl. Phys. 52, 110105 (2013)
- 4. M.I. Katsnelson, K.S. Novoselov, A.K. Geim, Nat. Phys. 2, 620 (2006)
- 5. A.V. Shytov, M.S. Rudner, L.S. Levitov, Phys. Rev. Lett. 101, 156804 (2008)
- B. Ozyilmaz, P. Jarillo-Herrero, D. Efetov, D.A. Abanin, L.S. Levitov, P. Kim, Phys. Rev. Lett. 99, 166804 (2007)
- 7. J.R. Williams, L. DiCarlo, C.M. Marcus, Science 317, 638 (2007)
- 8. G. Liu, J. Velasco, W.Z. Bao, C.N. Lau, Appl. Phys. Lett. 92, 203103 (2008)
- 9. H.C. Cheng, R.J. Shiue, C.C. Tsai, W.H. Wang, Y.T. Chen, ACS Nano. 5, 2051 (2011)
- 10. D.B. Farmer, Y.M. Lin, A. Afzali-Ardakani, P. Avouris, Appl. Phys. Lett. 94, 213106 (2009)
- 11. K. Brenner, R. Murali, Appl. Phys. Lett. **96**, 063104 (2010)
- F.M. Koehler, N.A. Luechinger, D. Ziegler, E.K. Athanassiou, R.N. Grass, A. Rossi, C. Hierold, A. Stemmer, W.J. Stark, Angew. Chem. Int. Ed. 48, 224 (2009)
- 13. H.-Y. Chiu, V. Perebeinos, Y.-M. Lin, P. Avouris, Nano. Lett. 10, 4634 (2010)
- C.-H. Liu, P.-H. Wang, T.-P. Woo, F.-Y. Shih, S.-C. Liou, P.-H. Ho, C.-W. Chen, C.-T. Liang, W.-H. Wang, Phys. Rev. B 93, 041421(R) (2016)
- 15. D.A. Abanin, L.S. Levitov, Science **317**, 641 (2007)
- S.V. Morozov, K.S. Novoselov, M.I. Katsnelson, F. Schedin, L.A. Ponomarenko, D. Jiang, A.K. Geim, Phys. Rev. Lett. 97, 016801 (2006)
- E. McCann, K. Kechedzhi, V.I. Fal'ko, H. Suzuura, T. Ando, B.L. Altshuler, Phys. Rev. Lett. 97, 146805 (2006)
- 18. X. Wu, X. Li, Z. Song, C. Berger, W.A. de Heer, Phys. Rev. Lett. 98, 136801 (2007)
- F.V. Tikhonenko, D.W. Horsell, R.V. Gorbachev, A.K. Savchenko, Phys. Rev. Lett. 100, 056802 (2008)
- Y.W. Tan, Y. Zhang, K. Bolotin, Y. Zhao, S. Adam, E.H. Hwang, S. Das Sarma, H.L. Stormer, P. Kim, Phys. Rev. Lett. 99, 246803 (2007)
- 21. Y. Oh, J. Eom, H.C. Koo, S.H. Han, Solid State Commun. 150, 1987 (2010)
- M.Z. Iqbal, K. Özgür, M.W. Iqbal, J. Xiaozhan, H. Chanyong, E. Jonghwa, New. J. Phys. 16, 083020 (2014)
- J. Heo, H.J. Chung, S.-H. Lee, H. Yang, D.H. Seo, J.K. Shin, U.I. Chung, S. Seo, E.H. Hwang,
 S. Das Sarma, Phys. Rev. B 84, 035421 (2011)
- 24. E.H. Hwang, S. Das Sarma, Phys. Rev. B **82**, 081409 (R) (2010)
- F.V. Tikhonenko, D.W. Horsell, R.V. Gorbachev, A.K. Savchenko, Phys. Rev. Lett. 100, 056802 (2008)
- 26. B.L. Altshuler, D. Khmel'nitzkii, A.I. Larkin, P.A. Lee, Phys. Rev. B 22, 5142 (1980)
- 27. H.-C. Cheng, R.-J. Shiue, C.-C. Tsai, W.-H. Wang, Y.-T. Chen, ACS Nano. 5, 2051 (2011)
- 28. T. Lohmann, K. von Klitzing, J.H. Smet, Nano. Lett. 9, 1973 (2009)



Chapter 5 Observation of Quantum Hall Plateau-Plateau Transition and Scaling Behavior of the Zeroth Landau Level in Graphene p-n-p Junction

5.1 Introduction

Electrical transport studies of graphene heterostructures [1] have revealed the quantum Hall effect (QHE) [2], quantum interference behaviors [3, 4], Klein tunneling [5, 6], and the split closed-loop resonator [7], hence convincingly demonstrating the advantages of constructing in-plane heterostructures of graphene. Specifically, the relativistic quantization of graphene's electronic spectrum results in distinct characteristics, including the presence of a Landau level (LL) at zero energy and chiral QHE [8–12]. In the quantum Hall (QH) regime, the plateau-plateau transition and the scaling behavior have been studied using Hall bar [13] and Corbino geometry [14], providing important information about the carrier localization in graphene. In a graphene Hall bar, the slope of the Hall conductivity at the transition region, $d\sigma_{xy}/dv$, exhibits scaling behavior with $\kappa = 0.41$ for the first and second LLs, while that of the zeroth LL is temperature (T)-independent [13]. In a Corbino geometry, the full width at half maxima (FWHM) Δv of the zeroth LL is T dependent and shows scaling behavior with $\kappa = 0.16$, which is attributed to an inhomogeneous charge carrier distribution [14]. However, until now, a well-defined QH plateau-plateau transition point of the zeroth LL of graphene has not been directly observed, obscuring a detailed understanding of the scaling behavior of this unique LL. Moreover, the variation of the T exponent in previous reports suggests the need for further investigation of the scaling behavior of the zeroth LL using different methods for the device structures.

In this chapter, we fabricate a high-quality graphene p-n-p junction, achieved via controlled diffusion of metallic contacts, to explore the QH plateau-plateau transition and scaling behavior of graphene. Interestingly, we observe a well-defined transition point corresponding to the zeroth LL, revealing the scaling behavior and a reduced T exponent. There are additional advantages of utilizing a graphene p-n-p junction to explore the transition region of the QHE. First, the presence of the transition between an integer QH plateau and a QH plateau with a fractional value enables direct access to the transition of the zeroth LL. Second, in a graphene p-n-p geometry, the intrinsic

graphene region is adjoined by the doped graphene from both sides. The doped graphene regions can be viewed as an ideal contact, facilitating the investigation of the transition region of the intrinsic graphene. Moreover, we derive the value of energy level for the observed LLs, which agrees with the theoretical values, further validating the assignment of the LL index of the QH plateau-plateau transition.

5.2 Fabrication

We exfoliated monolayer graphene onto SiO₂/Si substrates modified by a selfassembled monolayer of organic molecules (octadecyltrichlorosilane) [15], which can greatly reduce charged-impurity scattering and provide an ultra-smooth substrate surface [15]. We then employed resist-free fabrication with a shadow mask to reduce possible polymer residue. A crucial step in this process was to control the metal diffusion of electrodes by deliberately increasing the gap between the shadow mask and graphene samples. We then deposited Ti/Au (5 nm/50 nm) onto the graphene sample as contact electrodes, and the extent of the edge diffusion of the electrodes was fine controlled by a proper distance between the shadow mask and the graphene samples, which is demonsated in Chap. 4. The graphene p-n-p devices were annealed at 110 °C for 3 h in a low vacuum (helium atmosphere) to remove the adsorbates on the surface of graphene, then cooled down to $T = 2 \,\mathrm{K}$. We measured the devices by using a standard lock-in technique, with 100 μV of source-drain voltage and a modulation frequency of 17 Hz. The current signal was amplified by using a current pre-amplifier (Stanford Research Systems, SR570) and then measured by using a lock-in amplifier (Stanford Research Systems, SR830). V_G was applied by using a DC source (Keithley 2400).

Figure 5.1a shows a schematic of the graphene p-n-p junction device with a pronounced diffusion of the metallic contact. With a gap of $(130\pm5)\,\mu\text{m}$, we deposited 5-nm-thick Ti and 50-nm-thick Au as contact electrodes, which resulted in a large lateral diffusion of approximately 4 μ m, as evidenced by an AFM image of sample A (Fig. 5.1b, blue gradient area). Before we performed transport/magnetotransport measurement, the samples had been annealed at 383 K for 3 h in a low vacuum (helium atmosphere) to remove adsorbates [15].

5.3 Experimental Results

5.3.1 The Doping Effect from Titanium Diffusion

We note that the Ti layer play a critical role in determining the transport behavior by comparing the two-terminal conductance vs. gate voltage $(G - V_G)$ curves of a graphene p-n-p junction (sample A) and a control sample (sample B), as shown in

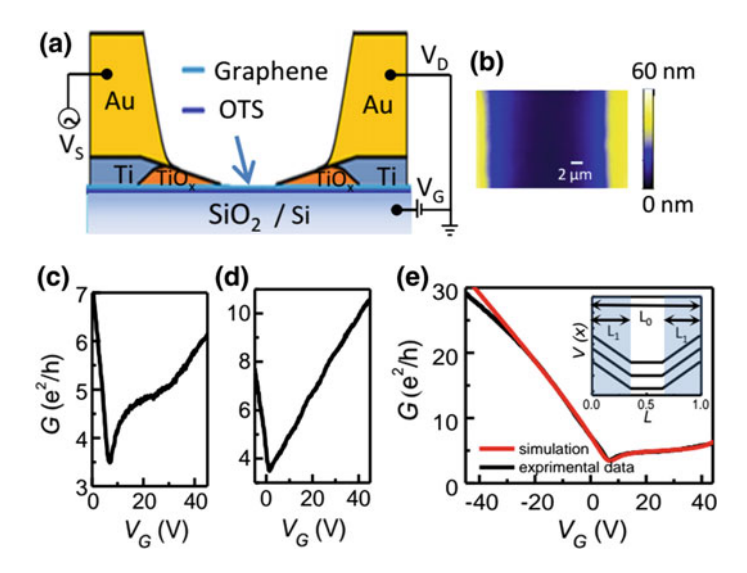


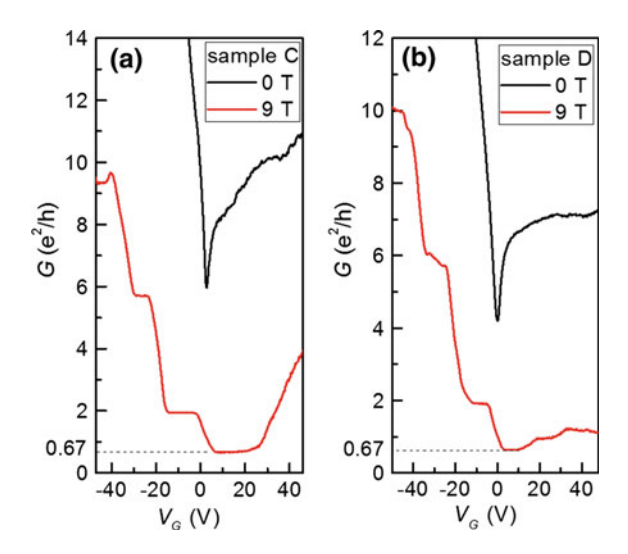
Fig. 5.1 The structure and the transport characteristics of the graphene p-n-p junctions. **a** A schematic of the structure of the graphene device with diffused electrode edges. **b** An AFM image showing the edge diffusion of sample A. Comparison of the $G - V_G$ curves between **c** sample A and **d** sample B with Au electrode. **e** Measured $G - V_G$ curve for sample A at T = 2 K and simulation based on the metal contact model. Inset: depinning potential assumed in the simulation

Fig. 5.1c, d, respectively. For sample A, a large field effect is observed for $V_G < 7$ V, showing a typical graphene characteristic, in which the $G - V_G$ curve can be well described by the self-consistent Boltzmann equation

$$\rho = (ne\mu_c + \sigma_0)^{-1} + \rho_s, \tag{5.1}$$

where μ_c , ρ_s , and σ_0 are density-independent mobility, the resistivity due to short-range scattering, and residual conductance at the Dirac point, respectively. The fit yields that μ_c and ρ_s of sample A are 3000 cm²/V s and 368 Ω , respectively. However, the $G-V_G$ curve for $V_G>7$ V shows an additional conductance minimum at $V_G=32$ V, suggesting a doping effect of graphene in the diffused electrode region [16, 17]. The double conductance minimum was reproducible in graphene p-n-p junction devices, sample C and sample D, as shown in Fig. 5.2a, b. To examine the role of the Ti layer, we have fabricated sample B such that the contact metal is made only with Au instead of the Ti/Au bilayer. Different from sample A, sample B exhibits a typical $G-V_G$ curve in the regime $V_G>V_{CNP}$, as shown in Fig. 5.1d. We therefore infer that the double dip feature observed in sample A is related to the Ti adhesion layer.

Fig. 5.2 a, b The transport and magnetotransport for samples C and D. Both samples exhibit QH plateaus of $\nu = 2$, 6 in the unipolar regime and $\nu = 2/3$ in the bipolar regime



5.3.2 The Doping Effect Simulated by Theoretical Dipining Model

It is well understood that the charge density of graphene under metallic contact is pinned due to Fermi level pinning [18, 19], leading to typical transfer characteristics. We confirm the structure of a diffused electrode via theoretical simulation based on a simple metal contact model [20]. The overall channel resistance, R, can be written as follows:

$$R = \frac{1}{W} \int_{0}^{L_0} \frac{1}{\sigma(x)} dx,$$
 (5.2)

where L_0 , W and $\sigma(x)$ are the channel length, sample width and local conductivity, respectively. The ratio $L_0/W=1.06$ is extracted from the sample geometry. The local conductivity can be formulated as

$$\sigma(x) = \sqrt{\{\mu_C C_0 [V_G - V_D(x)]\}^2 + \sigma_{min}^2},$$
(5.3)

where C_0 is the gate capacitance per unit area and μ is the carrier mobility. Nevertheless, an additional kink is observed in the $G-V_G$ curve, suggesting that the depinning of charge density occurs [20, 21]. We performed a theoretical simulation of the $G-V_G$ curves based on a simple metal contact model [21], in which the overall channel resistance. Therefore, R can be re-written as

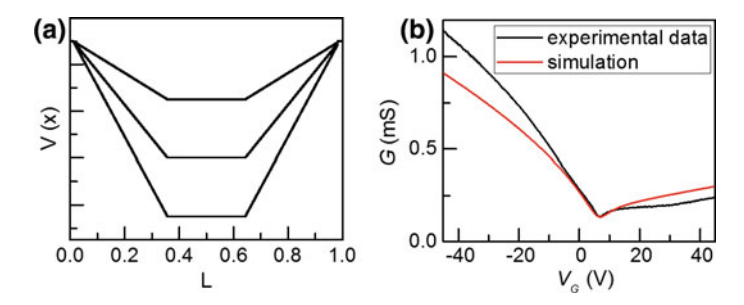


Fig. 5.3 a The potential profile, assuming charge-density pinning. b $G - V_G$ curve and simulation, assuming the pinning potential with the same parameter $L_1 = 0.33L_0$

$$R = \frac{1}{W} \int_{0}^{L_0} (\{\mu C_0 [V_G - V_D(x)]\}^2 + \sigma_{min}^2)^{-1/2} dx.$$
 (5.4)

By assuming charge-density depinning and employing the potential profile V(x) depicted in the inset of Fig. 5.1e, we calculated transfer characteristics that reasonably fit the measured data, as shown in Fig. 5.1e. Conversely, if the potential is pinned, the simulation yields a $G-V_G$ curve with a single conductance minimum, which is not consistent with the experimental curves, as shown in Fig. 5.2. The agreement between the modeled and the measured $G-V_G$ curve suggests that the interfacial metal is oxidized [20]. In the calculation, we applied the device geometry with $L_0/W=1.06$ and assumed $L_1=0.35L_0$ ($L_0=12$ μ m). We note that the resulting $L_1=4.2$ μ m is comparable to the diffusion length of 4 μ m obtained from the AFM images (Fig. 5.1b), indicating that the interfacial oxidation occurs approximately in the diffused area. The depinning enables large-area modification of the carrier density [20, 21], which causes a doped graphene region [22]. We therefore conclude that charge-density depinning and the doping effect occur in the diffusion region, leading to a graphene p-n-p structure (Fig. 5.3).

5.3.3 Characteristics of Graphene p-n-p Junction Devices

We demonstrated the characteristics of three graphene p-n-p devices, including sample A, sample B, and sample C. The extent of the electrode diffusion of samples C and D is comparable to that of sample A. The charged neutrality points (CNP) of samples A, C, and D correspond to 7, 2, and 0 V, respectively. The CNP is observed in the vicinity of zero V_G , which is attributed to the low density of charged impurities on the OTS-modified substrates. The field effect mobility in the unipolar regions of samples A, C, and D are 3000, 5308, and 3774 cm²/V s, respectively. It is expected

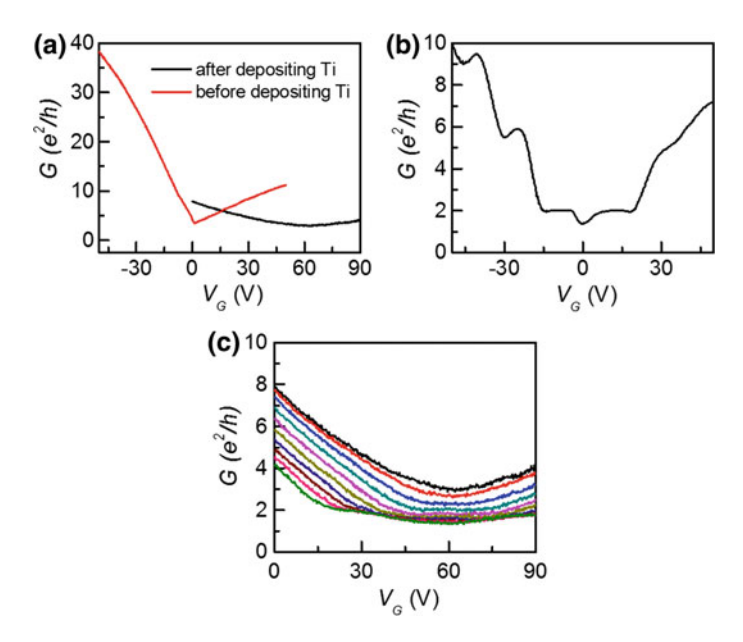


Fig. 5.4 a $G-V_G$ curves before (red curve) and after (black curve) deposition of Ti onto the graphene channel. b The control sample before Ti deposition exhibiting QH plateaus of $\nu = 2$, 6 for both electron and hole branches at B = 9 T. c The control sample after Ti deposition showing the QH plateau of $\nu = 2$ as the magnetic field increases from B = 0 T to B = 9 T

that the graphene samples attain to the quantum Hall (QH) regime at B = 9 T, based on the condition $\mu B > 1$ [23].

To understand the critical role played by the Ti layer, we fabricate a control sample with an Au electrode and then deposite Ti (1 nm) onto the graphene channel by using a polymethyl methacrylate (PMMA) stencil mask [24]. Figure 5.4a compares the $G-V_G$ curve of a control sample before Ti deposition with that after Ti deposition. The CNP is greatly shifted toward the positive voltage of ~64 V, indicatingstrong p-type doping. This p-type doping is consistent with the formation of the graphene p-n-p junctions through controlled diffusion as well as with oxidation that causes the charge-density depinning discussed in the main text.

Figure 5.4a shows that the carrier mobility is suppressed for both the electron and hole branches after Ti deposition, which can be attributed to the increased charged impurity scattering. Figure 5.4b shows the $G-V_G$ curves of the control sample before Ti deposition at $B=9\,\mathrm{T}$, where the conventional integer QH effect is observed. After Ti deposition, the mobility dropped to ~1000 cm²/V s. Nevertheless, we can still observe QH-related characteristics in the control sample with this Ti deposition because the QH plateau of v=2 is observable at $B=9\,\mathrm{T}$, as shown in Fig. 5.4c, suggesting that a graphene p-n-p junction is feasible with titanium oxide as a doping source.

5.3.4 Quantum Hall Effect in p-n-p Junction

We present the magnetotransport properties of the fabricated graphene p-n-p junctions. Figure 5.5a compares the $G - V_G$ curves of sample A at B = 0 T and B = 9 T. The graphene sample exhibits two conductance minima at B = 0 T, corresponding to the pristine and doped graphene regions mentioned above. Therefore, sample A is in the unipolar regime for $V_G < 7$ V and $V_G > 32$ V and in the bipolar regime for $V_G < 32$ V. At B = 9 T, sample A shows a pronounced QHE, revealing QH plateaus for v = 2, 6, and 10 in the unipolar regime and a QH plateau at v = 2/3 in the bipolar regime. In a graphene p-n-p junction, the direction of the chiral edge states under a magnetic field is determined by the type of carriers. In the bipolar regime, these chiral states circulate with opposite direction in p-type and n-type regions, as shown in the schematic of Fig. 5.5b. When the edge states form at the p/n interface with full mixing equilibrium [2], the conductance can be expressed as

$$G = v_{pnp}e^2/h, (5.4)$$

with $\nu_{pnp}=\frac{|\nu_1||\nu_2|}{|\nu_1|+2|\nu_2|}$ ($\nu_1\nu_2<0,\,\nu_1,\,\nu_2=\pm 2,\pm 6,\pm 10\ldots$) The mixture of $\nu_1=2$ of the intrinsic graphene region and $\nu_2=-2$ of the doped region results in the observed $\nu=2/3$ of the first mixing filling factor. In the unipolar regime, the filling factor is given by

$$G = \min(|\nu_1|, |\nu_2|) \times e^2/h, \tag{5.5}$$

which can account for the integer QH plateau of v = 2, 6, and 10.

In Fig. 5.2a, b, we show two other graphene p-n-p junction devices (sample C and sample D), which exhibit a comparable QHE, indicating the validity of the fabrication method. We note that despite the presence of charged impurity scattering introduced by the oxide layer, the high mobility and the QH regime can still be attained in our graphene samples. To evaluate the disorder in our graphene p-n-p junction devices, we calculate the Ioffe-Regel parameter $(k_F\lambda)^{-1}$, where λ is the transport mean free path, yielding $(k_F\lambda)^{-1} = 0.5, 0, 3$, and 0.4 for samples A, C, and D, respectively. The obtained $(k_F\lambda)^{-1} < 1$ indicates that the graphene p-n-p junction samples have reasonably low disorder. Furthermore, Fig. 5.5d shows the derivative of $\mathrm{d}G/\mathrm{d}V_G$ as a function of V_G for 2 K < T < 100 K. We note that the minimum for the zeroth LL exhibits split peaks, while the minimum for the other LL only shows a single peak. The presence of the split peaks of the zeroth LL may be attributed to sublattice symmetry breaking in the samples with the small disorder strength [25], which is consistent with the aforementioned low disorder of the sample.

A schematic diagram of the energy level of the LLs in the graphene p-n-p junction is shown in Fig. 5.5e. Because of the extra carriers induced by the p-type doping, the energy of the LLs in the doped region is higher than that of the same LL index in the intrinsic region. We note that the device does not show a transition when the Fermi level crosses the LLs of the doped graphene because the chiral edge states in those

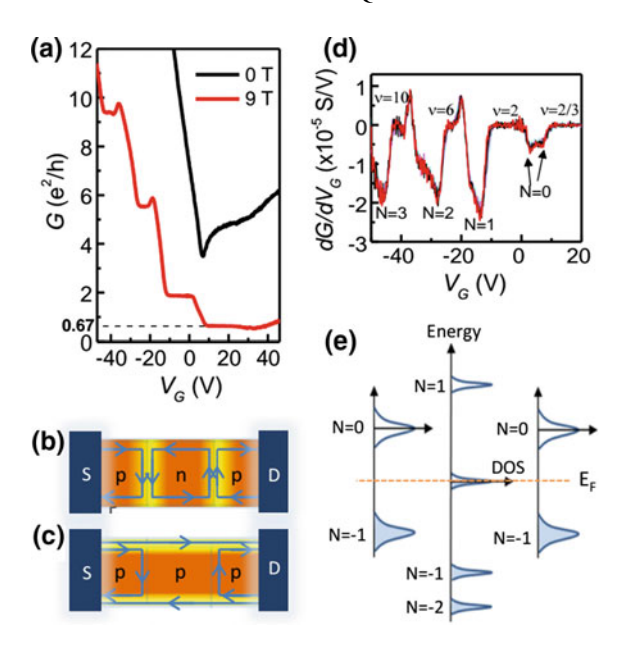


Fig. 5.5 The magnetotransport of the graphene p-n-p junctions. **a** The $G-V_G$ curves of sample A at B=0 T (black) and B=9 T (red). **b**, **c** Edge state circulation of the graphene p-n junctions in the QH regime. **b** Edge currents in p- and n-regions, which circulate in opposite directions and mix at the p-n interface in the bipolar regime. **c** Edge currents in the unipolar regime, which circulate in the same direction. **d** The differential conductance as a function of V_G , indicating the plateau-plateau transition points. **e** A schematic of the energy distribution of the LLs of the graphene p-n-p junction

regions reflect back to the same electrodes (see schematics of Fig. 5.5b, c) and do not contribute to the two-terminal resistance. Therefore, the transition of the QHE is only manifested by the LLs of the intrinsic graphene. The doped graphene regions thus act as a contact in this sense, offering a unique means to probe the LLs of the intrinsic graphene region.

We further discuss the robustness of the QH state against the thermal energy. Figure 5.5a shows the $G-V_G$ curves for $2\,\mathrm{K} < T < 100\,\mathrm{K}$. At $T=2\,\mathrm{K}$, the sample exhibits the pronounced QH plateaus at $\nu=2$, 6, 10 and $\nu=2/3$ for the unipolar and bipolar regime, respectively. The QH plateau at $\nu=2$ is particularly robust, persisting up to $T=100\,\mathrm{K}$. Conversely, the QH plateaus at $\nu=6$, 10, and 2/3 are further subjected to the influence of the thermal energy. The energy quantization of graphene in a magnetic field can be written as

$$E_N = \nu_F \sqrt{|2e\hbar BN|},\tag{5.6}$$

where v_F is the Fermi velocity and N is the LL index. The energy gap of the QH plateau at v = 2 can be estimated as $\Delta E = E_1 - E_0 \approx 1000$ K at B = 9 T. Because

the cyclotron gap, $\hbar\omega_c$, is larger than the thermal energy, k_BT , by a factor of 10 [26], the persistence of the QH plateau at $\nu=2$ for T<100 K, which is comparable to the observed critical T, is implied. Alternatively, the energy gap of the fractional-valued QH plateau at $\nu=2/3$ is smaller than that of the QH plateau at $\nu=2$ (see Fig. 5.5e), causing a weaker persistence of the QHE against thermal excitation.

5.3.5 Scaling Behavior

We now focus on the scaling behavior of the QH plateau-plateau transitions in our graphene p-n-p junction devices. In the QH regime, both the localized and extended states are critical to the development of the QHE, and the width of the QH plateaus depends on the ratio of localized to extended states [27]. At the QH plateau-plateau transition, the presence of the delocalized states results in nonzero σ_{xx} ; σ_{xy} becomes non-quantized because these states condense into a fluid state, leading to a transition region of nonzero width between quantized values [28]. The delocalization can be described by the scaling behavior of the magnetoresistance (MR) as a function of T in the transition region [29], which can be inferred as follows. In the center of a LL, the localization length ξ of electronic states diverges as $\xi \propto |\nu - \nu_c|^{-\gamma}$, where v_c is the LL center and v is its localization edge [30]. It can then be derived that the maximum slope of $d\sigma_{xy}/dv$ diverges as $T^{-\kappa}$ in the transition region, with the exponent $\kappa = p/2\gamma$, where γ is the localization length exponent and p is the inelastic scattering exponent [29, 30]. Hence, the deviation of the field from its critical value $(v - v_c)$ rescales by the factor T^{κ} as T decreases; it follows that the transition region becomes smaller as T decreases.

From Fig. 5.6a, we can extract $(dG/dv)_{max}$, the maximum of the slope for each T, in which the filling factor v is calculated using the relation v = nh/eB. We can then plot the T dependence of $(dG/dv)_{max}$ for the first and second LLs corresponding to the intrinsic region of the p-n-p junction, as shown in Fig. 5.6b. The value of $(dG/dv)_{max}$ is extracted up to the T value at which the QH plateaus are about to disappear. Sample A exhibits a scaling behavior, and $(dG/dv)_{max}$ varies linearly with T for 30 K < T < 70 K, yielding $\kappa = 0.36 \pm 0.01$ and $\kappa = 0.35 \pm 0.01$ for the first and second LLs, respectively. Here, we assume that p=2, which is generally accepted for a 2D system dominated by short-range scattering [31, 32]. This is conceivable because the carrier transport is dominated by short-range scattering for TiO_2 on graphene [33]. From the relation $\kappa = p/2\gamma$, we then obtain $\gamma = 2.7$, which is in reasonable agreement with the theoretical calculation $\gamma = 2.35$ [27], indicating that localization of the higher order LLs in our graphene p-n-p samples is governed by a scaling behavior similar to that in conventional 2D systems. At lower T, the T dependence of $(dG/dv)_{max}$ becomes smaller because the localization length approaches the intrinsic scattering length, which is T independent [14]. We define T_C as the T where the data start to deviate from the scaling behavior. It is found that T_C for the first and second LLs are comparable (approximately 30 K), suggesting that T_C is associated with the dimension of the sample but not the LL index.

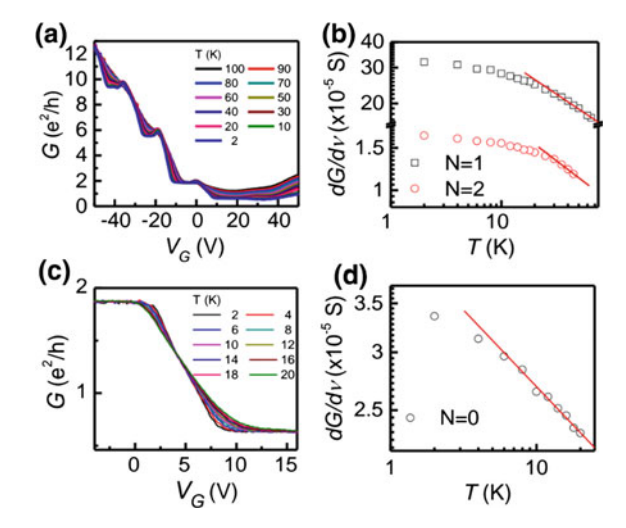


Fig. 5.6 The scaling behavior of the QH plateau-plateau transitions. **a** The $G-V_G$ curves of sample A from T=2 K to T=100 K. **b** $(\mathrm{d}G/\mathrm{d}v)_{max}$ as a function of T and the fits, which yield the scaling exponent for the first and second LLs. **c** The $G-V_G$ curves of sample A from T=2 K to T=20 K, exhibiting the transition region between the integer QH plateau v=2 and the fractional-valued QH plateau v=2/3. **d** $(\mathrm{d}G/\mathrm{d}v)_{max}$ as a function of T and the fitting of the scaling exponent for the zeroth LL

Notably, we observe the scaling behavior of the QH plateau-plateau transition between integer and fractional-valued QH plateaus of graphene. Figure 5.6c shows the $G-V_G$ curves at the transition region between the integer QH plateau $\nu=2$ and the fractional-valued QH plateau $\nu=2/3$ for T ranging from 2 to 20 K. According to the energy levels of the LLs shown in Fig. 5.5e, this transition occurs at the zeroth LL of the intrinsic graphene region. We obtain $\kappa=0.21\pm0.01$ for the zeroth LL, which is smaller than those of the first and second LLs. A reduced value of κ for the zeroth LL has been reported in the graphene Corbino device [14], which has been attributed to the dominance of electron-hole puddles, as evidenced by an inhomogeneous charge carrier distribution [13, 14]. Because the transition of the zeroth LL coincides with the charge neutrality point, the reduced κ observed in the graphene p-n-p junction may be related to the presence of the electron-hole puddles [34].

5.3.6 The MR and the Distribution of the Energy Levels of the LLs

We estimate the energy level (E_N) for the LL index to validate the assignment of the LLs of the QH plateau-plateau transition. Figure 5.7a shows the MR curves of sample A for different V_G in the unipolar regime. For -0.3 T < B < 0.3 T, we

observe negative MR, which can be attributed to weak localization (WL) [35, 36]. Beyond the WL regime, sample A exhibits positive MR, which can be explained by the classical Hall effect. Moreover, we observe oscillating peaks, which are coupled by the Shubnikov-de Haas (SdH) oscillations in σ_{xx} for -50V < V_G < -10 V. For $V_G = 0$ V V, sample A enters the QH regime for B > 3 T and shows a pronounced QH plateau at $\nu = 2$, which is consistent with the aforementioned QHE. We then construct the Landau fan diagram by identifying the value of the $1/B_N$ field corresponding to the Nth maxima and minima of the SdH oscillations and by plotting against the Landau index N at different V_G , as shown in Fig. 5.7b. The N versus $1/B_N$ data at different V_G can be fitted linearly, and these lines extrapolate and converge at y = -0.5 on the y-axis, indicating a nonzero Berry's phase of monolayer graphene [10]. From the slope of the linear fit, we can obtain the SdH oscillation period $1/B_F(V_G)$, yielding the V_G dependence of carrier density as n= $4e/hB_F(V_G)$, which is shown in Fig. 5.7c. We found that n varies linearly with V_G , and the n capacitance of the graphene device on 300-nm-thick SiO₂ is calculated as $\alpha = n(V_G)/V_G = 4.77 \times 10^{10} \text{ cm}^{-2} \text{ V}^{-1}.$

From the Landau fan diagram, the relationship between E_F and $n(V_G)$ can be derived using $B_F = E_F^2/2ev_F^2\hbar$ [37–39], where $v_F = 10^6$ m/s, as shown in the inset of Fig. 5.7d. We note that E_F varies linearly with the square root of n, which is consistent with the behavior of relativistic Dirac particles described by $E_F =$

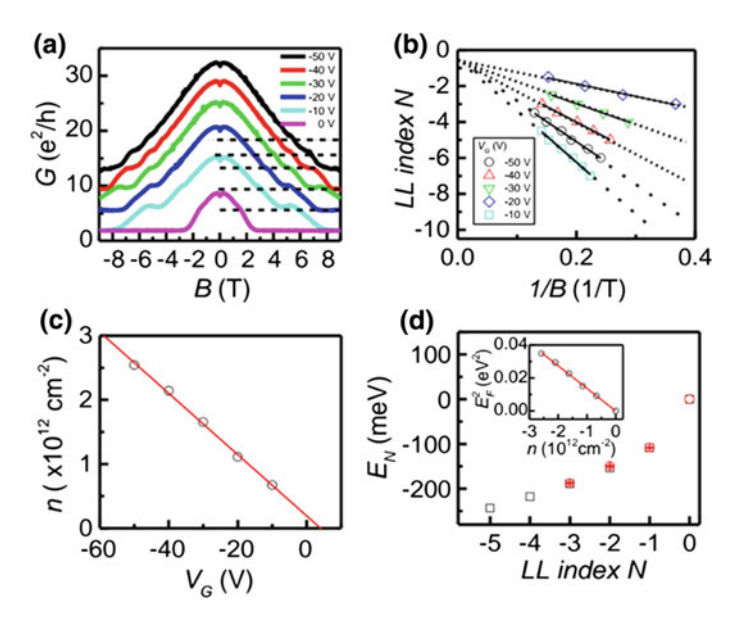


Fig. 5.7 The MR and the distribution of the energy levels of the LLs. **a** The MR, showing SdH oscillations in the unipolar regime. **b** A fan diagram showing the LL index as a function of $1/B_N$ at different V_G . **c** The carrier concentration $n = 4e/hB_F(V_G)$, which is linearly dependent on V_G , from which the carrier density capacitance α is extracted. **d** The energy of the Nth LL (E_N) as a function of the LL index. Inset: Fermi energy as a function of carrier density

 $\hbar v_F k_F = \hbar v_F \sqrt{n\pi}$ [40, 41]. We then identify $V_G(v)$ for the LL index based on the corresponding derivative minima from $\mathrm{d}G/\mathrm{d}V_G$ versus V_G curves (Fig. 5.5d). By converting $V_G(v)$ to n(v) and using the E_F-n relation, we obtain the E_N corresponding to the LL index, as shown in Fig. 5.7d. The estimated E_N versus the LL index agrees well with theoretically derived values based on $E_N = v_F \sqrt{2e\hbar BN}$ with $E_N = 0$ T, indicating the validity of the assignment of the LLs of the QH plateau-plateau transition.

5.4 Conclusion

We report distinctive magnetotransport properties of a graphene p-n-p junction prepared by controlled diffusion of metallic contacts. In most cases, materials deposited on a graphene surface introduce substantial carrier scattering, which greatly reduces the high mobility of intrinsic graphene. However, we show that an oxide layer only weakly perturbs the carrier transport, which enables fabrication of a high-quality graphene p-n-p junction through a one-step and resist-free method. The measured conductance-gate voltage $(G-V_G)$ curves can be well described by a metal contact model, which confirms the charge density depinning due to the oxide layer. The graphene p-n-p junction samples exhibit pronounced quantum Hall effect, a well-defined transition point of the zeroth Landau level (LL), and scaling behavior. The scaling exponent obtained from the evolution of the zeroth LL width as a function of temperature exhibits a relatively low value of $\kappa=0.21\pm0.01$. Moreover, we calculate the energy level for the LLs as a function of the LL index based on the distribution of plateau-plateau transition points, further validating the assignment of the LL index of the QH plateau-plateau transition.

References

- 1. A.F. Young, P. Kim, Ann. Rev. Conden. Ma. P. 2, 101 (2011)
- 2. B. Ozyilmaz, P. Jarillo-Herrero, D. Efetov, D.A. Abanin, L.S. Levitov, P. Kim, Phys. Rev. Lett. 99, 166804 (2007)
- 3. A.F. Young, P. Kim, Nat. Phys. 5, 222 (2009)
- M. Satoru, M. Sei, O. Masahiro, I. Kazuyuki, W. Kenji, T. Takashi, M. Tomoki, Jpn. J. Appl. Phys. 52, 110105 (2013)
- 5. M.I. Katsnelson, K.S. Novoselov, A.K. Geim, Nat. Phys. 2, 620 (2006)
- 6. A.V. Shytov, M.S. Rudner, L.S. Levitov, Phys. Rev. Lett. 101, 156804 (2008)
- L. Zheng, L. Ma, G. Shi, W. Zhou, Y. Gong, S. Lei, X. Yang, J. Zhang, J. Yu, K.P. Hackenberg,
 A. Babakhani, J.-C. Idrobo, R. Vajtai, J. Lou, P.M. Ajayan, Nat. Nanotechnol. 8, 119 (2013)
- 8. A.K. Geim, K.S. Novoselov, Nat. Mater. 6, 183 (2007)
- K.S. Novoselov, A.K. Geim, S.V. Morozov, D. Jiang, M.I. Katsnelson, I.V. Grigorieva, S.V. Dubonos, A.A. Firsov, Nature 438, 197 (2005)
- 10. Y. Zhang, Y.-W. Tan, H.L. Stormer, P. Kim, Nature 438, 201 (2005)
- K.S. Novoselov, E. McCann, S.V. Morozov, V.I. Fal'ko, M.I. Katsnelson, U. Zeitler, D. Jiang, F. Schedin, A.K. Geim, Nat. Phys. 2, 177 (2006)

References 53

 A.H. Castro Neto, F. Guinea, N.M.R. Peres, K.S. Novoselov, A.K. Geim, Rev. Mod. Phys. 81, 109 (2009)

- A.J.M. Giesbers, U. Zeitler, L.A. Ponomarenko, R. Yang, K.S. Novoselov, A.K. Geim, J.C. Maan, Phys. Rev. B 80, 241411 (R) (2009)
- 14. E.C. Peters, A.J.M. Giesbers, M. Burghard, K. Kern, Appl. Phys. Lett. 104, 203109 (2014)
- 15. S.-Y. Chen, P.-H. Ho, R.-J. Shiue, C.-W. Chen, W.-H. Wang, Nano. Lett. 12, 964 (2012)
- 16. J.R. Williams, L. DiCarlo, C.M. Marcus, Science 317, 638 (2007)
- 17. H.C. Cheng, R.J. Shiue, C.C. Tsai, W.H. Wang, Y.T. Chen, ACS Nano. 5, 2051 (2011)
- 18. B. Huard, N. Stander, J.A. Sulpizio, D. Goldhaber-Gordon, Phys. Rev. B 78, 121402 (2008)
- 19. T. Mueller, F. Xia, M. Freitag, J. Tsang, P. Avouris, Phys. Rev. B 79, 245430 (2009)
- 20. R. Nouchi, K. Tanigaki, Appl. Phys. Lett. **105**, 033112 (2014)
- 21. R. Nouchi, K. Tanigaki, Appl. Phys. Lett. 96, 253503 (2010)
- 22. F.N. Xia, V. Perebeinos, Y.M. Lin, Y.Q. Wu, P. Avouris, Nat. Nano. 6, 179 (2011)
- 23. S. Cho, M.S. Fuhrer, Phys. Rev. B 77, 081402 (2008)
- F.-Y. Shih, S.-Y. Chen, C.-H. Liu, P.-H. Ho, T.-S. Wu, C.-W. Chen, Y.-F. Chen, W.-H. Wang, AIP Adv. 4, 067129 (2014)
- 25. F. Ortmann, S. Roche, Phys. Rev. Lett. 110, 086602 (2013)
- K.S. Novoselov, Z. Jiang, Y. Zhang, S.V. Morozov, H.L. Stormer, U. Zeitler, J.C. Maan, G.S. Boebinger, P. Kim, A.K. Geim, Science 315, 1379 (2007)
- 27. B. Huckestein, Rev. Mod. Phys. **67**, 357 (1995)
- 28. S.L. Sondhi, S.M. Girvin, J.P. Carini, D. Shahar, Rev. Mod. Phys. 69, 315 (1997)
- 29. H.P. Wei, D.C. Tsui, M.A. Paalanen, A.M.M. Pruisken, Phys. Rev. Lett. 61, 1294 (1988)
- 30. A.M.M. Pruisken, Phys. Rev. Lett. 61, 1297 (1988)
- 31. S. Koch, R.J. Haug, K.V. Klitzing, K. Ploog, Phys. Rev. Lett. **67**, 883 (1991)
- 32. T. Brandes, Phys. Rev. B **52**, 8391 (1995)
- 33. K.M. McCreary, K. Pi, R.K. Kawakami, Appl. Phys. Lett. 98, 192101 (2011)
- 34. J. Martin, N. Akerman, G. Ulbricht, T. Lohmann, J.H. Smet, K. Von Klitzing, A. Yacoby, Nat. Phys. 4, 144 (2008)
- Morozov SV, Novoselov KS, Katsnelson MI, Schedin F, Ponomarenko LA, Jiang D, Geim AK (2006) Phys. Rev. Lett. 97
- P.-H. Wang, Fu-Yu. Shih, S.-Y. Chen, A.B. Hernandez, P.-H. Ho, L.-Y. Chang, C.-H. Chen,
 H.-C. Chiu, C.-W. Chen, W.-H. Wang, Carbon 93, 353 (2015)
- 37. I.A. Luk'yanchuk, Y. Kopelevich, Phys. Rev. Lett. 93, 166402 (2004)
- 38. D.E. Soule, J.W. McClure, L.B. Smith, Phys. Rev. 134, A453 (1964)
- 39. C. Berger, Z. Song, X. Li, X. Wu, N. Brown, C. Naud, D. Mayou, T. Li, J. Hass, A.N. Marchenkov, E.H. Conrad, P.N. First, W.A. de Heer, Science 312, 1191 (2006)
- 40. P.R. Wallace, Phys. Rev. 71, 622 (1947)
- 41. G.P. Mikitik, Y.V. Sharlai, Phys. Rev. Lett. 82, 2147 (1999)

Chapter 6 Extrinsic Origin of Persistent Photoconductivity in Monolayer MoS₂ Field Effect



6.1 Introduction

Following the discovery of graphene, [1–3] two-dimensional (2D) materials have emerged as one of the most important research topics in condensed matter physics because of promising applications of these materials [4–6]. In particular, semiconducting layered materials, [7, 8] such as transition metal dichalcogenides (TMD), [9, 10] can complement graphene because of their intrinsic bandgaps [11, 12]. In particular, molybdenum disulfide (MoS₂) is a layered semiconducting TMD and therefore exhibits a bandgap, [13, 14] high mobility, [15, 16] and strong mechanical properties [17]. Moreover, unique physical properties, including spin-valley coupling and the layer dependence of the band structure in MoS₂, have been demonstrated [18–20]. The combination of these interesting properties has made MoS₂ very attractive for new functionalities such as sensors, [21–23] logic circuits [24, 25] and optoelectronic devices [26–30].

Recently, high photoresponsivity [31, 32], the photovoltaic effect [29] and the photothermoelectric effect [28] have been reported in monolayer MoS₂-based photodetectors and phototransistors. Optoelectronic studies on these MoS₂ devices demonstrated persistent photoconductivity (PPC), which is sustained conductivity after illumination is terminated [32–35]. However, a detailed understanding of PPC and its mechanism in MoS₂ are still not available. The origin of the trap states in MoS₂, which leads to the PPC effect, remains under debate [36–39]. Moreover, the PPC effect modifies the transport properties of MoS₂ samples, which are sensitive to the history of photon irradiation. Therefore, it is essential to understand the PPC effect to control transport phenomena in MoS₂.

Here, we present a systematic study of PPC in monolayer MoS_2 field effect transistors. The PPC dependence on the temperature, the photon dose, and the excitation energy enabled us to attribute the PPC in MoS_2 to random localized potential fluctuations that hinder the recombination of photoexcited electron-hole pairs. Comparing the PPC in suspended and substrate-supported MoS_2 devices led us to conclude that

PPC originates primarily from extrinsic sources. Moreover, we could correlate PPC phenomena with transport, whereby carriers transfer among nearest low-potential puddles. This work was done in collaboration with Yueh-Chun Wu.

6.2 Fabrication

MoS₂ flakes were mechanically exfoliated onto octadecyltrichlorosilane (OTS) selfassembled monolayer (SAM) functionalized SiO₂ (300 nm)/Si substrates. The surface of the OTS-functionalized SiO₂/Si substrate was hydrophobic with a typical contact angle above 110°. The hydrophobic surface decreased the number of absorbate molecules, thereby decreasing the charged-impurity scattering in MoS₂ and charge traps [40]. First, the MoS₂ flakes were identified and characterized under an optical microscope using variations in contrast. Figure 6.1a shows a typical optical microscopy image of the MoS₂ sample after deposition of the electrode. Figure 6.1b shows the photoluminescence (PL) spectrum of a typical monolayer and bilayer MoS₂ sample that were fabricated on OTS-functionalized substrates, showing the exciton peak A and peak B. Due to the difference in the quantum efficiency, the intensity of the exciton peak A and peak B in the monolayer MoS₂ are larger than those in the bilayer MoS₂ samples. Another PL peak (I) at $\simeq 1.6$ eV corresponding to the indirect interband transition was observed in bilayer MoS₂. Figure 6.1c shows a Raman spectrum (blue curve) of a monolayer MoS2 sample with two characteristic peaks at 388.7 and 407.0 \mbox{cm}^{-1} that correspond to the E_{2g} and A_{1g} resonance modes, respectively. The difference between the two peaks is $\simeq 18.3$ cm⁻¹, which is consistent with that obtained for the monolayer MoS₂ from previous reports [41]. For comparison, the Raman spectra of the bilayer and trilayer MoS₂ samples are also shown in Fig. 6.1c.

First, the MoS₂ flakes were identified and characterized under an optical microscope using variations in contrast and then were examined by Raman and photoluminescence spectra. We adopted resist-free fabrication to prevent contamination of the MoS₂ samples from the resist residue of the conventional lithography process. We used nanowire as a shadow mask to deposit metallic contacts (Au, 50 nm) with an electron-beam evaporator at a base pressure of 1.0×10^{-7} Torr in a two-probe geometry using a residue-free approach [42, 43] to minimize contamination from the conventional lithography process. The MoS₂ devices were transferred into a cryostat (Janis Research Company, ST-500) for electrical and optical characterization. The samples were stored under a high vacuum of 1×10^{-6} Torr to minimize the undesirable adsorption of chemical substances. This procedure enabled us to investigate the photoresponse of MoS₂ without interference from the gas adsorbate effect [44]. Figure 6.1d shows the source-drain current (I_{SD}) as a function of the source-drain bias (V_{SD}), which is linear over the small bias region.

6.3 Measurement Method 57

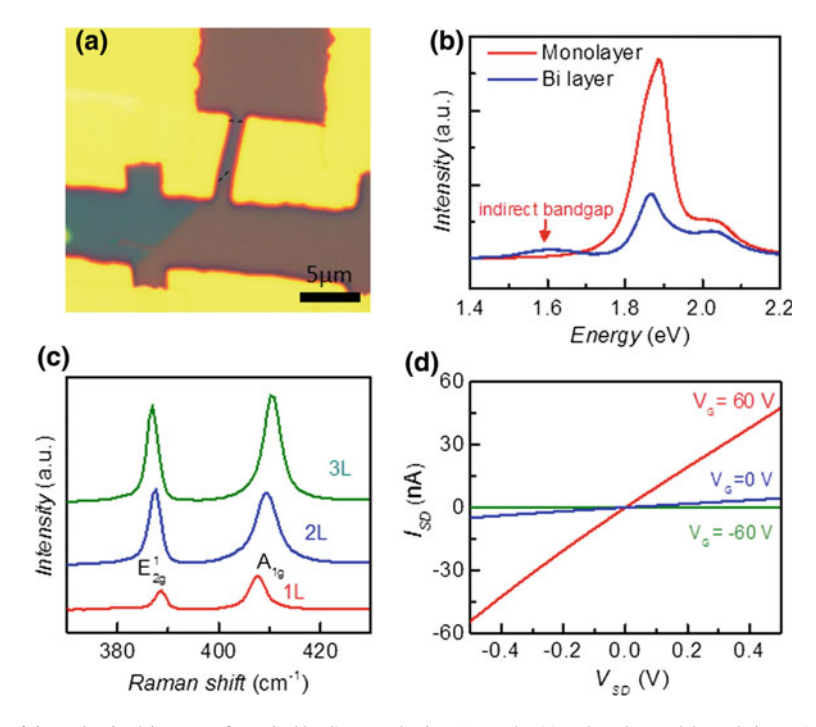


Fig. 6.1 a Optical image of MoS₂/OTS FET device (sample A). The channel length is $\simeq 1~\mu m$. b PL spectra of monolayer and bilayer MoS₂ on OTS-functionalized substrates. c Raman spectra of monolayer, bilayer, and trilayer MoS₂ on OTS-functionalized substrates, showing E_{2g} and A_{1g} peaks of different MoS₂ layers. d The $I_{SD}-V_{SD}$ curve of the MoS₂/OTS/SiO₂ device

6.3 Measurement Method

As mentioned in Chap. 3, the measurement system that consists of optical microscopy, and Raman/PL spectroscopy is used in this experiment. A solid-state CW laser (Nd: YAG, 532 nm) was employed as the light source in the photoresponse measurements. The incident light was guided into the microscope and focused by an objective ($10\times$, NA 0.3) with a spot size of $\simeq 1.5~\mu m$. The power density on the sample was estimated at $\simeq 5.6\times 10^4~W/cm^2$ for an illumination power of 1 mW. For Raman and PL spectroscopy, a $100\times$ objective (NA 0.6) was used with a spot size of $\simeq 0.7~\mu m$. A mercury-xenon lamp (Hamamatsu Photonics, 150 W) was used as the broadband white light source for the excitation energy dependence of photoresponse. The white light was selected using a band-pass filter for peak wavelengths from 450 to 850 nm (spacing: 50 nm; full width at half maximum (FWHM): 40 nm). The dependence of the photoresponse on the excitation energy was measured by fixing the power density at 15.9 W/cm² for different excitation energies.

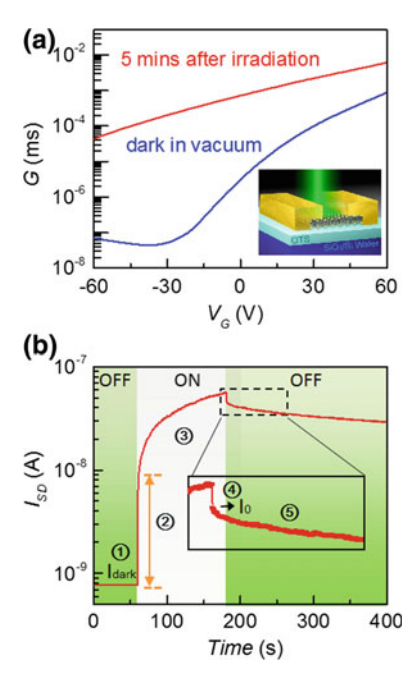


Fig. 6.2 The PPC effect in a monolayer MoS_2 transistor. a Conductance as a function of V_G in the dark and after illumination at room temperature in a vacuum, showing that the conductance of the device is greatly enhanced after illumination and remains in a high-conductivity state for a long period of time. Inset: a schematic of a MoS_2 device on an OTS-functionalized substrate. b The photoresponse of the MoS_2 device for $V_G = 0$ V and $V_{SD} = 50$ mV, which can be classified into 5 stages. In addition to the photoresponse due to band-to-band transition (stages 2 and 4), the device exhibits a slow increase in the photocurrent under illumination (stage 3) and the PPC effect (stage 5)

6.4 Experimental Results and Discussion

6.4.1 The PPC Effect in a Monolayer MoS₂ Transistor

Figure 6.2a shows the two-probe transconductance of sample A as a function of the back-gate voltage $(G-V_G)$. The MoS_2 device exhibited typical n-type channel characters with a mobility of 0.7 cm²/Vs and an on/off ratio of 2×10^4 . The MoS_2 transistor was then illuminated by a laser (wavelength = 532 nm) with a spot size of $\simeq 1.5~\mu m$. After the illumination was terminated, the conductance of the device was greatly enhanced and remained in a high-conductivity state for a time period from 2 min to 2 h, depending on the irradiated photo-dose. It is noted that the longer the illumination time, the higher the conductance.

We subsequently investigated the PPC effect in the MoS_2 transistor in greater detail. Figure 6.2b shows the temporal evolution of the source–drain current $(I_{SD} - t)$

in vacuum. The fast response of the current (stage 2) was attributed to a band-to-band transition that created conducting electrons and holes [26, 27]. After the initial upsurge from the dark current (I_{dark}) level, the I_{SD} increased gradually to over 2 orders of magnitude (stage 3) above the dark current. This slow increase in the I_{SD} could not be attributed to the common band-to-band transition. After the laser irradiation was terminated, the I_{SD} exhibited a rapid drop because of the band-to-band transition (stage 4), followed by noticeable PPC (stage 5).

We characterized the PPC relaxation by choosing the starting point of the PPC (I_0) in Fig. 6.2b as the first data point after the photocurrent sharply dropped. Here, we assumed that the band-to-band recombination time was comparable to the lifetime of the PL ($\simeq 100$ ps) [45, 46]. Because the time delay of the PC measurement was 200 ms, which was much larger than the photocurrent relaxation due to band-to-band recombination, the photocurrent after I_0 was dominated by PPC.

This PPC effect was consistently observed in all of our 10 MoS_2 devices. For MoS_2 under ambient conditions, a short photoresponse time below 1 s has been previously reported [26] and attributed to the presence of gas adsorbates [44]. However, adsorbates were not a significant factor in the present study because our MoS_2 samples were treated in vacuum.

We first discuss the temperature dependence of PPC in the MoS_2 devices, which provides important indications of the PPC mechanism [47]. Figure 6.3a is a comparison of three characteristic PPC relaxations for sample A at T=80, 180, and 300 K. For purposes of comparison, the dark level was subtracted, and the PPC was normalized by I_0 . It is noted that the PPC was more pronounced at high temperatures, although the photocurrent decreased very fast and the PPC was considerably weakened at low temperatures. The temperature dependence of the PPC was measured by heating the samples up to room temperature, allowing the carriers to relax to equilibrium, [48] and then cooling the samples down in the dark to the target temperature. The PPC relaxation curves were well-fitted by a single stretched exponential decay, [49]

$$I_{PPC}(t) = I_0 \exp[-(t/\tau)^{\beta}],$$
 (6.1)

where τ is the decay time constant, and β is the exponent. The stretched exponential decay has been widely used to model relaxation processes in complex and slowly relaxing materials [47–50]. Therefore, this photocurrent decay suggests that PPC is related to disorders in the MoS₂ devices.

The fitted τ and β values at different temperatures are shown in Fig. 6.3b. Clearly, the MoS₂ device exhibited a shorter τ at low temperatures, which is a signature of the random local potential fluctuations (RLPF) model [48, 51]. In the RLPF model, local potential fluctuations arise either because of intrinsic disorders in the materials or extrinsic charged impurities. Therefore, low-energy electrons and holes become localized in potential minima and are spatially separated, resulting in a long recombination lifetime. The thermal excitation of carriers to higher energy states above the mobility edge produces a photocurrent after the irradiation is terminated, resulting in the PPC effect. At low temperature, the carriers are well-confined inside

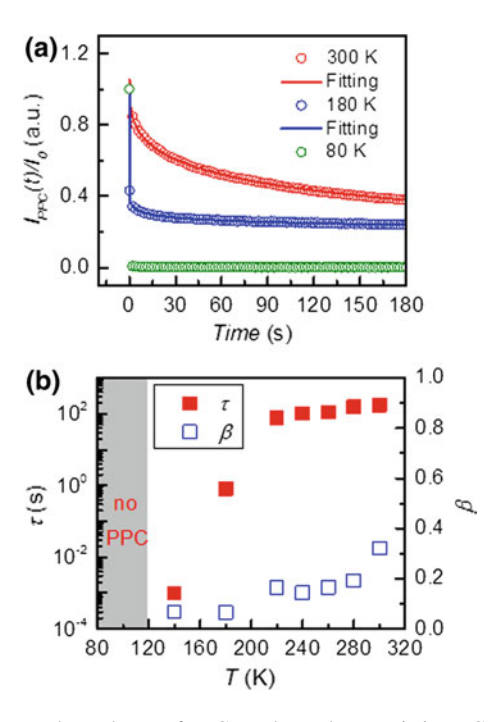


Fig. 6.3 The temperature dependence of PPC. **a** Three characteristic PPC relaxations (circles) at T=80, 180, and 300 K. PPC is more pronounced at higher temperatures, but is greatly suppressed at T=80 K. The PPC relaxations are well described by a stretched exponential decay (solid line). The stretched exponential decay is $I_{PPC}=I_0exp\left[-(t/\tau)^{\beta}\right]$ with the dark current subtracted. I_0 in the PPC relaxation curves is normalized to 1 for comparison of the decay rate. **b** The temperature dependence of the decay time constant (τ) and the exponent (β) . The grey region indicates the temperature range over which PPC is not observed

charge traps and therefore, negligible PPC is observed. This RLPF model has been widely used to explain PPC in II-VI compound semiconductors [48, 50, 51]. However, this model has not been used to explain the PPC effect in 2D TMD materials.

6.4.2 Temperature Dependence of PPC Relaxation

Before each measurement, the MoS_2 samples were warmed up to room temperature to ensure that the dark current had reached equilibrium and then cooled down in the dark to the desired temperature. Detailed data on the temperature dependence of PPC are shown in Fig. 6.4, in which the PPC is normalized by I_0 for purposes of comparison. PPC clearly weakened as the temperature decreased for sample A and sample B. As shown in Fig. 6.3b, both τ and β decreased as the temperature decreased. At low temperatures, the PPC dropped more quickly for t < τ but became more persistent

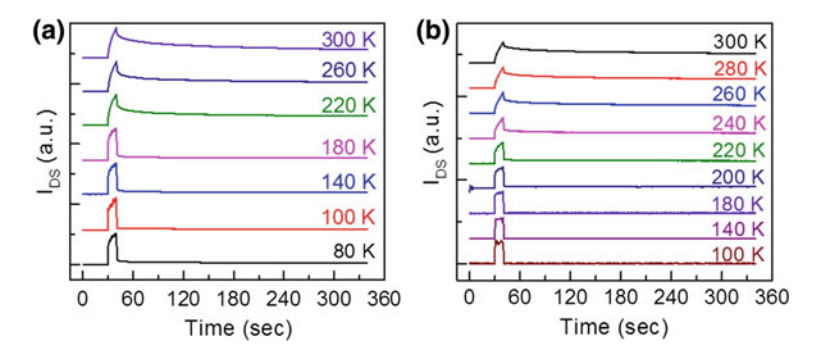


Fig. 6.4 Temporal evolution of the photoresponse for $\bf a$ sample A and $\bf b$ sample B at different temperatures. The PPC is normalized by I_0 and offset vertically for purposes of comparison

for $t > \tau$, which could be accurately described by a stretched exponential function with a small β [52].

6.4.3 The Subtract Effect of PPC

The PPC in the MoS₂ samples was attributed to the RLPF model in which the potential fluctuations originate from extrinsic [36, 53] or intrinsic [54, 55] sources. Extrinsic adsorbates or chemical impurities in the vicinity of the MoS₂ samples can lead to trap states [36, 53]. Alternatively, sulfur vacancies [37] and the formation of MoO₃ in bulk MoS₂ have intrinsic causes. We determined the origin of the potential fluctuations by investigating the substrate effect on the PPC. We first measured the PPC in suspended MoS₂ devices that were fabricated by exfoliating monolayer MoS₂ onto SiO₂/Si substrates with trenches (width $\simeq 2 \,\mu m$). Figure 6.5a shows the optical images of a fabricated suspended MoS₂ device before and after deposition of the electrodes. To verify the suspension of the MoS₂ sample, we measured the PL spectra of the sample, which are very sensitive to the existence of SiO₂/Si substrates [56]. Figure 6.5b is a comparison of the PL spectra of a suspended MoS₂ device (sample B) and a SiO₂-supported MoS₂. The PL spectrum of the suspended MoS₂ exhibited a strong exciton peak (A), along with trion (A⁻) and exciton (B) peaks. The presence of the pronounced exciton peak A indicated that the MoS₂ sample was free from the strong n-type doping effect of the SiO₂ substrate, [56] indicating a suspended structure. In contrast, only trion (A⁻) and exciton (B) peaks were observed in the PL spectrum of SiO₂-supported MoS₂.

Next, we discuss the photoresponse of the suspended MoS_2 (sample B) that is shown in Fig. 6.5c. Interestingly, sample B exhibited a negligible PPC effect at T=300 K, in contrast to the photoresponse of the substrate-supported MoS_2 at the same temperature. Only the photoresponse from the band-to-band transition was observed in this suspended MoS_2 device. The absence of the PPC effect in this

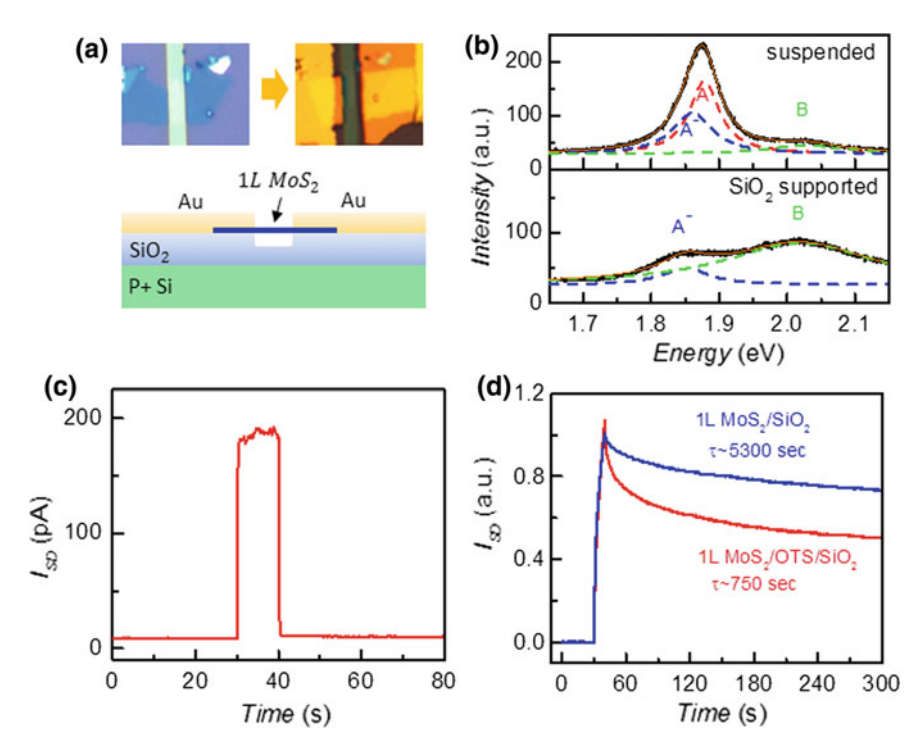


Fig. 6.5 The substrate effect of PPC. **a** Upper panel: optical images of the suspended MoS₂ device before and after deposition of the electrode. Lower panel: a schematic of the suspended monolayer MoS₂ device. **b** PL spectra of suspended (upper panel) and SiO₂-supported (lower panel) 20 monolayer MoS₂ devices. **c** Photoresponse of the suspended MoS₂ device showing negligible PPC at T = 300 K ($V_G = 0V$, $V_{SD} = 5V$). **d** Photoresponses of monolayer MoS₂ on OTS-functionalized and conventional SiO₂ substrates ($V_G = 0V$, $V_{SD} = 5V$). The photocurrents are normalized by I_0 for purposes of comparison

control sample clearly indicated that the potential fluctuations in our MoS₂ devices had extrinsic sources. We also compared the PPC effect for MoS₂ devices that were fabricated on an OTS-functionalized SiO₂ surface and those were fabricated on conventional SiO₂ substrates, as shown in Fig. 6.5d. The PPC effect in the MoS₂/SiO₂ device was stronger than that in the MoS₂/OTS/SiO₂ device. This substrate effect was consistently observed in several samples, suggesting that there were fewer charge traps in the MoS₂/OTS/SiO₂ devices than in the MoS₂/SiO₂ device. This difference was reasonable because the OTS-functionalized SiO₂ surface is known to be hydrophobic and could therefore reduce surface adsorbates, [57] resulting in smaller potential variations. Further study is required to identify these extrinsic sources in detail, e.g., gas adsorbates and/or chemical impurities on the SiO₂ interface. Nevertheless, our finding demonstrates the importance of extrinsic sources, thereby providing a means of eliminating the PPC effect to control the photoresponse in TMD materials.

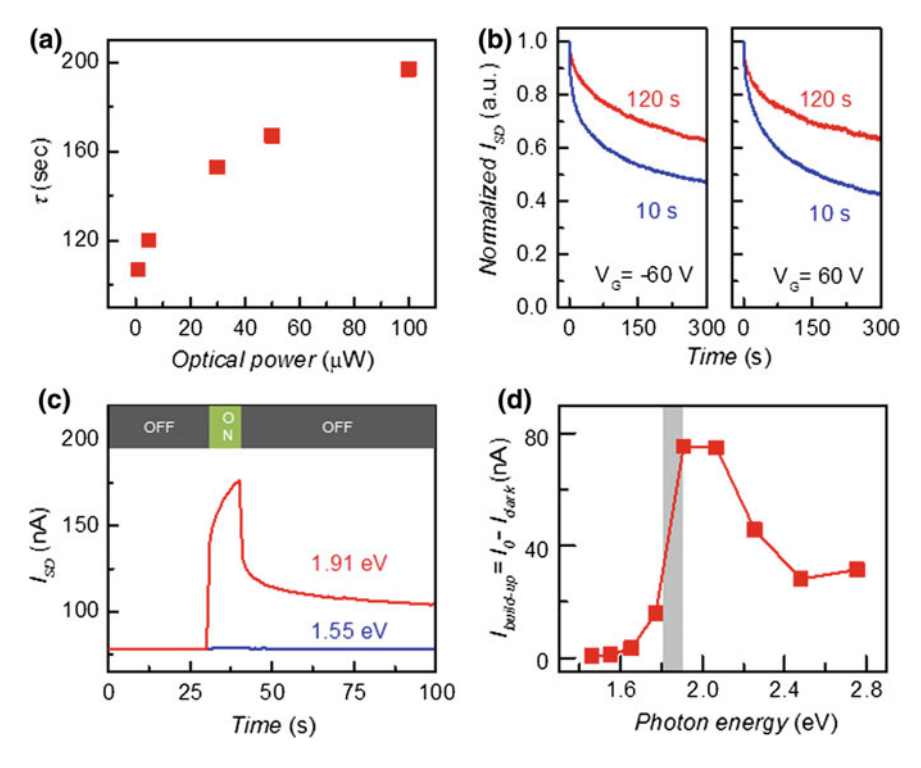


Fig. 6.6 Photon dose and excitation wavelength dependences of the PPC relaxation. **a** Excitation power dependence of the decay time constant for $V_G = -60 \,\mathrm{V}$, $V_{SD} = -50 \,\mathrm{mV}$. **b** The PPC relaxations for different illumination times (10 s and 120 s) at $V_G = \pm 60 \,\mathrm{V}$ and $V_{SD} = 50 \,\mathrm{mV}$. **c** The temporal evolution of I_{SD} for excitation energies below ($E_{ex} = 1.55 \,\mathrm{eV}$) and above ($E_{ex} = 1.91 \,\mathrm{eV}$) the bandgap at $T = 300 \,\mathrm{K}$ and $V_G = 0 \,\mathrm{V}$. **d** The PPC build-up level ($I_{build-up}$) at different excited photon energies and $V_G = 0 \,\mathrm{V}$. The photon dose and excitation energy dependences of the PPC are consistent with the RLPF model in the monolayer MoS₂ devices

6.4.4 Discussion of PPC Mechanism

We now present the PPC dependence on the photon dose and the excitation energy to further validate the RLPF mechanism in our MoS_2 samples. Figure 6.6a shows the excitation power dependence of τ at room temperature, where the PPC increases with the excitation power. In the RLPF model, more carriers are excited under higher photon doses, and more electrons and holes can redistribute to occupy the sites of the local potential minima. This redistribution of carriers is therefore enhanced under high excitation power, resulting in a larger τ after the photoexcitation is terminated [50]. Figure 6.6b shows the PPC relaxation for different illumination times at room temperature, where τ increases with the illumination time. This behavior is similar to the effect of excitation power. Therefore, the PPC dependence on the photon dose in MoS_2 devices is in good agreement with the RLPF mechanism.

We further investigate the PPC of monolayer MoS₂ at different excitation energies ranging from 1.46 to 2.75 eV, which includes the optical bandgap in monolayer MoS₂ $\simeq 1.8$ eV [13, 14]. Figure 6.6c is a comparison of the temporal evolution of the photoresponse for excitation energies below ($E_{ex} = 1.55 \,\mathrm{eV}$) and above ($E_{ex} = 1.91 \text{ eV}$) the bandgap. While the $I_{SD} - t$ curve for $E_{ex} = 1.91 \text{ eV}$ exhibites a typical photoresponse (which is similar to that in Fig. 6.1b), the photoresponse is insignificant for $E_{ex} = 1.55$ eV. Figure 6.6d shows the excitation energy dependence of the PPC build-up level $(I_{build-up})$, which is defined as $I_0 - I_{dark}$. Here, $I_{build-up}$ represents the charging process in which photoexcited carriers fill up the local potential minimum during illumination. The photoresponse is clearly activated at $E_{ex} \sim 1.8$ eV, showing that the bandgap of monolayer MoS₂ is related to the PPC [58]. In the RLPF model, $I_{build-up}$ is initiated by the photoexcited carriers through the band-to-band transition, which are subsequently confined by the trap states. Therefore, PPC can only occur when the photon energy is higher than the bandgap. To briefly summarize, our observations of the PPC dependence on the temperature, the substrate effect, the photon dose, and the excitation energy fully support the RLPF model as the mechanism of PPC in the monolayer MoS₂ devices.

In addition to RLPF, two other mechanisms, large lattice relaxation (LLR) [59, 60] and the microscopic barrier (MB) [61, 62], are well-known mechanisms for PPC in a variety of materials, including mixed crystals, semiconductors, and heterostructures. In the LLR model, electrons are photoexcited from deep-level traps, and an energy barrier prevents the recapture of the electrons, [59, 63] resulting in the PPC effect. Because the recapture is a thermally activated process, the PPC due to LLR is more pronounced at low temperatures, which is inconsistent with our observations in sample A and sample B. Another feature of the PPC that results from LLR is that a photocurrent can be activated by excitation from deep-level traps to conduction bands [64] with energies below that of the bandgap, which also contradicts the observed dependence of the PPC on the excitation energy. The MB is another mechanism for PPC in which photoexcited electron-hole pairs are spatially separated by a macroscopic potential barrier, followed by charge accumulation or trapping by barriers/spacers [61, 62]. Recent studies on various structures, including MoS₂/graphene, [30] quantum-dot/graphene [65] and chlorophyll/graphene [66] heterostructures, demonstrated noticeable PPC due to this MB model. However, there were no such artificially created structures in our MoS₂ devices that could yield a macroscopic potential barrier. The PPC effect in the MB model also follows a singleexponential decay, [61] unlike the stretched exponential decay that was observed in our samples. We therefore conclude from our experimental data that LLR and MB are not mechanisms for PPC in our MoS₂ devices.

6.4.5 The Relationship Between the PPC Effect and Transport Behavior

We consider the connection between the PPC effect and the transport properties of the MoS₂ devices. Figure 6.7a is an Arrhenius plot of the conductance of sample C at different V_G values and shows that insulating behavior (dG/dT > 0) was found over the temperature range 80 K < T < 300 K. For T > 200 K, the MoS₂ sample exhibited thermally activated behavior, where the activation energy was extracted from the linear fit ($E_a = 98 \text{ meV}$ at $V_G = 0 \text{ V}$). The carrier transport in this temperature regime could be described by a percolation model, in which conduction occurs via a network of spatially distributed charge puddles [67]. The activation energy then corresponded to the average potential barrier of the charge puddles. For $80 \,\mathrm{K} < T < 200 \,\mathrm{K}$, the correlation of the puddles decreased because of the decrease in the thermal energy, and the carriers could only conduct by tunneling between localized states [67]. Therefore, there was a phase transition from localized to percolation transport. The transition temperature of sample C was $T_{\rm C} \sim 200$ K, which corresponded to the temperature at which the $G-T^{-1}$ curve deviated from thermally activated behavior. To compare the temperature dependence of the PPC and transport properties, we plot $I_{build-up}$ as a function of temperature in Fig. 6.7b. The PPC is insignificant for $T < 200 \,\mathrm{K}$ because of the low conductivity in the localized transport regime. Notably, $I_{build-up}$ exhibited an activated behavior for T > 200 K, where the transition temperature coincided with the T_c value that was extracted from the transport behavior. $I_{build-up}$ could be described by a percolation approach [47]

$$I_{build-up} \propto (T - T_C)^{\mu},\tag{6.2}$$

where μ is the characteristic exponent. We found that this function fits the data reasonably well ($\mu = 2.6$), indicating that the PPC relaxation was consistent with the percolation transport picture.

6.4.6 Fitting of the PPC Relaxation Curves

To verify the validity of stretched exponential decay for describing the observed PPC in monolayer MoS_2 , we consider other possible relaxation approaches, including single exponential, double exponential and logarithmic decay. The fitting results of two representative PPC relaxation curves at $T=300 \, \text{K}$ and 180 K by these different schemes are shown in Fig. 6.8. It can be seen that only the stretched exponential decay yields satisfactory fits for the whole temporal range at different temperatures. As mentioned in Sect. 6.4.1, the observed stretched exponential decay of the PPC relaxation in our MoS_2 devices suggests a disordered system, which is consistent with the transport model discussed in Fig. 6.7.

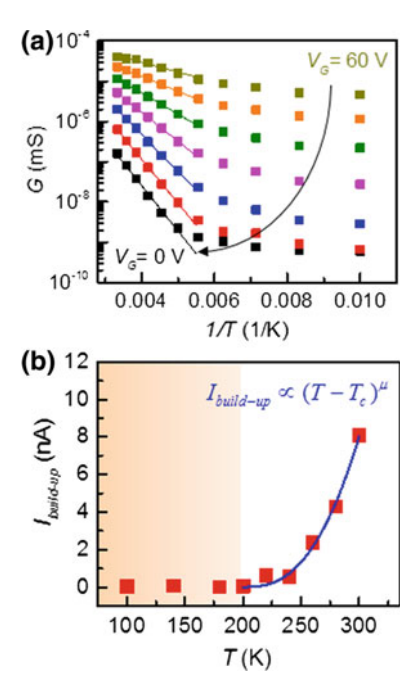


Fig. 6.7 Correlations between PPC and transport behaviors. **a** The Arrhenius plot for the conductance of sample C at different V_G values. The solid lines indicate linear fits in the thermally activated regime. **b** The temperature dependence of the PPC buildup level $(I_{build-up})$ at $V_G = 0$ V. For T > 200 K, $I_{build-up}$ is well described by a percolation model, which is shown as a solid line. The shaded region denotes the temperature regime over which transport is dominated by tunneling between localized states

6.4.7 Gate Voltage Dependence of the PPC

We discuss the back gate voltage (V_G) dependence of the PPC relaxation here. We show the PPC relaxation for $V_G = -60 \,\mathrm{V}$ and $V_G = +60 \,\mathrm{V}$ in Fig. 6.9a (also in Fig. 6.6b), as well as the V_G dependence of τ in Fig. 6.9b. The position of Fermi level, which is controlled by V_G , can greatly affect the carrier density and consequently the conductance in the MoS₂ channel. This V_G dependence of conductance is revealed in Fig. 6.2a and the related discussion. Nevertheless, the PPC relaxation is mainly determined by the density of the trap states and the extent of the carrier trapping in the RLPF model. Because there are various possible sources of trap states, including electron traps, hole traps, and mid-gap states in MoS₂ samples, [68] it is plausible that the strength of the PPC is correlated to the density of the trap states as the Fermi level is tuned with V_G . However, we note that the correlation may be complicated and further study is required to elucidate detailed V_G dependence of the PPC effect.

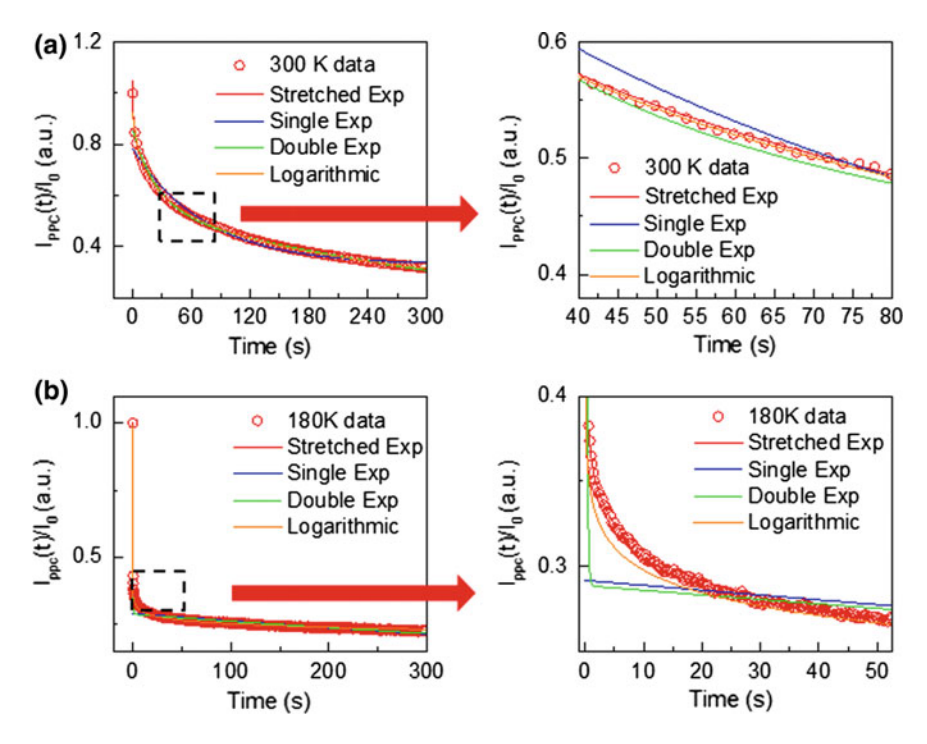


Fig. 6.8 Two representative PPC relaxation curves at $\mathbf{a} T = 300 \,\mathrm{K}$ and $\mathbf{b} 180 \,\mathrm{K}$ and the fits with various schemes, including stretched exponential, single exponential, double exponential and logarithmic decay

6.4.8 Transport Characteristics of the MoS₂ FET

In addition to characterizing the transport behavior of sample B, we show the transfer curves for sample A at different temperatures in Fig. 6.10a. Figure 6.10b shows an Arrhenius plot for the conductance of sample A at different V_G values. The transport behavior of sample A could be classified into three different regimes. (1) For $T>240\,\mathrm{K}$, the MoS2 sample exhibited metallic behavior where σ decreased rapidly with the temperature. Over this temperature range, carriers above the mobility edge dominated the transport, resulting in metallic behavior. (2) For $160\,\mathrm{K} < T < 240\,\mathrm{K}$, the sample exhibited thermally activated behavior. The carrier transport in this temperature regime could be described by a percolating picture in which conduction occurred via a network of spatially distributed puddles. (3) For $80\,\mathrm{K} < T < 160\,\mathrm{K}$, the correlation of the puddles decreased because of the decrease in the thermal energy, and the carriers could only conduct by tunneling between localized states. Similar to sample B, the build-up level of the PPC was closely related to the carrier transport, which exhibited percolation behavior ($\mu=2.2$) above the transition temperature $T_{\rm C}=160\,\mathrm{K}$, as shown in Fig. 6.10c.

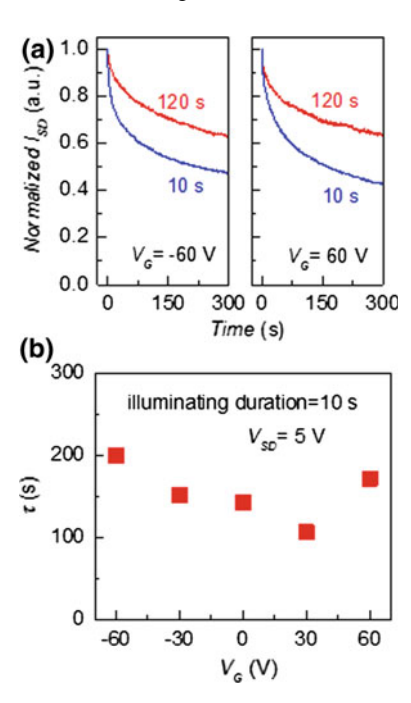


Fig. 6.9 a The normalized PPC relaxation curves at $V_{SD}=50$ mV under $V_G=-60$ V (left panel) and $V_G=60$ V (right panel). Two different irradiation duration (10 s and 120 s) were used to excite the MoS₂ sample. No significant difference between the PPC relaxation for $V_G=60$ V and $V_G=-60$ V was observed. **b** The fitted τ versus applied V_G at $V_{SD}=5$ V for illumination duration of 10 s

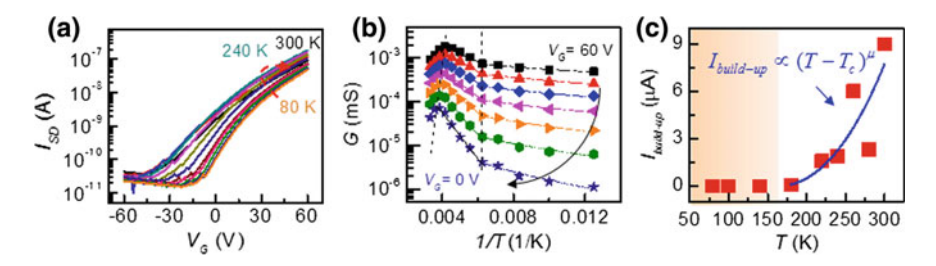


Fig. 6.10 Transport characteristics and PPC for sample A: **a** The two-probe transfer curves at different temperatures. **b** Arrhenius plots of the conductance at different V_G values. **c** The temperature dependence of the PPC buildup level $(I_{build-up})$, where the solid line is the fitted result using the transition temperature $T_c = 160 \,\text{K}$, which is obtained from the transport measurement

6.4.9 Carrier Mobility Dependence of the PPC

Figure 6.11 shows a distribution of τ versus mobility for 7 monolayer MoS₂ samples that were obtained by same illumination condition. The data suggest that the PPC

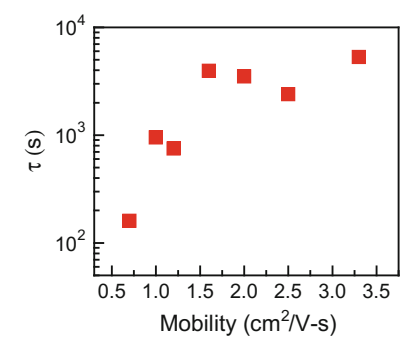


Fig. 6.11 The distribution of τ versus mobility for 7 monolayer MoS₂ samples that were obtained by the same illumination condition

becomes more persistent for higher mobility samples. It is conceivable that more persistent PPC is caused by higher density of the trap states in the MoS_2 channel. This could result in shorter average distance between the localized states and greater hopping rate among these states, leading to higher mobility. However, the detail mechanism behind the relation between τ and mobility requires further study.

6.5 Conclusion

Among the various types of photoresponses of MoS_2 , PPC at different levels has been reported. However, a detailed study of the PPC effect and its mechanism in MoS_2 is still not available, despite the importance of this effect on the photoresponse of the material. Here, we present a systematic study of the PPC effect in monolayer MoS_2 and conclude that the effect can be attributed to random localized potential fluctuations in the devices. Notably, the potential fluctuations originate from extrinsic sources based on the substrate effect of the PPC. Moreover, we point out a correlation between the PPC effect in MoS_2 and the percolation transport behavior of MoS_2 . We demonstrate a unique and efficient means of controlling the PPC effect in monolayer MoS_2 , which may offer novel functionalities for MoS_2 -based optoelectronic applications in the future.

References

- K.S. Novoselov, A.K. Geim, S.V. Morozov, D. Jiang, Y. Zhang, S.V. Dubonos, I.V. Grigorieva, A.A. Firsov, Science 306, 666 (2004)
- K.S. Novoselov, A.K. Geim, S.V. Morozov, D. Jiang, M.I. Katsnelson, I.V. Grigorieva, S.V. Dubonos, A.A. Firsov, Nature 438, 197 (2005)
- 3. Y. Zhang, Y.-W. Tan, H.L. Stormer, P. Kim, Nature 438, 201 (2005)

- K.S. Novoselov, V.I. Falko, L. Colombo, P.R. Gellert, M.G. Schwab, K. Kim, Nature 490, 192 (2012)
- 5. S.Z. Butler et al., ACS Nano. 7, 2898 (2013)
- 6. X. Huang, X.Y. Qi, F. Boey, H. Zhang, Chem. Soc. Rev. 41, 666 (2012)
- K.S. Novoselov, D. Jiang, F. Schedin, T.J. Booth, V.V. Khotkevich, S.V. Morozov, A.K. Geim, Proc. Natl. Acad. Sci. USA. 102, 10451 (2005)
- J.N. Coleman, M. Lotya, A. O'Neill, S.D. Bergin, P.J. King, U. Khan, K. Young, A. Gaucher, S. De, R.J. Smith, I.V. Shvets, S.K. Arora, G. Stanton, H.-Y. Kim, K. Lee, G.T. Kim, G.S. Duesberg, T. Hallam, J.J. Boland, J.J. Wang, J.F. Donegan, J.C. Grunlan, G. Moriarty, A. Shmeliov, R.J. Nicholls, J.M. Perkins, E.M. Grieveson, K. Theuwissen, D.W. McComb, P.D. Nellist, V. Nicolosi, Science 331, 568 (2011)
- B. Radisavljevic, A. Radenovic, J. Brivio, V. Giacometti, A. Kis, Nat. Nanotechnol. 6, 147 (2011)
- 10. V. Podzorov, M.E. Gershenson, C. Kloc, R. Zeis, E. Bucher, Appl. Phys. Lett. 84, 3301 (2004)
- 11. A.K. Geim, I.V. Grigorieva, Nature **499**, 419 (2013)
- Q.H. Wang, K. Kalantar-Zadeh, A. Kis, J.N. Coleman, M.S. Strano, Nat. Nanotechnol. 7, 699 (2012)
- 13. K.F. Mak, C. Lee, J. Hone, J. Shan, T.F. Heinz, Phys. Rev. Lett. **105**, 136805 (2010)
- A. Splendiani, L. Sun, Y.B. Zhang, T.S. Li, J. Kim, C.Y. Chim, G. Galli, F. Wang, Nano. Lett. 10, 1271 (2010)
- 15. B.W.H. Baugher, H.O.H. Churchill, Y.F. Yang, P. Jarillo-Herrero, Nano. Lett. 13, 4212 (2013)
- 16. B. Radisavljevic, A. Kis, Nat. Mater. 12, 815 (2013)
- A. Castellanos-Gomez, M. Poot, G.A. Steele, H.S.J. van der Zant, N. Agraït, G. Rubio-Bollinger, Adv. Mater. 24, 772 (2012)
- 18. K.F. Mak, K. He, J. Shan, T.F. Heinz, Nat. Nanotechnol. 7, 494 (2012)
- 19. D. Xiao, G.B. Liu, W.X. Feng, X.D. Xu, W. Yao, Phys. Rev. Lett. 108, 196802 (2012)
- 20. H. Zeng, J. Dai, W. Yao, D. Xiao, X. Cui, Nat. Nanotechnol. 7, 490 (2012)
- 21. Q. He, Z. Zeng, Z. Yin, H. Li, S. Wu, X. Huang, H. Zhang, Small 8, 2994 (2012)
- 22. H. Li, Z. Yin, Q. He, H. Li, X. Huang, L. Gang, D. Wen Hui Fam, A. Ling Yoong Tok, Q. Zhang, H. Zhang, Small 8, 63 (2012)
- 23. C.F. Zhu, Z.Y. Zeng, H. Li, F. Li, C.H. Fan, H. Zhang, J. Am. Chem. Soc. 135, 5998 (2013)
- 24. B. Radisavljevic, M.B. Whitwick, A. Kis, ACS Nano. 5, 9934 (2011)
- H. Wang, Yu. Lili, Lee Yi-Hsien, S. Yumeng, H. Allen, L. Matthew Chin, L. Lain-Jong, D. Madan, K. Jing, P. Tomas, Nano Lett. 12, 4674 (2012)
- Z.Y. Yin, L. Hai, L. Hong, L. Jiang, S. Yumeng, S. Yinghui, L. Gang, Z. Qing, C. Xiaodong, Z. Hua, ACS Nano. 6, 74 (2012)
- H.S. Lee, S.W. Min, Y.G. Chang, M.K. Park, T. Nam, H. Kim, J.H. Kim, S. Ryu, S. Im, Nano Lett. 12, 3695 (2012)
- M. Buscema, M. Barkelid, V. Zwiller, H.S.J. van der Zant, G.A. Steele, A. Castellanos-Gomez, Nano. Lett. 13, 358 (2013)
- M. Fontana, T. Deppe, A.K. Boyd, M. Rinzan, A.Y. Liu, M. Paranjape, P. Barbara, Sci. Rep. 3 (2013)
- 30. K. Roy, M. Padmanabhan, S. Goswami, T.P. Sai, G. Ramalingam, S. Raghavan, A. Ghosh, Nat. Nanotechnol. **8**, 826 (2013)
- O. Lopez-Sanchez, D. Lembke, M. Kayci, A. Radenovic, A. Kis, Nat Nanotechnol 8, 497 (2013)
- W. Zhang, J.-K. Huang, C.-H. Chen, Y.-H. Chang, Y.-J. Cheng, L.-J. Li, Adv. Mater. 25, 3456 (2013)
- O. Lopez-Sanchez, D. Lembke, M. Kayci, A. Radenovic, A. Kis, Nat Nanotechnol. 8, 497 (2013)
- G. Cunningham, U. Khan, C. Backes, D. Hanlon, D. McCloskey, J.F. Donegan, J.N. Coleman, J. Mater. Chem. C. 1, 6899 (2013)
- 35. K. Cho, T.Y. Kim, W. Park, J. Park, D. Kim, J. Jang, H. Jeong, S. Hong, T. Lee, Nanotechnol. **25**, 155201 (2014)

References 71

- 36. S. Ghatak, A.N. Pal, A. Ghosh, ACS Nano. 5, 7707 (2011)
- H. Qiu, T. Xu, Z. Wang, W. Ren, H. Nan, Z. Ni, Q. Chen, S. Yuan, F. Miao, F. Song, G. Long,
 Y. Shi, L. Sun, J. Wang, X. Wang, Nat. Commun. 4, 2642 (2013)
- 38. W. Zhu, T. Low, Y.-H. Lee, H. Wang, D.B. Farmer, J. Kong, F. Xia, P. Avouris, Nat. Commun. 5, 4458 (2014)
- 39. S. Ghatak, A. Ghosh, Appl. Phys. Lett. 103, 122103 (2013)
- 40. S.L. Li, K. Wakabayashi, Y. Xu, S. Nakaharai, K. Komatsu, W.W. Li, Y.F. Lin, A. Aparecido-Ferreira, K. Tsukagoshi, Nano Lett. 13, 3546 (2013)
- 41. C. Lee, H. Yan, L.E. Brus, T.F. Heinz, J. Hone, S. Ryu, ACS Nano. 4, 2695 (2010)
- 42. H.-C. Cheng, R.-J. Shiue, C.-C. Tsai, W.-H. Wang, Y.-T. Chen, ACS Nano. 5, 2051 (2011)
- F.Y. Shih, S.Y. Chen, C.H. Liu, P.H. Ho, T.S. Wu, C.W. Chen, Y.F. Chen, W.H. Wang, AIP Adv. 4, 067129 (2014)
- 44. C. Kyungjune, K. Tae-Young, P. Woanseo, P. Juhun, K. Dongku, J. Jingon, J. Hyunhak, H. Seunghun, L. Takhee, Nanotechnol. 25, 155201 (2014)
- 45. T. Korn, S. Heydrich, M. Hirmer, J. Schmutzler, C. Schuller, Appl. Phys. Lett. **99**, 102109 (2011)
- 46. D. Kozawa, R. Kumar, A. C., K.K. Amara, W. Zhao, S. Wang, M. Toh, R.M. Ribeiro, A.H. Castro Neto, K. Matsuda, G. Eda, Nat. Commun. 5, 4543 (2014)
- 47. H.X. Jiang, J.Y. Lin, Phys. Rev. Lett. 64, 2547 (1990)
- 48. H.X. Jiang, J.Y. Lin, Phys. Rev. B 40, 10025 (1989)
- 49. R.G. Palmer, D.L. Stein, E. Abrahams, P.W. Anderson, Phys. Rev. Lett. 53, 958 (1984)
- 50. A.S. Dissanayake, S.X. Huang, H.X. Jiang, J.Y. Lin, Phys. Rev. B 44, 13343 (1991)
- 51. H.X. Jiang, J.Y. Lin, Phys. Rev. Lett. 64, 2547 (1990)
- 52. D.C. Johnston, Phys. Rev. B 74, 184430 (2006)
- 53. C.P. Lu, G.H. Li, J.H. Mao, L.M. Wang, E.Y. Andrei, Nano Lett. 14, 4628 (2014)
- 54. S. McDonnell, R. Addou, C. Buie, R.M. Wallace, C.L. Hinkle, ACS Nano. 8, 2880 (2014)
- 55. S. Ghatak, S. Mukherjee, M. Jain, D. Sarma, A. Ghosh, arXiv preprint arXiv:1403.3333 (2014)
- N. Scheuschner, O. Ochedowski, A.M. Kaulitz, R. Gillen, M. Schleberger, J. Maultzsch, Phys. Rev. B 89, 125406 (2014)
- 57. S.-Y. Chen, P.-H. Ho, R.-J. Shiue, C.-W. Chen, W.-H. Wang, Nano Lett. 12, 964 (2012)
- C.-C. Wu, D. Jariwala, V.K. Sangwan, T.J. Marks, M.C. Hersam, L.J. Lauhon, J. Phys. Chem. Lett. 4, 2508 (2013)
- 59. D.V. Lang, R.A. Logan, Phys. Rev. Lett. **39**, 635 (1977)
- 60. D.V. Lang, R.A. Logan, M. Jaros, Phys. Rev. B **19**, 1015 (1979)
- 61. H.J. Queisser, D.E. Theodorou, Phys. Rev. B 33, 4027 (1986)
- 62. T.N. Theis, S.L. Wright, Appl. Phys. Lett. 48, 1374 (1986)
- 63. R.J. Nelson, Appl. Phys. Lett. 31, 351 (1977)
- Y.C. Lee, J.L. Shen, K.W. Chen, W.Z. Lee, S.Y. Hu, K.K. Tiong, Y.S. Huang, J. Appl. Phys. 99, 063706 (2006)
- G. Konstantatos, M. Badioli, L. Gaudreau, J. Osmond, M. Bernechea, F.P.G. de Arquer, F. Gatti, F.H.L. Koppens, Nat. Nanotechnol. 7, 363 (2012)
- S.-Y. Chen, Y.-Y. Lu, F.-Y. Shih, P.-H. Ho, Y.-F. Chen, C.-W. Chen, Y.-T. Chen, W.-H. Wang, Carbon 63, 23 (2013)
- S.T. Lo, O. Klochan, C.H. Liu, W.H. Wang, A.R. Hamilton, C.T. Liang, Nanotechnol. 25, 375201 (2014)
- 68. M.M. Furchi, D.K. Polyushkin, A. Pospischil, T. Mueller, Nano Lett. 14, 6165 (2014)

Chapter 7 Conclusion



In this dissertation, investigations of a variety of physical phenomena in graphene junctions were reported. These measurements revealed interesting features such as SdH oscillation, weak localization, scaling behavior, the fractional-valued QH plateau, and plateau-plateau transition points between the quantum Hall plateau. In MoS₂ devices, the PPC effect was found after illumination is terminated. The mechanism of PPC effect can be well explained by the RLPF model.

In Chap. 4, I presented the distinctive magneto transport properties of graphene p-n-p and p-n junction devices enabled by the resist-free and one-step method. We demonstrate precise control of lateral diffusion and interfacial oxidation of the metallic contact, which leads to the fabrication of high-quality graphene hetero structures. The fabricated graphene p-n-p and p-n junction samples exhibit pronounced QH effect with fractional-valued plateaus due to the full mixing of the edge states. The positive MC of the graphene p-n-p junction devices at low magnetic field is well described by the WL theory and the extracted coherence length is found to be correlated to the conductance in the back-gate dependence measurement. The demonstrated method can offer novel scheme for the fabrication of high-quality devices composed of general 2D materials.

In Chap. 5, I demonstrated a unique method of fabricating a graphene p-n-p junction by controlling the lateral diffusion of the metallic contacts. The measured $G - V_G$ curves can be thoroughly described by the metal contact model, confirming the charge density depinning and the presence of interfacial oxidation. The graphene p-n-p junction devices showed quantization condition in the unipolar regime is described by pronounced half integer in QHE due to the contribution of the nontrivial Berry's phase. In the bipolar regime, a well-defined transition point of the zeroth LL, and the scaling behavior has been observed, indicating the non-localized states in the zeroth LL. In addition, we can estimate E_N for the LL index which is consistent with the theoretically values. The demonstration of a high-quality graphene p-n-p junction with controlled diffusion of the contacts provides an alternative fabrication method for future graphene-based electronics. A clear indication

74 7 Conclusion

of a phase shift of π in the magnetoconductance clearly indicates again the existence of a non-trivial Berry's phase.

In Chap. 6, we have demonstrated that PPC in monolayer MoS_2 can be controlled by temperature, the photon dose, the excitation energy, and the substrate effect. These characteristics show that PPC in MoS_2 can be well-explained by the RLPF model. The potential fluctuations could be attributed to extrinsic sources because of the absence of PPC in the suspended MoS_2 devices. Moreover, the temperature dependence of the PPC could be described as a transition from localization to percolation models, which was in agreement with the transport properties of MoS_2 . The results of this study can provide insight into PPC phenomena in monolayer MoS_2 , which is important for the development of MoS_2 -based optoelectronic applications.